

CHAPTER 7: THIN LIQUID WALL CONCEPTS AND THE CLIFF DESIGN

Contributors

Lead Author: Neil B. Morley
Sergey Smolentsev
Karani Gulec
Alice Ying
Mahmoud Youssef
Brad Nelson
Paul Fogarty
Dai-Kai Sze
Hesham Khater
Kathy McCarthy
Mohamed Abdou
Mike Kotschenruether
Mohamed Sawan

7. THIN LIQUID WALL CONCEPTS AND THE CLIFF DESIGN

Jump off the CLiFF and build your wings on the way down – Ray Bradbury

7.1 Introduction

The idea behind CLiFF, the *Convective Liquid Flow First-Wall* concept, is to eliminate the presence of a solid FW facing the plasma through which the surface heat load must conduct. This goal is accomplished by means of a fast moving (*convective*), thin liquid layer flowing on the FW surface (see Figure 7.1-1). The layer adheres to the curved wall by means of its centrifugal acceleration, U^2/R , where U is the velocity and R is the radius of curvature of the first structural wall surface. This thin layer is easier to control than a thick liquid FW/Blanket, but still provides a renewable liquid surface immune to radiation damage and sputtering concerns, and largely eliminates thermal stresses and its associated problems in the first structural wall. The liquid film can be utilized at the bottom of the reactor as an integrated liquid surface divertor, and then removed from the vacuum chamber by gravity drainage, an EM pump (if the working liquid is an electrical conductor), or some more sophisticated head recovery system. The CLiFF class of liquid wall concepts is viewed as a more near-term application of liquid walls.

The working liquid should be a tritium breeding material like lithium, lead-lithium, tin-lithium or FLiBe. Thus the liquid removed from the reactor can be recirculated to the blanket as the main tritium breeder and coolant. The bulk nuclear heat is added on top of the FW/divertor heat before the liquid is sent to the power conversion system. In this manner, the FW and divertor power is not wasted, but converted at relatively high thermal efficiency. The surface layer also improves the overall tritium breeding of the system.

The convective liquid layer concept has many issues that must be addressed before the idea can be seriously considered for use in a tokamak or other magnetic confinement device. The main issue is the compatibility of a free surface liquid with the plasma. Plasma compatibility will likely set a limit on the amount of material allowed to evaporate or sputter from the surface, possibly as a function of poloidal location around the reactor. This evaporation limit will in turn give a surface temperature limit of the flowing liquid layer. Other potential issues include the effect of a hydrogen or impurity *getter* (like lithium) on the fuel balance in the reactor system, liquid removal or drainage from a zero pressure chamber, corrosion, and nuclear damage of support structures and electrical insulators. At high wall load especially, this last concern is very serious as the flowing liquid layer does little to reduce the DPA or helium production in the *submerged* supporting structure.

Details of the preliminary design, heat transfer, power balance, thermal-hydraulic performance, neutronics, activation and safety are included in this chapter. It is noted that the first several centimeters of a thick liquid FW/blanket concept will behave (thermal-hydraulically) in a very similar fashion to the various thick liquid wall concept discussed

in the preceding chapters, and significant overlap with those analyses will be seen in what follows. However, significant differences do exist and will be pointed out when appropriate. An attempt to keep consistent notation and working assumptions has been made during the preparation of this document. However, the CLiFF analysis and design is still a *work-in-progress* and so this goal of absolute consistency has not always proved possible, and some sections authored by different people, will have small contradictions and differences in nomenclature.

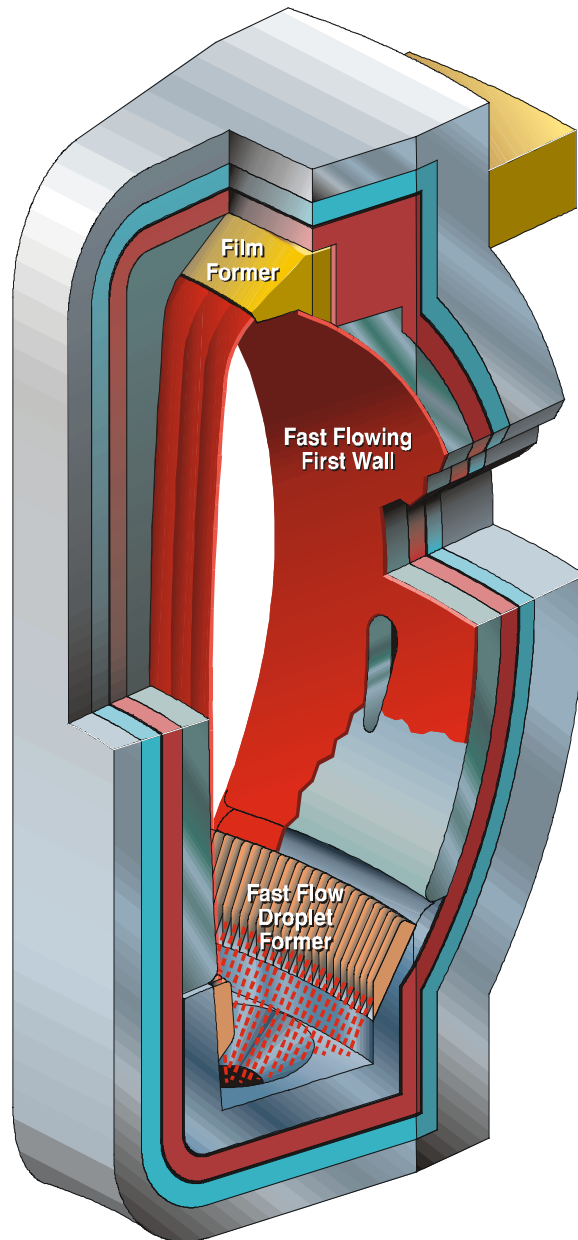


Figure 7.1-1: Conceptual sector schematic of CLiFF implementation in ARIES-RS scale reactor.

7.2 Idea Description and Rationale

7.2.1 General Perspective and Preliminary Design Description

The general CLiFF design, as seen in Figure 7.1-1, is conceptually simple in its implementation. A thin fast liquid layer is injected near the top of the plasma chamber. The layer flows down the reactor walls without excessive slowing down or thinning out, is removed in some fashion from the bottom of the chamber. Layer thicknesses h on the order of 0.5 to 2 cm, and velocities U on the order 10 m/s, are considered for three different working liquids; Li, Sn-Li, and the molten salt FLiBe. The curved reactor wall fits the plasma shape and provides an adhesion force due to the liquid's centrifugal acceleration. The criteria for continuous attachment of the liquid layer is simply:

$$U^2/R > g \cos\alpha, \quad (7.2-1)$$

where g is the acceleration of gravity and α refers to the angle from vertical.

The velocity range is chosen quite high both to ensure adhesion to the back-wall, but also to keep the exposure time to the plasma short, and thus keep the surface temperature low. It turns out that it is this second restriction that is the more severe, based on the maximum surface temperature estimates provided by the preliminary plasma edge analysis described elsewhere.

The CLiFF design shown in Fig. 7.1-1 has an integrated droplet-type divertor. Some means (mechanical or electrical) are used to stimulate the breakup of the FW flow into a droplet screen. It is hoped that the droplet screen will have a higher heat removal capability due to the rapid rotation and internal circulation in the droplets, but this fact remains to be proven. In addition, for LMs, the droplet screen will be electrically isolated from the main FW flow and plasma currents will not be able to close.

Supply nozzles will form the desired liquid flow at the top of the reactor. These nozzles will likely present a limited amount of solid surface to the plasma, but since they are at the top of the reactor chamber, the surface heat load and nuclear heat will be lower than the peak mid-plane values. Removal from the plasma chamber is accomplished by gravity drain through a combined vacuum pumping and liquid drain port. It is envisioned that the liquid flow itself will pump a portion of the implanted plasma particles into the pumping ducts by convection, thus aiding in impurity removal.

Penetrations for various heating, fueling and diagnostics functions will be provided as much as possible in the lower half of the outboard FW. Flow can be guided by means of submerged grooves around the penetration, and close again downstream to form a continuous surface protection. Cooling of the penetration structures themselves will be aided by the CLiFF flow. It is likely that for LMs, the penetrations will have to be electrically isolated from the flow by means of some insulator coating. This will be true in supply lines and nozzles as well, to avoid large MHD drag forces that will prevent the rapid flow of the liquid metal.

Off-normal plasma events like disruption can possibly induce large currents LM CLiFF flows and cause the layer to be splashed or torn-off the wall altogether. For Flibe, the effect of the disruption is not as clear. It is hoped that, in any case, splashing will turn out to be an allowable response, and that the liquid wall will just be restarted following the disruption. For an all-liquid wall system, this seems a reasonable assumption, except for possible damage to antennae and sensitive diagnostics. It is hoped that “liquid tolerant” antennae could be designed that could accept the occasional splashing of liquid metal, but this certainly remains to be seen

The presence of this thin, rapidly moving liquid layer has the potential to dramatically change the attractiveness outlook as compared to solid FW structures due to elimination of the thermal stress due to FW surface heating and potentially beneficial effects on the stability of the plasma. Of course, the idea of using a liquid surface exposed to the plasma suggests a myriad of potential problems as well. Table 7.2-1 summarizes the potential advantages and issues identified in the APEX project.

7.2.2 Applications to Tokamaks

The majority of the work reported here was carried out for a tokamak implementation. Specifically, the ARIES-RS geometry was utilized whenever possible, with modifications for the unique structures and high flowrates required for CLiFF. This means, however, that the ARIES-RS fusion power needed to be scaled-up to 4500 MW to give the 10 MW/m² peak neutron wall load and 2 MW/m² peak surface heat flux mandated in the APEX project.

Tokamaks present a difficult challenge for liquid walls due to the fact that the plasma chamber is relatively closed with a thin scrape-off layer, and so vaporized liquid wall material must be efficiently screened by the edge plasma to keep it from penetrating to the core. A certain amount of impurity is tolerable, maybe even desirable, but the interaction with the plasma becomes a crucial feasibility issue for liquid walls in tokamaks. Additionally, tokamak geometries are complex and complete coverage is a difficult challenge. Although spherical tokamaks have not yet been looked at in detail for CLiFF, it is assumed that they will have the same problems with plasma contamination that faces conventional tokamak embodiments like the ARIES-RS.

7.2.3 Applications to Other MFE Confinement Schemes

It is hypothesized that other high power density confinement schemes, most notably the FRC, would be more amenable to liquid walls in general, including CLiFF concepts. As yet, however, no work has been done to conceptualize a CLiFF implementation in the FRC designs like those shown in Chapter 5 for thick liquid walls. However, it is assured that a thicker scrape-off layer and the removal of the divertor region to greater distance from the core plasma will increase the allowable vaporization limits and make the CLiFF

Table 7.2-1: Potential Advantages and Issues of CLiFF Concept for APEX

Potential:	Issue:
<ul style="list-style-type: none"> • Removal of surface heat loads (greater than 2 MW/m² possible). Local peaking and transients can be tolerated • FW surface protected from sputtering erosion and possibly disruption damage • Beneficial effects on confinement and stability from conducting shell and DT gettering effects • Elimination of high thermal stresses in solid FW components, having a positive impact on failure rates • Possible reduction of structure-to-breeder ratio in FW area, with breeder material facing virgin neutron flux • Integrated divertor surface possible where CLiFF flow removes all α heat • Complex tokamak D-shape & ports can likely be accommodated 	<ul style="list-style-type: none"> • Hydrodynamics and heat transfer involve complicated MHD interaction between flow, geometry, and the magnetic field: <ul style="list-style-type: none"> – Suppression of turbulence & waves – LM-MHD drag thickens flow and inhibits drainage from chamber – Effects of varying fields on LM surface stability and drag • Evaporating liquid can pollute plasma, surface temperature limits unknown • High flowrate requirement can result in low coolant ΔT or two coolant streams • Effect of liquid choice on edge plasma gettering, tritium through-put, and tritium breeding • Neutron damage in structure is only slightly reduced compared to standard blankets, blanket change-out required for high power density operation

7.3 Hydrodynamics Analysis

Aside from plasma compatibility, one of the key class of feasibility issues for CLiFF is the hydrodynamic configuration. A significant amount of design analysis has been done so far on CLiFF in order to answer the three basic questions: how do you form it? How do you drain it? How do you maintain it? As an introduction to this analysis, it should be noted that liquid metals and Flibe behave very differently in the magnetic environment of a tokamak. The low thermal and electrical conductivity of Flibe indicates that the Flibe flow will still be turbulent, and that the heat transport at the free surface and flow drag at the back-wall will depend heavily on this turbulence. For LMs the converse case occurs, where it is expected that the MHD effects will dominate the drag, and the heat transfer largely by thermal conduction. Typical dimensionless parameters that indicate these trends are summarized in Table 7.3-1.

7.3.1 Fast Liquid Layer Hydrodynamics for Turbulent Flibe Flow

One of the first difficulties involving the use of free surface films for fusion reactors is determining how do you make the flow conform as closely as possible to the plasma shape, but keep it adhered to the wall. The CLiFF concept, as stated above, relies on centrifugal acceleration to keep the flow attached to a concave surface. To this end, the flow has to carry adequate centrifugal inertia to balance against the gravity, friction and MHD forces. Several models have been applied to predicting the flow profiles, ranging from simple hydraulic models for the steady state equilibrium flow profile, to more complex two- and three-dimensional non-steady codes for studying phenomena like surface waves and penetrations. These different analyzes are described below.

7.3.1.1 1½-D Hydraulics Analysis for Flibe Flow on Cylindrical Back-Wall

The hydraulics of a thin flow on a typical plasma topological surface is analyzed using the simplified conservation equations for mass and momentum in cylindrical coordinates (see Figure 7.3-1).

$$\begin{aligned}
 -\frac{U^2}{R} &= -\frac{1}{\rho} \frac{\partial p}{\partial r} - g \cos \alpha \quad (\text{r - momentum}) \\
 \frac{1}{2R} \frac{\partial U^2}{\partial \alpha} &= -\frac{1}{\rho R} \frac{\partial p}{\partial \alpha} - \frac{fU^2}{8h} + g \sin \alpha \quad (\alpha - \text{momentum}) \\
 U &= \frac{Q}{hw} \quad (\text{conservation of mass})
 \end{aligned} \tag{7.3-1}$$

Here U, h, and p represent the mean flow velocity, layer height (depth) and pressure in the layer; r and α are the cylindrical coordinates, and Q, w(α), R, are the known volumetric flowrate, flow width, and back-wall radius of curvature. The symbols f and ρ are the Darcy-Weisbach friction factor and the liquid density.

These simple equations can then be solved to produce profiles of U, h and p as a function of location on the arc. The pressure p is an indicator of the adherence of the film, and is always positive for attached flows.

$$\begin{aligned}
 \frac{dh}{d\alpha} &= \frac{-gRh^3 \left(1 - \frac{h}{R}\right) \sin \alpha + \frac{fRQ^2}{8w^2} - \frac{hQ^2}{w^3} \left(1 + 2\frac{h}{R}\right) \frac{dw}{d\alpha}}{gh^3 \cos \alpha + \frac{Q^2}{w^2} \left(1 + \frac{h}{R}\right)} \\
 U &= Q/wh \\
 p &= \rho h \left(\frac{U^2}{R} - g \cos \alpha \right)
 \end{aligned} \tag{7.3-2}$$

The appropriate friction term is determined by the type of flow. For an low electrical conductor like Flibe, the flow is turbulent and the friction is estimated from the Darcy-Weisbach formula applied to open channels using the appropriate friction factor, f

$$\Delta head_f = \frac{fL}{4R_H} \frac{U^2}{2g} \Rightarrow \frac{\partial p_{loss}}{\partial \alpha} = \frac{fR}{4h} \frac{\rho U^2}{2} \quad (7.3-3)$$

Contributions to the friction by MHD forces is estimated to be small in a thin Flibe flow that is highly elongated along the toroidal field. However, the complete neglect of MHD forces in free surface Flibe flows is not assured as the layer height is increased, or the layer width or velocity is decreased. This fact should be kept in mind as the design for CLiFF (and various thick liquid concepts) evolves.

The equilibrium height can be determined by setting the numerator of the evolution equation for h equal to zero. This is the point where friction balances gravitational acceleration.

$$h_{eq} = \left(\frac{fQ^2}{8gw^2 \sin \alpha} \right)^{1/3} \quad (7.3-4)$$

(We have assumed for simplicity sake that $h \ll R$ for CLiFF). The film height is thus very sensitive to the definition of the friction term, and this term is checked in subsequent calculations described later in the chapter.

The correct choice for the friction factor depends on the flow conditions. The Reynolds number (based on the hydraulic diameter) is in the 10^5 range. For a smooth wall, the friction factor from the Moody Diagram suitable for pipe flow is $f = 0.018$. If the surface is rougher, or if additional boundary layer turbulence phenomena results from things Taylor-Gortler instabilities, then the friction factor is likely to increase by 25 to 30%. We use here a value

$$f = 0.025 \quad (7.3-5)$$

as our best estimate.

The toroidal width is assumed to vary with the size of an ARIES-RS toroidal sector as a function of poloidal angle on the outboard. Calculations for the inboard assume the width is constant.

$$\begin{aligned} w(\alpha) &= w_o \cdot (R_o + R_c \cdot \sin[\alpha]) / (R_o + R_c \cdot \sin[\alpha_o]) && \text{outboard} \\ w(\alpha) &= w_o && \text{inboard} \end{aligned} \quad (7.3-6)$$

Here w_o is the width where the inboard meets the outboard, and α_o , R_o is the initial angle, and associated major radius, of the outboard sector (see Figure 7.3-1). The formulations

allows no energy loss in flow re-distribution as it expands and contracts in the toroidal direction, it simply enforces conservation of mass. The radius of curvature for the outboard that best fits the plasma shape is $R_c = 3.8$ m. The sector width is plotted in Figure 7.3-2.

Hydraulic calculations indicate that a flow depth equilibrium in the range of 2 cm can be achieved for Flibe flows in the 8-10 m/s range (see Figures 7.3-3). Bear in mind that a thicker/faster film leads to a high volumetric flow and more difficulties in supply and removal of the CLiFF stream from the plasma chamber. Designs should try to optimize simultaneously to maximize heat transfer (low surface temperatures) and minimize mass flow-rate (too keep pumping power down and maximize bulk temperature rise). The back-wall pressure for the cases in Figure 7.3-3 is given in Figure 7.3-4 where it is seen that no cases result in detachment from the back-wall. These calculations serve as a basis for the Flibe design that is discussed throughout the remainder of the chapter.

7.3.1.2 Numerical Calculations of Turbulent Flow Based on the "k- ϵ " Model

The low-Reynolds number k- ϵ model of turbulence [1] was applied to the thin layer flow of low conducting liquids in order to study the effect of turbulence on the flow profile (and in a later Section 7.5 on the surface temperature and heat transfer). In comparison to the ordinary k- ϵ model, the present one was extended to the MHD case by means of additional terms in the closure equations [2]. These terms stand for the Joule dissipation by the induced currents. Two variants of boundary conditions on the free surface were used, the Naot boundary condition [3], and the zero surface turbulence boundary condition. The first one expresses the turbulence redistribution by the free surface, and does not force turbulent fluctuations to zero. The second one simulates the effect of the near-surface layer, where the normal component of the turbulent motion is absent. The calculations have been carried for CLiFF parameters with Flibe as a working fluid. The details of the calculational methodology are discussed in Chapter 5 and are not repeated here.

As calculations show, the two variants of the boundary conditions give approximately the same results for the hydrodynamic quantities, the layer thickness and the velocity profiles. This is because the processes near the back-wall, not at the surface-layer, determine the changes in the flow thickness and in the velocity field. Nevertheless, the boundary conditions lead to different results in the surface temperature as will be discussed later.

Some preliminary benchmarks were made to validate the code. First of all, it was tested against the analytical solution for the fully developed flow between parallel plates. Both the velocity profile and the Nusselt number are in good agreement with the analytical results. To validate the code in the turbulent regime for the free surface flows, the calculated mixing length was compared with that from numerical calculations carried out by Naot *et al.* on the basis of similar k- ϵ model [4] where it is seen that these two predictions are almost identical. This fact demonstrates that the code is formulated

correctly. Nevertheless, this comparison is not enough to draw a conclusion about the k- ϵ model applicability to the free surface flows along concave walls especially in the presence of a magnetic field.

The computations were carried out with CLiFF parameters for Flibe. Due to turbulent viscous friction, the layer thickness increases rapidly over the initial flow section (Figure 7.3-5). This is in contrast to the results presented earlier where the simple friction factor formulation predicts nearly constant flow height and velocity profiles for CLiFF. This is cause for concern because if the layer slows down significantly, the transit time through the plasma chamber will go up, as well as the surface temperature (discussed in more detail later). Attempts to benchmark the k- ϵ and friction factor against available data from the UCLA Mega-Loop Experiment [5], shown in Figure 7.3-6, are inconclusive. The data splits the difference between the k- ϵ and friction factor. Unfortunately, we have not found any conclusive data to validate the model. At present, some benchmarks are being planned to test our results against numerical data from Direct Numerical Simulation (DNS).

The effect of the magnetic field on the flow parameters (see Figure 7.3-7) is negligible if the Hartmann number is less than about 1000, and hence we conclude that there is no strong impact of MHD on the Flibe flow for CLiFF. Only when the Hartmann number gets larger is an effect observed. Remember for CLiFF the Hartmann number is about 500.

7.3.1.3 Surface and Boundary Layer Stability with Flibe

Hydrodynamic characteristics of Cliff concept that uses Flibe as a working fluid are investigated in two main sections:

- Determination and evaluation of operational parameters that may effect the hydrodynamic stability of the thin (liquid layer thickness ≤ 2 -cm) liquid layer.
- Determination of possible hydrodynamic perturbation sources, such as geometric configuration, upstream flow generating mechanisms, etc.

The current study is as a preliminary hydrodynamic feasibility analysis for poorly electrically conducting operational fluids. As a first step, MHD effects on the hydrodynamic characteristics of the thin liquid layer flow are assumed to be negligible. In addition, current study does not include the designs of upstream components for delivering the high velocity liquid layers (nozzle contraction ratio, nozzle upper wall curvature, *etc.*). Therefore, in the second section, the impacts of external parameters on the hydrodynamic stability of the proposed liquid walls are explained and several modifications for future designs of upstream components are proposed to prevent or minimize the disturbances to the flow.

Linear Stability Analysis of High Velocity Liquid Flow over a Concave Surface

There are many studies performed for high velocity liquid layer flow over concave surfaces and in swirl chambers (which are totally filled with fluid for combustion studies) [6,7,8,9]. The experimental information obtained from swirl chamber studies suggest that the radial distribution of the tangential flow is divided into two regions - a region of forced rotational flow in the center of the chamber which is surrounded by a region of quasi-free rotational flow. The α -component of the quasi-free swirl flow has the similar hydrodynamic characteristics of proposed Cliff concept which uses high velocity thin liquid layer over a concave back wall structure to take advantage of centrifugal force to keep the thin liquid layer adhered to the back wall.

As seen in Table 7.3-3, thin liquid layer flow over concave back wall has a high Reynolds numbers ($Re > 10^4$) where the boundary layer thickness may be less than the liquid layer thickness for several meters away from the inlet section. As an example, ratio of the turbulent boundary layer thickness

$$\delta = 0.16x^{6/7} \left(\frac{\rho U}{\mu} \right)^{-1/7} \quad (7.3-7)$$

(where x is the axial distance along the cylindrical chamber, ρ is the density and μ is the viscosity of the fluid) to 0.02-m liquid layer thickness of Flibe at 550 C with 10 m/s inlet velocity at a location of 1.5-m away from the inlet is ~ 1 . This section of the liquid layer flow has main stream and boundary layer flow regions and is subject to external perturbation sources that may be coming from converging nozzle section. Linear stability analysis of a high velocity liquid layer flow over a concave surface is performed to determine the possible mechanisms that may effect the stability of the liquid layer from inlet section to 1 m away from the inlet. Potential flow theory can be used for the characterization of flow in alpha direction for linear stability analysis. 2-d (r - α) linear stability analysis is performed using an irrotational velocity profile with surface tension, gravitational acceleration and the centrifugal acceleration models. The assumptions are: (1) boundary layer thickness is small compared to the free stream thickness, (2) only velocity component in alpha direction is taken into account, (3) initial infinitely small perturbations are introduced for the surface displacement and velocity potential. Assuming a fully developed potential flow in cylindrical geometry, the velocity profile in the Flibe flow in the alpha flow direction may be expressed as:

$$U(r) = C \frac{R_s}{r} \quad (7.3-8)$$

where R_s corresponds the radius of curvature at the boundary layer surface, C is constant and r is the radial variable. Using the velocity profile stated above, the velocity potential can be expressed as $\phi = U_s R_s \alpha$, where U_s corresponds to the velocity component in alpha direction at the free-surface.

Laplacian of the velocity potential of a potential flow must be equal to zero as

$$\nabla^2 \phi = 0 \quad (7.3-9)$$

The pressure equilibrium at the surface streamline can be expressed using the Bernoulli Equation,

$$\frac{\partial \phi}{\partial t} + \frac{1}{2}(\nabla \phi)^2 + \frac{P}{\rho} + gz = C(t) \quad (7.3-10)$$

The mechanisms affecting the pressure at the free surface streamline may be centripetal acceleration, surface tension and gravitational acceleration, when there is a surface displacement. The first order modeling of these mechanisms for a very small surface displacement (ζ) is explained as follows.

Modeling of Centrifugal Acceleration Term: The pressure at the streamline of the potential flow in cylindrical coordinates with a free surface at the inner radius can be expressed as,

$$\frac{dp}{dr} = \rho \omega^2 r \quad (7.3-11)$$

where the angular velocity may be expressed as

$$\omega = \frac{U_s}{R_s} \quad (7.3-12)$$

where U_s corresponds the velocity component in the alpha direction at the flow free-surface. Using the above relationship in the radial pressure gradient and integrating over the small surface displacement of ζ ,

$$p' = \rho \frac{U_s^2}{R_s^2} \int_{R_s - \zeta}^{R_s} r dr \quad (7.3-13)$$

and neglecting the higher order surface displacement terms results in a simplified relationship for a pressure perturbation at the free surface

$$p' \approx \rho \frac{U_s^2}{R_s} \zeta \quad (7.3-14)$$

when there is a surface displacement.

Modeling of Surface Tension Term: The pressure perturbation at the free surface of a flow over a concave surface radius can be expressed as,

$$p = \sigma \left(\frac{1}{r} - \frac{1}{r^2} \frac{d^2 \zeta}{d\alpha^2} \right), \quad r = R_s \quad (7.3-15)$$

when flow over the concave surface has a free surface radius of curvature R_s and the small surface displacement of $\zeta(\alpha)$. The first term in the above relationship is due to the concavity of the flow and the second term is due to the surface displacement, which is a function of α . Although modeling the first term is straightforward and may come from the definition of surface tension, the modeling of the second term for Cartesian coordinates can be explained in Figure 7.3-9.

Modeling of Gravitational Acceleration Term: The direction of flow with respect to gravitational acceleration changes as the fluid flows in the α direction. The effect of varying gravitational acceleration on the free surface streamline pressure perturbation may be expressed as the following

$$p' \approx -\rho \zeta g \sin \alpha \quad (7.3-16)$$

for a 2D cylindrical geometry as shown in Figure 7.3-1.

Boundary Conditions: The thickness of the boundary layer is assumed to be an order of magnitude smaller than the thickness of the thin liquid layer flow. Therefore, the boundary layer thickness of the flow may be neglected, and the velocity in the radial direction at the boundary layer surface is assumed to be zero as,

$$V = \frac{\partial \phi}{\partial r} r_0 = 0, \quad r = R_w \quad (7.3-17)$$

At the free surface (the interface between the fluid and the vacuum), the fluid particles at the interface must move with the interface. Therefore, the vertical velocity at the interface may be expressed by the substantial derivative of the surface elevation [10] as:

$$\frac{\partial \phi}{\partial t} = \frac{D\zeta}{Dt} = \frac{\partial \zeta}{\partial t} + (\nabla \phi)_r \frac{\partial \zeta}{\partial r} + (\nabla \phi)_\alpha \frac{1}{r} \frac{\partial \phi}{\partial \alpha} \quad (7.3-18)$$

Linearization: Since the set of partial differential equations has constant coefficients independent of time and α , the method of normal modes is used in the linearization where small arbitrary perturbations of the form

$$\zeta, \phi' = (\hat{\zeta}, \hat{\phi}) e^{ik\alpha + st} \quad (7.3-19)$$

In the linearization process, the steady state and perturbed components of the velocity potential are used in both system and boundary equations. The steady state terms of the system and boundary equations are cancelled, and the terms containing higher order surface displacement or perturbed velocity potential are neglected since they have at least an order of magnitude smaller value than the terms containing first order surface displacement or perturbed velocity potential.

$$\nabla^2 (U_s R_s \alpha) + \nabla^2 \phi' = 0 \rightarrow \nabla^2 \phi' = 0 \quad (7.3-20)$$

Using the pressure perturbation terms in the Bernoulli Equation and linearizing results as,

$$\frac{\partial \phi'}{\partial t} + (\nabla \phi_0 \nabla \phi')_\alpha = \frac{1}{\rho} \left(\rho \zeta g \sin \alpha + \frac{\sigma}{R_s^2} \frac{\partial^2 \zeta}{\partial \alpha^2} - \rho \frac{U_s^2 \zeta}{R_s} \right) \quad (7.3-21)$$

The boundary conditions are linearized as,

$$r_0 \frac{\partial}{\partial r} (U_s R_s \alpha) + r_0 \frac{\partial}{\partial r} \phi' = 0 \rightarrow r_0 \frac{\partial}{\partial r} \phi' = 0 \quad r = R_w \quad (7.3-22)$$

$$\frac{\partial \phi'}{\partial r} = \frac{\partial \zeta}{\partial r} + \left(\frac{U_s R_s}{r} + \frac{1}{r} \frac{\partial \phi'}{\partial \alpha} \right) \frac{1}{r} \frac{\partial \zeta}{\partial \alpha} \quad r = R_s \quad (7.3-23)$$

Using the linearized form of system equations and boundary conditions, the coefficient of small disturbances in the exponent form is derived as,

$$s_{1,2} \cong \frac{U_s}{R_s} ik \pm i \sqrt{\frac{k}{R_2} \frac{1 - \left(\frac{R_w}{R_s}\right)^{2k}}{1 + \left(\frac{R_w}{R_s}\right)^k} \sqrt{g \sin \alpha - \frac{U_s^2}{R_s} - \frac{\sigma k^2}{R_s}}} \quad (7.3-24)$$

Using above equation, the liquid layer may be stable when gravitational acceleration, centrifugal acceleration and surface tension are taken into account and yield the following condition for stability:

$$g \sin \alpha < \frac{U_s^2}{R_s} + \frac{\sigma k^2}{R_s} \quad (7.3-25)$$

The above equation suggests that the high velocity liquid layer flow is always stable when the velocity component in the alpha direction is taken into account, since the centrifugal acceleration should be more than gravitational acceleration for the liquid layer to adhere to the wall. Gravitational acceleration has both stabilizing and destabilizing effects on the flow depending on the direction of the flow with respect to the direction of gravitational acceleration. Surface tension has a stabilizing effect for a high wave number (short wave wavelength) as expected. Hydrodynamic stability analysis will be extended to take into account the Coriolis force.

Mechanisms Affecting the Hydrodynamic Characteristics of Thin Liquid Flow Over Concave Surface

The primary section of the liquid first-wall flow system will include flow straighteners, contraction nozzles, curved back plates and drain systems. The fluid dynamic behavior of the first-wall flow system may be effected due to the existence of these components. Possible eddy generating mechanisms may be (Figure 7.3-9),

- Boundary layer relaxation on the flow surface at the nozzle exit
- Liquid first-wall operating conditions (Reynolds number, turbulence, flow surface topology), Froude number (hydraulic-jump), etc)
- Possible vortex generation/separation in the nozzle or flow straightener section

- Cylindrical flow geometry (centrifugal acceleration related Taylor-Gortler vortices)
- Inviscid shear-layer instabilities and stratification.

Eddy generating mechanisms may introduce/enhance the turbulence intensity in the liquid first-wall flow as well at its free surface. An increase in the turbulence intensity at the free surface may increase the convective heat transfer rate at the free surface. This condition may decrease the required minimum operation velocity so that minimum evaporation rate at the liquid first-wall surface can be maintained. Therefore, any of the eddy-generating mechanism should not be eliminated unless it destabilizes the liquid first-wall flow completely or increases mass loss in the first wall due to evaporation or spraying.

As seen in Table 7.3-3, the flow regimes in all the concepts proposed in the present study are turbulent. Both the Froude number and the modified Froude number are more than 1, therefore hydraulic jump may occur. This condition also predicts that the flow regimes in all the proposed concepts are supercritical, which means that the disturbances on the liquid first-wall surface may not propagate upstream.

Gortler Vortices Formation: The stability condition of a flow field of a boundary layer on a concave wall can be shown as:

$$\frac{r}{\delta_m} \leq \left(\frac{\rho \delta_m U_\infty}{\mu} \right)^2, \quad (7.3-26)$$

where r is the radius of curvature of the concave wall, δ_m is the momentum thickness and U_∞ is the liquid layer main stream velocity. It should be noted that the stability mechanism is inviscid and viscosity only damps the motion as in other inviscid instabilities. There may be randomly existing Gortler vortices in the turbulent boundary layer [11,12,13]. Destabilizing curvature amplifies large-scale motions that are normal to the wall. When the boundary layer entering the curve is free of spanwise non-uniformity, the resulting eddy structure does not consist of distinct longitudinal vortices. Flow is dominated by large eddies (inflows and outflows) that have streamwise extent of only a few boundary layer thickness, are quite unsteady, and do not cause significant variations in the mean properties of the boundary layer. Mixing across the boundary layer is enhanced by the new eddy structure that brings high momentum fluid closer to the wall than in the normal flat boundary layer and causes a significant increase in skin friction. Increase in the turbulence intensities and Reynolds shear stress across the outer layer are due to increased energy in low frequency, large scale motions.

Although large-scale inflows and outflows have strong influence on the flow structure in the near wall region, near wall profiles of Reynolds-averaged quantities may show relatively minor differences between the flat and concave back wall cases when the local value of the friction velocity u_τ is used for scaling.

The boundary layer is unstable for the operation velocity of 10 m/s over a 4.0 m radius of curvature when it is assumed that fluid layer flows over ~ 1.0 m flat plate (in the nozzle) before it reaches the concave back plate. The momentum thickness becomes as 3.9×10^{-4} m. And the inequality in becomes as:

$$\frac{4}{3.9 \times 10^{-4}} \leq \left(\frac{1963 \times 3.9 \times 10^{-4} \times 10}{6.78 \times 10^{-3}} \right)^2 \rightarrow 1.02 \times 10^4 \leq 1.27 \times 10^6, \quad (7.3-27)$$

which shows that there will be randomly existing Gortler vortices in the turbulent boundary layer. Using friction velocity as a scale may approximate the height, spanwise and streamwise dimensions of the vortices:

$$\frac{u_\tau}{U_\infty} = 0.576 \left(\frac{U_\infty \rho l}{\mu} \right)^{-\frac{1}{4}}. \quad (7.3-28)$$

In which, the boundary layer thickness for the turbulent flow may be estimated as:

$$\frac{\delta}{l} = 0.37 \left(\frac{U_\infty \rho l}{\mu} \right)^{-\frac{1}{5}}, \quad (7.3-29)$$

where δ is the boundary layer thickness, l is the distance in the flow direction, μ viscosity of the fluid, ρ is density and U_∞ is the free stream velocity.

The average height of the vortices for mildly curved back plate will be approximately $50\nu/u_\tau$ which corresponds 1.24×10^{-3} m and the average length of the vortices for mildly curved back plate will be approximately $1000 \cdot \nu/u_\tau$ which corresponds to ~ 0.025 m, for a 10 m/s liquid layer operation velocity over a 4 m radius of curvature.

Surface Waves Formation at the Nozzle Exit: Waves may form on the first wall surface due to the relaxation of the boundary layer leaving the nozzle exit from a no-slip boundary condition to a free-shear boundary condition. The relaxation of the boundary depends on the relaminarization of the flow in the convergent section of the nozzle (nozzle contraction ratio, upper wall surface curvature, etc). A critical Reynolds number based on momentum thickness on the nozzle wall for the onset of the surface waves is 70 by Brennen [14,15].

Boundary layer of the flow leaving the nozzle is related to the pressure distribution (nozzle contraction ratio, upper wall surface curvature) in the nozzle. Momentum thickness of the boundary layer leaving the upper wall of the nozzle is estimated using nozzle design data developed for Fusion Material Irradiation Test Facility FMIT for the liquid wall velocity of 10 m/s.

$$\text{BL momentum thickness} : 5.8 \times 10^{-5} \text{ m} \quad \text{Re momentum thickness} : 168 > 70 \quad (7.3-30)$$

As seen in above, surface waves are expected on the flow surface leaving the nozzle exit for a liquid layer velocity of 10 m/s from a FMIT nozzle type. The relationship between the surface waves on the free surface and the Reynolds number based on the momentum thickness is shown,

$$\alpha = \exp \left[-9.6481 + 2.4412 \ln(\text{Re}_m) - 0.1762 \ln^2(\text{Re}_m) \right] \quad (7.3-31)$$

where Re_m is Reynolds number based on momentum thickness, α is free surface wave number ($2\pi\delta_m/\lambda$) and λ is the free surface wavelength. The initial wavelength of the expected surface waves becomes as 0.21 cm. These surface waves are expected to be standing for surface tension parameters,

$$s = \sigma / (\rho \delta_m U_s^2) < 10^{-4} \quad (7.3-32)$$

where, σ is the surface tension, ρ is the liquid density and U_s is the surface speed. Surface waves are expected to be stable since the corresponding surface tension parameter is $1.7 \cdot 10^{-2}$. Then, the growth of waves may be result in two-dimensional and subsequently three-dimensional wave patterns.

The 3-D surface wave patterns may immediately exist after exiting the nozzle when the nozzle exit boundary layer is transitional or turbulent, which is also a function of flow velocity in addition to the nozzle contraction ratio and wall curvature. The source of the variations in the flow surface topology and the flow development length downstream of the nozzle mainly depends on nozzle design. Therefore, the design of liquid blanket/first-wall inlet section in a reactor design is crucial in delivering a uniform velocity profile to the cylindrical region and eliminating instabilities due to geometry and characteristics of the flow. As a future work, special attention will be given to the design of the inlet/nozzle designs and their applications to the FRC or tokamak like confinement configurations.

There are also additional physical mechanisms that may effect the performance of the liquid layer for free surface heat transfer and swirl decay. These mechanisms (such as, evaluation of radial distribution of turbulence intensity in free-vortex along the axial direction and its effect on swirl decay, etc) are out of the scope of the present study and are subject to future phases of ongoing effort.

Vortex Generation at Close Distance to Free Surface of a High Prandtl Liquid Layer Flow: Flibe viscosity decreases 33 % when its temperature increases from 500 to 600 °C. The density gradient and centripetal acceleration may generate two parallel layers of fluid with different thermo-physical properties moving at high velocity (~10 m/s). This condition may generate eddies/vortices at the interface of the layers and may promote turbulence. Since the temperature gradient is very steep at several mm from the surface, the enhancement of turbulence may end up increasing the heat transfer coefficient at the surface.

High heat flux at the liquid surface in combination with poor thermal conductivity may generate stratification at the liquid surface to the plasma. In combination with the high centripetal acceleration, stratification may become more dominant and may suppress the turbulence intensity close to the liquid surface facing the plasma. (This condition may result in a lower heat transfer coefficient.)

7.3.1.4 Accommodation of Penetrations with Flibe

Plasma confinement systems require access penetrations through the blanket and first wall system for plasma heating and diagnostics. Utilizing high velocity liquid layers as a first wall blanket system in these configurations makes it a challenging issue to accommodate these penetrations without disturbing the hydrodynamic characteristics of liquid layers. This preliminary analysis is aimed at determining the optimum penetration shapes and required modifications to the surrounding area of penetrations for minimum disruption to the hydrodynamic characteristics of the liquid layer. A preliminary study in accommodating penetrations in the high velocity liquid layer flow is performed in the following stages and is accomplished by:

- (1) Determining the critical issues in the penetration design and possible challenges that may arise when the penetration is located in the high velocity liquid flow.
- (2) Determining design goals.
- (3) Determining optimum penetration shapes and required modifications to the surrounding area of penetrations for minimum disruption to the hydrodynamic characteristics of the liquid layer.

The reference penetration dimensions and spatial problem domain are determined so that the hydrodynamic simulations can be performed within the capability of computational resources and reasonable computational time. The motivation in determining the reference penetration shape and problem domain is to: (1) minimize the loss of information as a result of using larger computational mesh sizes and (2) maximize the spatial problem domain to simulate a real penetration accommodation problem

In these preliminary analyses, 3-D, time-dependent Navier-Stokes solver that uses RANS method for turbulence modeling and utilizes VOF (Volume of Fluid) technique for free surface incompressible fluid flows are used. As a first step, a parametric penetration design study has been performed for a base penetration shape and dimension on a flat plate (Figure 7.3-11). The centripetal acceleration term is modeled as a constant force field with an acceleration term perpendicular to the flow direction and equal to the V_{axial}^2 / R . ($V_{axial} = 10$ m/s, $R=4.0$ m). The true gravitational acceleration is applied in the same direction of the flow. The location of the penetration can be assumed to be the mid-plane of the outboard blanket where the effect of gravitational acceleration to the liquid layer is maximum.

The preliminary results of the reference case are shown in Figure 7.3-12, as 2-d velocity vectors in the planes perpendicular to flow direction. The location of these planes with respect to penetration is shown in Figure 7.3-13. The purpose of the present

approach is to vary control variables (penetration shape, modifications to surrounding, *etc.*) to the reference design and determine the advantages of one variation over the another. Then, apply all the information obtained from this study to the final penetration case.

The main challenges will be:

A. Stagnation

- Minimizing the cooling of the front section of the penetration.
- Discharging the fluid towards the plasma from the front section.

B. Deflection

- Diversion of the rising fluid to the sides surrounding the penetration due to the obstruction of flow path. (For example, 144 m³ of fluid per hour is displaced for a 20-cm wide (in the flow direction) penetration for the CLiFF concept with a base velocity of 10 m/s.)
- Deflection of streamlines by the penetration structure results wake formation that persists downstream of the penetration itself

The proposed modifications for the penetrations can be classified in two different techniques.

A. Passive Techniques

- Modification of the back wall contour to accommodate the additional fluid that is diverted on the sides by the penetrations.
- Placing fins at various heights and angles parallel to the penetrations to divert the flow back to the end section of the penetration (eliminate the unwetted region down stream from the penetration)
- Using a fluid divertor section in the upstream section of the penetration so that sudden fluid level rises can be minimized.
- Using a sharp edge at the front section of the penetration may minimize the stagnation.

B. Active Techniques

- Using a jet at the end section penetration that has the same velocity as the liquid wall flow, in order to cover the unwetted back wall behind the penetrations.
- Using various suction and flow removal mechanisms at the upstream and guiding them back to the downstream by external flow mechanisms and pumping

Although we are aware of active techniques but are not pursuing them at the present time!

Two-Layer Groove Passive Diversion System

Two groove layers are used surrounding the penetration. The first layer (closer to the penetration) is 5 cm wide and 2 cm deep, while the second layer is 5 cm wide and 1 cm deep. The purpose is to minimize a sudden fluid level rise by increasing the flow area and to redirect the flow at the front section and back section of the penetration. The rise in

fluid level is less than that in the reference cases (6 cm as compared to more than 8 cm). Cavities do form at locations where flow area changes suddenly as the flow proceeds towards the steps of grooves. A sudden rise of the back wall level, due to the step at the end of the groove section, may result in perturbation to the liquid wall flow. Corrosion of the groove sidewalls may decrease the lifetime and minimize the possibility of continuous operation. See Figures 7.3-14 and 7.3-15.

The effect of a series of flow guiding fins placed in the upstream, mid and downstream locations was also evaluated. The guiding fins located upstream are designed to gradually divert the fluid flow away from the penetrations in order to minimize sudden displacement of fluid as it hits the penetrations. The guiding fins located at the mid-penetration are designed to redirect the diverted flow towards the penetration and minimize the potential non-uniformity in the flow away from the penetration. The guiding fins located at the downstream of the penetrations are designed to divert the flow back underneath the penetration so as not to leave any area exposed.

The fins placed closer to the penetration cause sudden reflection of fluid and therefore splash. The height of the fins may cause unwetted regions and separation as well as non-uniformity of the wall thickness due to the wake formation behind the fin. The fins closer to the end section of the penetration do not cause fluid splash. The relative angle of the fins to the flow direction is very important in eliminating wake formations behind the fins. High-speed flow may cause corrosion in the fins and maintenance and replacement times may not be feasible.

Gradual Tailoring of Back Wall Topology

Modifications to the back wall topology may result in more attractive fluid flow characteristics around the penetrations. Using a gradually increasing depth towards the penetration eliminates fluid splash and droplet ejection, directs the fluid towards downstream of the penetration and accommodates excessive fluid due to sudden obstruction of the flow. Further parametric analysis is required to obtain a uniform liquid wall thickness by modifying the concave contour depth and its distribution surrounding the penetration. Here, we investigate a concave contour whose depth slightly varies away from the penetration, becoming deepest (2.2 cm deep) near the penetration. Gradually increasing depth of the concave contour towards the penetration minimizes the disruption of the flow height in planes perpendicular to the flow direction, while accommodating maximum additional flow area to the diverted fluid near the penetration. Decreasing the radius of curvature increases the centripetal acceleration that is perpendicular to the flow direction. This condition minimizes the fluid level change in the vertical direction and redirects it in the lateral direction. Problems arising at the front section of the penetration (stagnant flow section and droplet ejection) are independent of type of hydrodynamic liquid wall configuration and can be eliminated by sharp edge or gradually increase in the height of the front section. This flow is pictured in Figures 7.3-16 and 7.3-17.

Preliminary Conclusions

There are slight differences and inherent advantages of each liquid wall concepts for various plasma confinement configurations over another as a result of configuration geometry and flow type. Problems arising at the front section of the port (stagnation and droplet ejection) are independent of type of confinement configuration.

Suggested Optimum Port Location for FRC: An elliptically shape port of dimensions (a: .2 m, b: .4 m) is used. The port is placed in the FRC chamber at an angle such that port centerline becomes parallel to the streamlines of the swirling flow. Inlet velocity in the axial direction is used as 10 m/s and in the alpha direction is used as 10 m/s from a 2.75 m radius of conical inlet that is converging to a 2 m radius. The bottom section perpendicular to the gravitational acceleration minimizes the ejection of droplets towards the plasma. Modification of the contour of the circular vacuum boundary wall slightly beyond where the flow passes the port (by forming a slight flow contraction in the radial direction) may generate a backward pressure that can eliminate wake formation.

Suggested Port Location for Tokamaks and ST Configurations: Use of vertical back wall is not suggested. Increasing the wall curvature at locations where the ports are placed is recommended. The lower half and near bottom section of the tokamak geometry may be an optimum location due to decrease in radial flow length and increasing the acceleration which is perpendicular to the flow direction.

Future work will try to optimize back-wall surface to accommodate penetrations while minimizing the disturbance to the flow and non-uniformity of the flow height. Implementing the optimized wall topology along with the optimized penetration shape to the concave back wall. Temperature distribution on the penetration walls (with a specified thickness, radiation and neutron wall loading) will be analyzed using 3-D heat transfer analysis by taking into account the convective heat transfer between fluid and solid, and conduction in the penetration structure.

Some interaction with the current drive and plasma heating community is needed to determine if severe restrictions exist in modifying the size and aspect ratio of required ports to be more hydrodynamically steam-lined.

7.3.2 Fast Liquid Layer Magnetohydrodynamics for Lithium and Sn-Li Flows

Mathematically these types of flows can be described by the Navier-Stokes equations for incompressible fluids and Maxwell's equations for electromagnetic phenomena. The numerical tools used to analyze this system of equations for the CLiFF concept are again described in Chapter 5, Section 5.4. This description will not be repeated here, except to note that the numerical solutions are based on the two-dimensional magneto-hydrodynamic equations and can be performed in practice for any values of governing parameters for ducts of various geometries. This is an extreme simplification of the physics and assumes that all currents close in each cross-sectional plane (no current along

the flow direction). This type of calculation is accurate for well-behaved, nearly fully-developed flows with simple geometries, but neglects potentially significant effects near field gradients and developing regions.

7.3.2.1 1½-D Analytical solution for the liquid metal MHD flow in an open duct with isolated side-walls

An analytical solution to the problem has been found for the case of liquid metal MHD flow in an open concave duct with isolated side-walls^a. For this case, the suppression of turbulence by the strong magnetic field is assumed, implying that $v_t = 0$ and the turbulent closure is not needed. The Hartmann solution was used in order to define both the viscous friction in the Hartmann layers and the drag Lorentz force. In doing so, the following expressions for the velocity profile function f , its derivative, and the electrical current density at the side-walls can be derived as:

$$f(z)=1-\exp\{Ha(|Z|-1)\}; \quad \partial f/\partial Z|_{Z=1}=-\partial f/\partial Z|_{Z=-1}=-Ha; \quad j_z|_{Z=1}=j_z|_{Z=-1}=0. \quad (7.3-33)$$

Using (7.3-33) and approximating the velocity profile in the y-direction with a parabola:

$$U(x,y) = a(x) y^2 + b(x) y + c(x), \quad (7.3-34)$$

gives the equations for the layer thickness and the pressure at the solid wall, P_w (scaled by ρU_0^2) as follows:

$$\frac{dh}{dx} = \frac{\frac{3}{Re} \frac{1}{h^2} + \frac{Ha}{Re} \beta^2 - \frac{\sin(\alpha + \alpha_0)}{Fr} h}{\frac{6}{5} \frac{1}{h^2} + \frac{\cos(\alpha + \alpha_0)}{Fr} h}; \quad (7.3-35)$$

$$P_w = \frac{6}{5} \chi \frac{1}{h} - \frac{\cos(\alpha + \alpha_0)}{Fr} h. \quad (7.3-36)$$

The equation (7.3-35) calculates changes in the thickness of the layer over the flow domain, while the expression (7.3-36) gives the criterion for the flow separation from the structural wall. If P_w is positive, the separation does not occur. If it becomes negative, the layer no longer adheres to the structural wall. In the subsequent discussions the conditions $h < 2$ and $P_w > 0$ are used as the criteria for choosing flow parameters which meet the concept requirements.

It should be noted that for the case with complete toroidal axi-symmetry, that no side-walls are present and so no Hartmann layer friction occurs. In such a case, β essentially

^a The term side-walls used in this chapter denotes walls that break-up the FW flow into toroidal sectors, and does not (necessarily) reflect the common MHD convention of denoting side-walls as walls that are parallel to the applied magnetic field where side-layers can develop

goes to zero and the effect of the toroidal field drops out entirely. The selection of a parabolic profile in y is especially relevant to cases with very small or vanishing β .

Similar analytic solutions for dh/dx and P_w can also be found using another velocity approximation:

$$U(y) = 1 - \exp(-\beta Ha^{0.5} y), \quad (7.3-37)$$

which gives more accurate results for larger values of $Ha\beta^2 > 10$. This profile takes into account the formation of a gradient velocity layer at the structural wall with the thickness proportional to $\beta Ha^{0.5}$. Using Eq. (7.3-37) the following equations were obtained:

$$\frac{dh}{dx} = \frac{\frac{1}{h} \beta \frac{\sqrt{Ha}}{Re} + \frac{Ha}{Re} \beta^2 - \frac{\sin(\alpha + \alpha_0)}{Fr} h}{\frac{1}{h^2} + \frac{\cos(\alpha + \alpha_0)}{Fr} h}, \quad (7.3-38)$$

$$P_w = \frac{\chi}{h} - \frac{\cos(\alpha + \alpha_0)}{Fr} h. \quad (7.3-39)$$

In both cases we note that the centrifugal force term does not enter either the equations Eqs. (7.3-35) or (7.3-38) and hence does not have an impact on the thickness of the layer. This is not the case if the radius of curvature is not constant, and instead varies as a function of poloidal angle. This case however is not analyzed here but may be an advantageous design modification. The curvature does, however, enter the expressions for the pressure distributions at the structural wall, namely Eqs. (7.3-36) and (7.3-39).

Numerical calculations based on the formulas (7.3-35), (7.3-36) and (7.3-38), (7.3-39) show approximately the same results as obtained earlier in [16] by using simpler solutions that are based on a hydraulic approximation. These results confirmed that the desired flow which meets both requirements, $0.5 < h < 2$ and $P_w > 0$, over the whole flow domain can be established in this simplified field geometry

7.3.2.2 2-D Numerical solutions

Although the above analytic formulas (or similar formulas based on the hydraulic approximation [16]), can be used to calculate the layer thickness as well as the pressure distribution over the structural wall, their applicability to the CLiFF concepts is restricted because of several reasons. First, they do not allow accurate calculations of velocity profiles, which are needed in the heat transfer calculations. Second, they are applicable to the case of electrically isolated side-walls only. This is rather restrictive since the effect of electrically conducting walls on the flow is not negligible. On the contrary, it can

change flow characteristics drastically. Therefore, more detailed calculations using a more accurate approach, like the numerical code for solving the problem for liquid metal flows described in the Chapter 5, become necessary.

Figure 7.3-18 presents numerical results for the thickness of the layer calculated with CLiFF parameters for lithium. The main flow parameters used in the calculations are presented in Table 7.3-4 (dimensional) and in Table 7.3-3 (dimensionless). In the same figure two other curves are plotted (2 and 3) to illustrate the analytical solutions Eqs. (7.3-38) and (7.3-35). Although all three curves are close, the analytical solution based on the Hartmann-type velocity approximation, Eq. (7.3-37), gives better results than the parabolic approximation for this case with relatively large $\text{Ha}\beta^2$.

The results of the calculations for both the isolated side-walls case (upper) and the conducting side-walls case (lower) are presented in Figure 7.3-19. The wall conductance ratio $c_w = \sigma_w t_w / (\sigma b)$ is chosen to be 10^{-6} . It should be mentioned that real values for this parameter could be much larger. For example, $c_w \approx 0.02 - 0.2$ for most metal walls and $10^{-4} - 10^{-5}$ for the walls made of silicon carbide^b. Hence, the value of 10^{-6} can be interpreted as that corresponding to a conducting wall with a thin isolating coating.

Both velocity profiles and changes in the film thickness over the flow domain are quantitatively and qualitatively different between isolated and conducting side-walls. In the case of isolated walls, the velocity profiles demonstrate a thin gradient layer (side-layer) at the structural wall with the thickness proportional to $\beta\text{Ha}^{0.5}$, while in the core of the flow the velocity is of a slug type. This observation confirms the assumption of Eq. (7.3-37) made earlier on the Hartmann-type velocity profiles in the y-direction, and it explains why using Hartmann-type velocity approximation gives better results for the layer thickness than the parabolic approximation (for high $\text{Ha}\beta^2 > 10$). The increase in the thickness of the layer over the flow domain caused by MHD effects is not significant in this case, and both criteria on h and P_w are met.

It is well known that the presence of electrically conducting walls can lead to larger electrical currents in the flow domain and, as a result, to a significant increase in the MHD drag effect. Figure 7.3-19 shows results illustrating the effect of conducting sidewalls on the velocity profiles and the layer thickness. The "M-shape" in the velocity profiles seen in the figure is caused by the Lorentz force, which is distributed non-uniformly over the layer height, with minimums at the back-wall and the free surface. The layer thickness also increases due to the increased drag. We ask ourselves two questions to attempt to quantify this effect for CLiFF. First, what is the maximum side wall conductance ratio, c_w , meeting the criterion $h < 2$? Second, if the side-walls are metallic or non-metallic (made for example of silicon carbide), what is the minimum allowable distance between them, $2b$?

^b The electrical conductivity of SiC assumed here is in the range $100 - 1000 \text{ } \Omega^{-1}\text{m}^{-1}$ which is (arguably) typical for composites and monolithic SiC at high temperatures and after irradiation, but tends to be at the high end of the spectrum. The potential to produce lower electrical conductivity SiC certainly exists and is desirable for CLiFF side-walls. Values as low as $\sigma = 0.001$ have been reported for room temperature SiC which is more than adequate for this application.

In order to answer these two questions, computations were carried out using the CLiFF set of the flow parameters (see Tables 7.3-3,4). It was assumed that the side-walls are metallic with the thickness of 1-10 mm or made of silicon carbide with the thickness of 5-20 mm. The wall conductance ratios in these two cases are 0.02 - 0.2 (metal) or $(1.0 - 4.0) \times 10^{-4}$ (SiC). If the distance between two side-walls is 1 m, as it has been chosen in CLiFF, the criterion $h < 2$ is not satisfied for c_w greater than 2.0×10^{-6} (Figure 7.3-20), and therefore neither metal or SiC side-walls can be used. So, a tentative conclusion is drawn that only electrically isolated side-walls are reasonable (again, see footnote). Turning to the second question, if SiC side-walls are employed given the above dimensions, the distance between them has to be more than 8 m. The metallic side-walls require much larger distance, no less than 110 m. From the practical point of view, these results mean that either the flow must not be sectioned (no side-walls) or the side-walls must be isolated or at least be quite far apart for the case of SiC.

Although conducting side-walls in the presence of the toroidal magnetic field affect the flow significantly through the MHD interaction within the Hartmann layers at these walls, the influence of the conducting back-wall is negligible unless a radial (free surface normal) field component exists. Estimations for the effect of the conducting back-wall caused by the MHD interaction between the induced electrical current and the radial field component were carried out using a different Hartmann-type MHD model taking into account only one small, but not negligible, radial component of the magnetic field (see Fig. 7.3-21). The problem was solved numerically for the flow parameters relevant to CLiFF using a finite-difference algorithm similar to that described in Chapter 5.

If it is assumed that the flow has isolated side-wall dividing the flow into toroidal sectors (preventing currents from closing around the torus, but at a great enough distance that the Hartmann effect discussed above is relatively small), then the wall conductance ratio of the back-wall plays a dominant role (Figure 7.3-22). The design window is illustrated in Figure 7.3-23, where the maximum layer thickness is plotted against the back-wall conductance ratio ($c_w = t_w \sigma_w / \sigma h_o$)^c for different Hartmann numbers. The horizontal solid line shows the acceptable limit in the layer thickness. By analyzing this plot, the following conclusions can be drawn on the back-wall conductivity. First, the metal back-wall is acceptable if the radial magnetic field is no more than 0.1-0.15 T. Second, for the radial magnetic field from 0.15-0.2 T the back-wall made of silicon carbide can be used. Third, if the radial magnetic field is larger than 0.5 T even an isolated back-wall is unacceptable.

If the flow is assumed to be axi-symmetric with no dividing side-walls, then induced currents in the toroidal direction no longer need a return current path and simply close on themselves. In this case, corresponding in the analysis of the preceding paragraph to a perfectly conducting backwall, the maximum allowable radial field is $B = 0.015$ T. This restriction means that flow will need to conform very closely to flux surfaces or toroidal

^c Note that this definition uses the layer depth instead of width for the liquid length scale

sectioning with side-walls will be required. Another option is that some alternate means to drive the flow (*e.g.* from applied electric currents) will need to be considered.

7.3.2.3 Surface and boundary layer instabilities

Results of the instability analysis for thin liquid metal layers flowing down inclined chutes in a transverse magnetic field show that this type of free surface flow does demonstrate MHD instability except in some particular cases where there are very small distances between the side-walls or very small flow velocities [17]. The analogous flows over concave surfaces, to our knowledge, have not been studied yet. Nevertheless, they will probably demonstrate the same type of hydrodynamic instability. In some cases, the surface instability can be a negative factor, since it can lead to the layer disintegration, and therefore some additional means for the instability suppression might be necessary.

In the present analysis of surface instability, two different approaches to the problem, analytical and numerical, were developed. Using the analytical approach based on the linear analysis, the approximate solution for the wave growth rate was found, which allows one to draw some qualitative conclusions about the instability process. Although this approach is very informative as it allows finding the parameters responsible for the wave growth or for its suppression, it is more qualitative primarily because of its linear character. On the other hand, the numerical approach allows more accurate analysis, including information on the wave growth in time and space depending on finite amplitude initial disturbances.

The stability analysis is done using some assumptions. The mathematical model of Chapter 5 based on the shallow water approximation is used. The consideration is restricted to the case of electrically isolated side-walls. The case of electrically conducting walls is not considered in accordance with the previous conclusions, since the electrically conducting walls cause a significant MHD drag force. Only long wave disturbances are taken into account in the stability analysis, as short wave disturbances are suppressed quickly by the surface tension.

Usually in the linear stability analysis based on the flow equations like those in the Chapter 5, the solution of the equation for perturbations is sought in the form of series in powers of a small parameter. For example, in [17], the small parameter is the wave number, which is less than unity, since only long wave disturbances are considered. The zero and the first order approximations are usually enough to get the critical wave number and the wave increment. In the present study, a simplified approach was applied to the problem based on a one-dimensional form of the equations, which requires less mathematics. The procedure of deriving these equations is explained below.

Typically, in a strong magnetic field, the free surface flow, bounded by the structural wall and the two electrically isolated side-walls, is broken up into a inviscid core, with Hartmann boundary layers at the side-walls and a gradient (*i.e.* side-) layer at the back-wall. By integrating the governing Navier-Stokes-Maxwell equations along the direction of the toroidal magnetic field, the two-dimensional equations were derived. In the same

manner, by again integrating the two-dimensional equations in the surface normal direction, simplified one-dimensional equations can be obtained as follows:

$$\begin{aligned} \frac{\partial U}{\partial t} + U \frac{\partial U}{\partial x} = \frac{1}{Fr} [\cos(\alpha + \alpha_0) \frac{\partial h}{\partial x} + \sin(\alpha + \alpha_0)] + 0.5 \frac{\gamma}{h} \frac{\partial}{\partial x} (Uh)^2 - \\ - (\beta^2 \frac{Ha}{Re} + \frac{1}{h} \beta \frac{\sqrt{Ha}}{Re}) U + \frac{1}{We} \frac{\partial^3 h}{\partial x^3}; \end{aligned} \quad (7.3-40)$$

$$\frac{\partial h}{\partial t} + \frac{\partial Uh}{\partial x} = 0. \quad (7.3-41)$$

When deriving the equations (7.3-40,41) the velocity distribution in the form of the Eq. (7.3-37) is assumed.

An ordinary linear approach for studying a stability problem is that the governing equations are linearized in the vicinity of the equilibrium solution, which corresponds to the fully developed flow regime. In the case under consideration, there is no equilibrium solution as the flow is developing over the whole flow length. Nevertheless, the stability analysis can be conducted assuming a locally fully developed flow (the solution of (7.3-40,41) where the terms $\sin(\alpha + \alpha_0)$ and $\cos(\alpha + \alpha_0)$ are "frozen"). Following this approach, the solution is sought as a sum:

$$U = U_1 + U', \quad h = h_1 + h', \quad (7.3-42)$$

where U_1 , h_1 and U' , h' are the locally fully developed solution and the perturbations correspondingly. Substituting (7.3-42) into the equations (7.3-40,41) and linearizing them, one can obtain two equations for U' and h' . The solutions of these linearized equations have the following form

$$h' = \exp\{\omega t\} \sin k\xi \quad (7.3-43)$$

$$U' = \left[\frac{\omega}{h_1 k} \cos k\xi + \frac{v}{h_1} \sin k\xi \right] \exp\{\omega t\}, \quad (7.3-44)$$

where:

- ω is the increment (decrement);
- k is the wave number ($\lambda = 2\pi/k$);
- v is the phase velocity;
- $\xi = x - (U_1 + v)t$.

Two equations for k and v were obtained as follows:

$$\omega^2 + \lambda\omega - \gamma = 0; \quad v = \frac{U_1^2 \beta \sqrt{Ha} / Re - \chi\omega}{2\omega + \beta^2 Ha / Re + U_1 \beta \sqrt{Ha} / Re} \quad (7.3-45)$$

where:

$$\lambda = \beta^2 \frac{Ha}{Re} + \frac{1}{h_1} \beta \frac{\sqrt{Ha}}{Re}; \quad (7.3-46)$$

$$\gamma = [v^2 + \chi(U_1 + v) + \frac{\cos(\alpha + \alpha_0)}{Fr} h_1] k^2 - \frac{k^4 h_1}{We}. \quad (7.3-47)$$

As v is not equal to zero, the surface waves propagate with a velocity different from that of the non-disturbed flow. It also can be seen from the equation for v that the surface waves are dispersive; that is, their velocity depends on the wavelength. The solution of the quadratic equation (7.3-45) is as follows:

$$\omega_{1,2} = 0.5(-\lambda \pm \sqrt{\lambda^2 + 4\gamma}) \quad (7.3-48)$$

Analysis of Eqs. (7.3-45)-(7.3-48) can provide some conclusions.

If the parameter $\beta^2 Ha / Re$ is large enough, $\lambda^2 \gg |4\gamma|$, and hence $\omega_1 = \gamma/\lambda$ and $\omega_2 = -\lambda$. This means that the strong magnetic field has a stabilizing effect on the flow. Nevertheless, as simple calculations show, the condition $\lambda^2 \gg |4\gamma|$ is not satisfied and thin liquid wall flows are unstable. The surface tension tends to suppress perturbations especially those having short wavelengths, while the effect of gravitation depends on the angle α . It can be expected that the disturbances will grow in the upper half ($0 \leq \alpha + \alpha_0 \leq \pi/2$) where $\cos(\alpha + \alpha_0)$ is positive and will propagate with slightly decreasing amplitude in the lower part ($\pi/2 \leq \alpha + \alpha_0 \leq \pi$) where $\cos(\alpha + \alpha_0)$ is negative. The centrifugal force always tends to destabilize the flow.

The results of computations based on the numerical solution of the above equations are presented in Figure 7.3-24. All computations were carried out for thin liquid wall concept using flow parameters from the Tables 7.3-3,4. The flow was perturbed through the boundary condition in the inlet cross-section. The disturbances were specified as the perturbations of the mean velocity without perturbations of the flow-rate: $U_{in} = 1 + \epsilon \sin(\omega t)$; $h_{in} U_{in} = 1$. In all variants the dimensionless amplitude was 0.05, while the parameter ω (wave number) was changed from 0.02 to 0.5. Corresponding to the changes in ω , the wavelength λ varied from 4.5 to 0.2 m. The results of computations are in a good agreement with the linear stability analysis conclusions. The initial disturbances grow very rapidly in the upper part under the effect of gravity and centrifugal acceleration and then propagate down with slowly decreasing amplitude. The growth rate and the maximum amplitude depend on the wavelength. The short waves are suppressed rapidly by the surface tension, while the long wave disturbances are not suppressed over the whole flow length. It can be seen that the disturbances with the wavelength smaller

than 20 cm are suppressed rapidly within the distance of about 1.5 - 2 m and practically do not affect the flow. The most dangerous disturbances are those having the long wavelength of about 2 m, for which the amplitude can reach 40-50% of the initial flow depth. The layer disintegration or other negative effects like the flow separation or the excessive increase in the thickness do not accompany the wave propagation. Therefore, special means to suppress surface instability are not needed. The only requirement is to provide inlet fluctuations at the level less than 5-10%, which can probably be accomplished without significant difficulty.

7.3.2.4 Accommodations of penetrations in LM flow with MHD effects

Due to the complexity of the problem, no detailed work has yet been done in the area of accommodation of penetrations in LM flow. Such penetrations represent MHD flow with a disturbance to the hydrodynamic flow field via the physical diversion of liquid from its initial course, and also, and more significantly, a disturbance to electrical current paths that potentially can overwhelm the flow with local and global MHD drag. Preliminary conclusion of the effect of penetrations can be gleaned from the discussion of side-walls above. The conclusion drawn is that any penetration will require an insulator coating to isolate the penetration for the free surface flow.

References for Section 7.3

1. Jones W.P., Launder B.E., The Prediction of Laminarization with a Two-Equation Model of Turbulence, *Int. J. Heat and Mass Transfer*, **15**, 301 (1972).
2. Kitamura K., Hirata M. Turbulent Heat and Momentum Transfer for electrically conducting Fluid Flowing in Two-Dimensional Channel under Transverse Magnetic Field, 6th Int. Heat Transfer Conf., **3**, 159 (1978).
3. Naot D., Rodi W. Calculation of Secondary currents in Channel Flow, *Proc. ASCE*, **108**, No.HY8, 948 (1982).
4. Naot D., Yacoub N., Moalem D. Dissipation Length Scale Dynamics, *Liquid Metal Flows and Magnetohydrodynamics: Progress in Astronautics and Aeronautics*, **221** (1991)
5. Morley N.B., Gaizer A.A., Tillack M.S., Abdou M.A., Initial liquid metal magnetohydrodynamic thin film flow experiments in the MeGA-Loop facility at UCLA, *Fusion Engr. Design*, **27** (1995) 725.
6. Kelsall, D. F., A Study of the Motion of Solid particles In a Hydraulic Cyclone, *Trans. Instn. Chem. Engrs.*, Vol. 30, 1952.
7. Bradley, D., *The Hydrocyclone*, Pergamon Press, First Edition, 1965.
8. Wang S., Rusak Z., 1996, On the Stability of an Axisymmetric Rotating Flow in a Pipe, *Physics of Fluids*, Vol. 8 (4), pp. 1007-1016.
9. Ligrani P.M. et al., 1998, Flow Phenomena in Swirl Chambers, *Experiments in Fluids*, Vol. 24., pp. 254-264.
10. Lamb H., 1960, *Hydrodynamic Stability*, Cambridge University Press, p 8-9.
11. Tani I, 1962, Production of Longitudinal Vortices in the Boundary layer Along a Concave Wall, *Journal of Geophysical Research*, Vol. 67, No. 8, pp. 3075-3080.

12. Ramaprian, B. R., Shivaprasad, B. G., 1978, The structure of Turbulent boundarylayers Along Mildly Curved Surfaces, J. Fluid Mech., Vol. 85, Part 2, pp. 273-303.
13. Bradshaw P., Muck K.C., Hoffman P.H., 1985, The Effect of Concave Surface Curvature On Turbulent Boundary Layers, J. Fluid Mech., Vol. 161, pp. 371-403
14. Brennen C., 1970, Cavity Surface Wave Patterns and General Appearance, J.Fluid Mech., Vol.44, part 1, pp.33-49.
15. Hassberger J.A, 1983, Comparison Between Measured and Predicted Performance of a High Speed Free Surface Liquid Jet Flowing along a Curved Wall, Nucl. Technol. Fusion, Vol. 4, pp. 433-438.
16. Ying A., Morley N., Gulec K., Nelson B., Youssef M. and Abdou M. Concept Description and Thermalhydraulics of Liquid Surface FW/Blankets for High Power Density Reactors, Fusion Technology, 34, 3, Pt. 2, 855 (1998).
17. Aitov T.N., Kirillina E.M., Tananaev A.V. Stability of the Flow of a Thin Layer of Liquid Metal in a Coplanar Magnetic Field, Magnetohydrodynamics, 1, 5 (1988)

Table 7.3-1: Flow and heat transfer parameters for a typical CLiFF case

Properties		Flibe (500C)	Lithium (400C)	Lithium-Tin
Composition	Mole %	66% LiF, 34% BeF ₂	100% Li	80% Sn, 20% Li
Melting Point, T _m	K	733	459	599
Density, ρ	Kg/m ³	2036	490	6761
Dynamic Viscosity, μ	Kg/m/s	0.015	4.02 × 10 ⁻⁰⁴	1.80 × 10 ⁻⁰³
Electrical Cond., σ	1/Ω.m	155	3.19 × 10 ⁺⁰⁶	1.85 × 10 ⁺⁰⁶
Thermal Cond., k	W/m.K	1.06	50.41	32.60
Specific Heat, C _p	J/kg.K	2380	4209.76	263.34
Surface Tension, γ	N/m	0.2	0.366	0.51
CLiFF Parameters				
Film Depth, h	m	0.02	0.02	0.02
Film Velocity, V	m/s	10	10	10
Channel ½ Width, w	m	1	1	1
Flow Length, L	m	8	8	8
Toroidal Field, B _T	T	8	8	8
Radial Field, B _R	T	0.2	0.2	0.2
Radius of Curvature, R	m	3	3	3
Dimensionless Numbers				
Aspect ratio, β	h/w	0.02	0.02	0.02
Reynolds No., Re	h.V.ρ/μ	2.71 × 10 ⁺⁰⁴	2.44 × 10 ⁺⁰⁵	7.51 × 10 ⁺⁰⁵
Hartmann No., Ha _T	B _T .w.(σ/μ) ^½	8.13 × 10 ⁺⁰²	7.13 × 10 ⁺⁰⁵	2.57 × 10 ⁺⁰⁵
Radial Hartmann, Ha _R	B _R .h.(σ/μ) ^½	4.07 × 10 ⁻⁰¹	356	128
Interaction parameter, N	B _T ² .σ.h/ρ.V	0.01	831	35
Vert. Froude No., Fr _v	V ² /gL	1.28	1.28	1.28
Cent. Froude No., Fr _c	R/h	150	150	150
Thermal Diffusivity, α	k/C _p .ρ	2.19 × 10 ⁻⁰⁷	2.44 × 10 ⁻⁰⁵	1.83 × 10 ⁻⁰⁵
Prandtl No., Pr^a	C_p.μ/k	33	0.034	0.015
Modified Hartmann^b	Ha_T.β²	0.33	285	102
Modified Reynolds^c	Re/Ha_T.β	1667	17	146
Force Ratio, F_c/F_{grav}^d	V²/gR	3.40	3.40	3.40

^aPrandtl Number scales importance of convective motion on heat transfer

^bModified Hartmann Number scales amount of MHD drag (< 1 indicates little drag)

^cModified Reynolds Number scales amount of Turbulence (> 500 indicates turbulence)

^dForce Ratio scales amount of centrifugal adhesive force (> 1 indicates adhered flow)

Table 7.3-2: Table of dimensions, operational parameters and related (magneto)-hydrodynamic dimensionless numbers.

Proposed Liquid Wall Configurations →	THICK WALL	THIN WALL	SWIRL FRC
Operational/Dimensionless Parameters			
Inlet Velocity U (m/s) (axial)	10.0	10.0	12.0
V (m/s) (alpha)			12.0
Dimensions D (m)	.45	.2	.5
Radius (m)	3.5	3.5	1.75
Chamber Length (m)			12.0
Ohnesorge Number (10^{-4})	8.7	4.13	8.7
Reynolds Number Re	789,500	35,000	243,000
Weber Number We	474,500	20,980	759,500
Froude Number Fr _g	22.65	510	29.35
Modified Froude No Fr _c	7.77	170	3.5
Magnetic Field, B T	10	10	4
Hartmann No, Ha	567	25	252
Interaction No, N	.4	0.018	0.006
Working Fluid	Flibe	Flibe	Flibe
Temperature (°C)	550	550	550
Density ρ (kg/m ³)	2035	2035	2035
Viscosity μ (kg/m s)	0.0116	0.0116	0.0116
Surface Tension σ (N/m)	0.194	0.194	0.194
Prandl Number $c_p\mu/k$	26	26	26
Pe 10^{+6}	20.53	20.53	20.53
Electrical Cond. σ (Ωm) ⁻¹	184	184	184
Hartmann Factor $(\sigma/v\rho)^{1/2}$	126	126	126
Interaction Factor (σ/ρ)	0.09	0.09	0.09
Magnetic Viscosity $(\sigma\mu)^{-1}$.468	.468	.468
Magnetic Re (UD/v_m)	9.61	.427	.427
Magnetic Prandtl No $(\sigma\mu^2/\rho) 10^{-6}$	12.1	12.1	12.1
$\delta_T/L 10^{-4}$	2.2	2.2	2.2
$\delta_v/L 10^{-3}$	1.125	1.125	1.125
δ_m/L	.385	.385	.385

Table 7.3-3: Dimensional flow parameters (Lithium, thin wall)

U_0	h_0	b	R	α_0	$\Delta\alpha$
m/s	m	m	m	degree	degree
10.0	0.02	0.5	4.0	30	120

Table 7.3-4: Dimensionless flow parameters (Lithium, thin wall)

Re	Fr	Ha	We	β	χ
$2.35 \cdot 10^5$	500.0	$4.53 \cdot 10^5$	12771	0.04	0.005

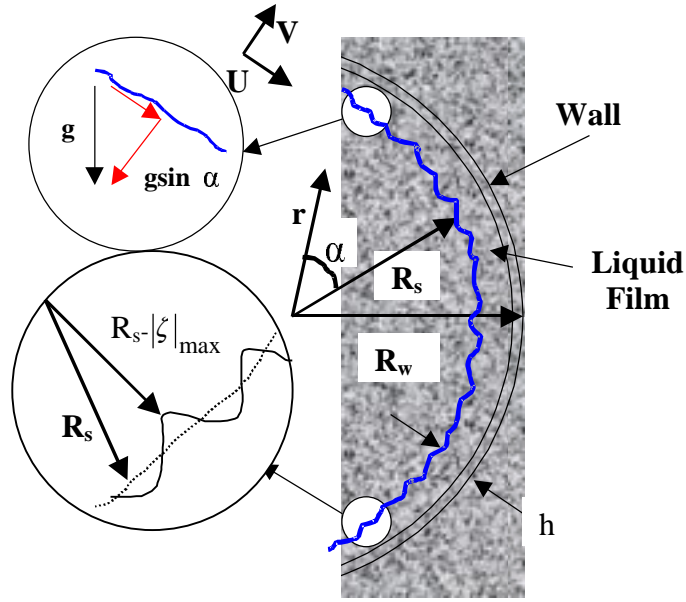


Figure 7.3-1 Simplified cylindrical geometry for hydraulics calculations of thin films.

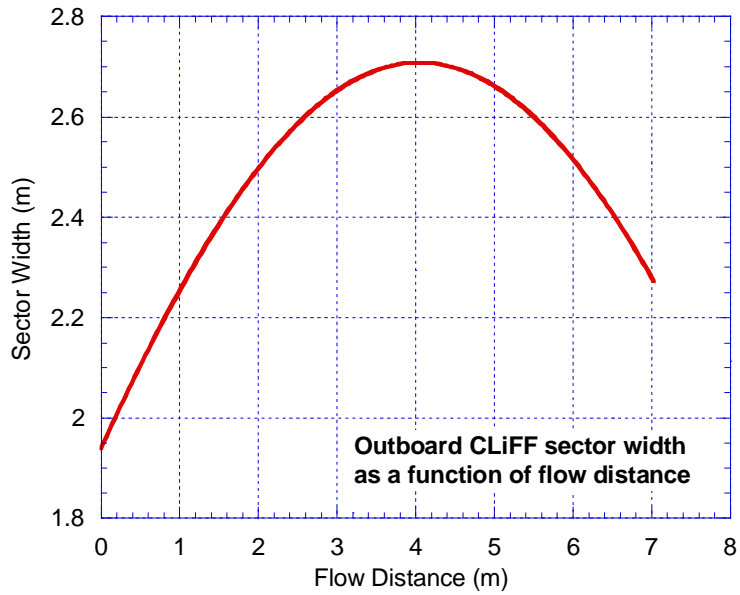


Figure 7.3-2: Sector Width of an Outboard Module.

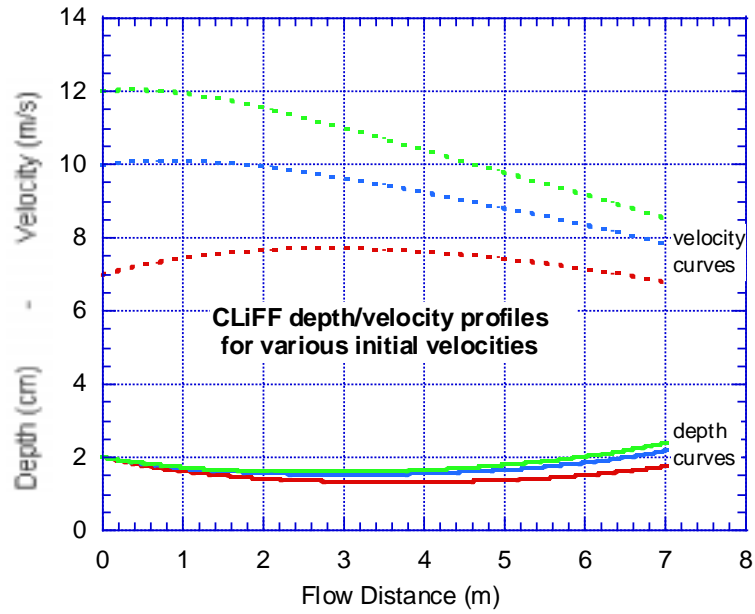
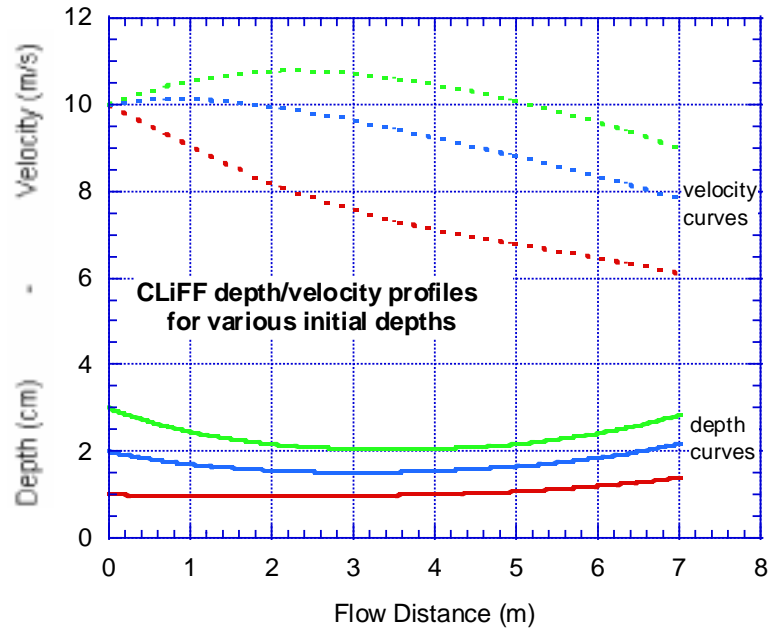


Figure 7.3-3: Results of simplified hydraulic calculations for Flibe flow on cylindrical backing wall.

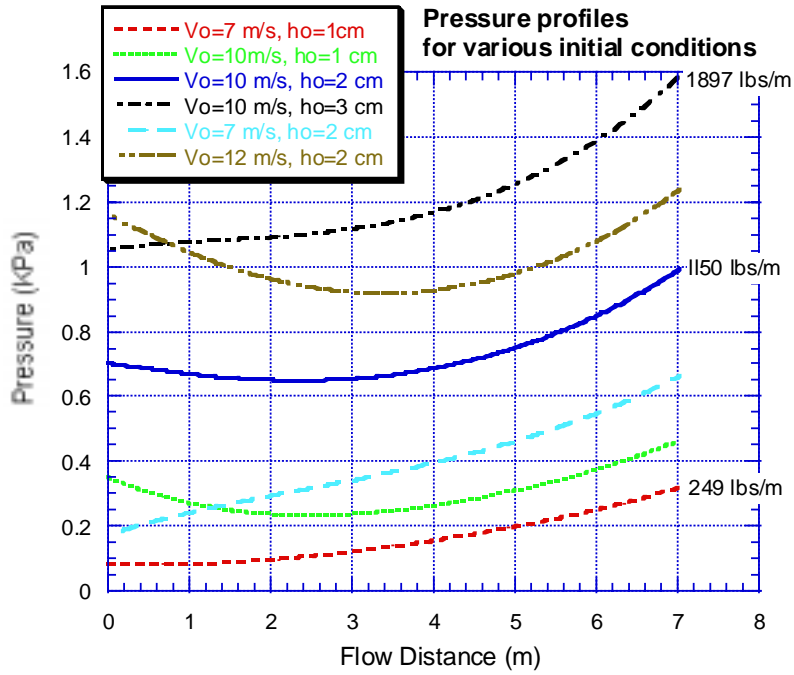


Figure 7.3-4: Pressure distribution on the back wall for various initial flow configurations.

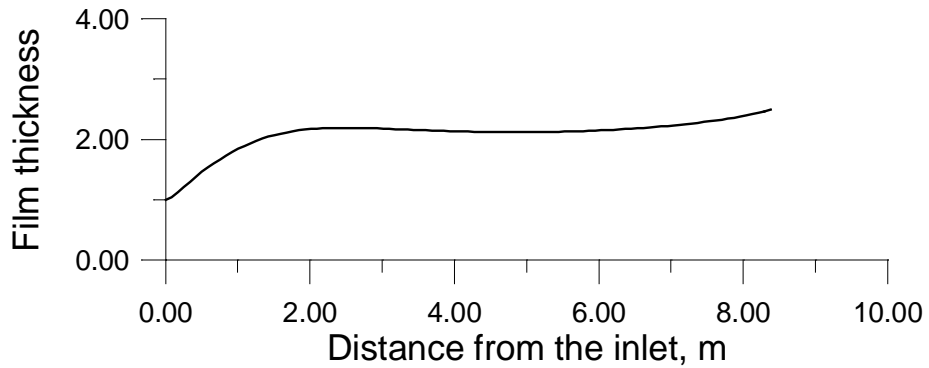


Fig.7.3-5: Turbulent CLiFF layer thickness calculated from the k-ε model.

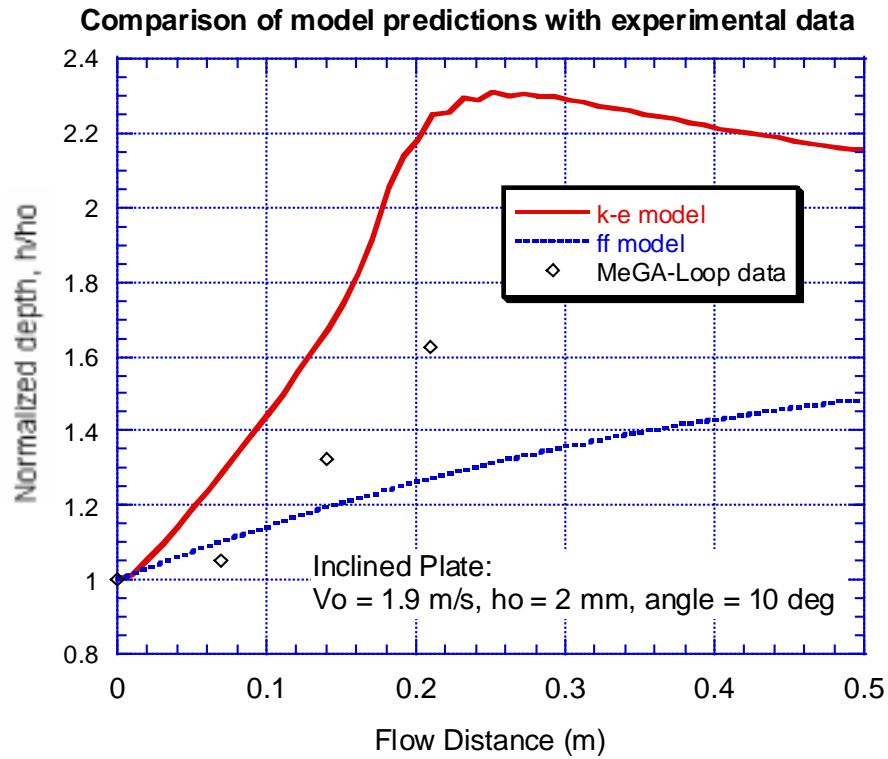


Figure 7.3-6: Comparison of data on turbulent liquid film height from MeGA-Loop experiment to k-e and simple friction factor models

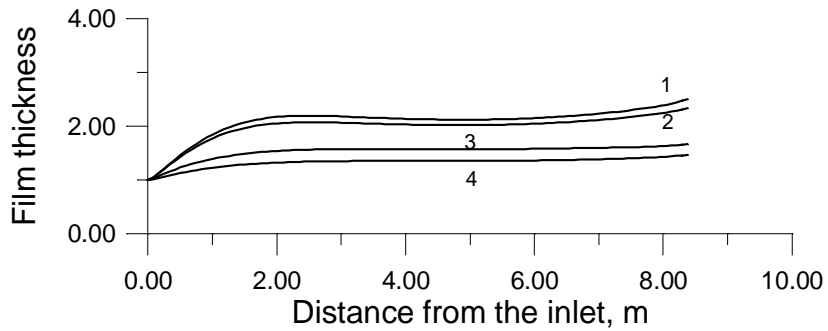


Figure 7.3.7: Effect of magnetic field on Flibe layer depth
1- Ha=0; 2- Ha=560; 3- Ha=2000; 4- Ha=3000

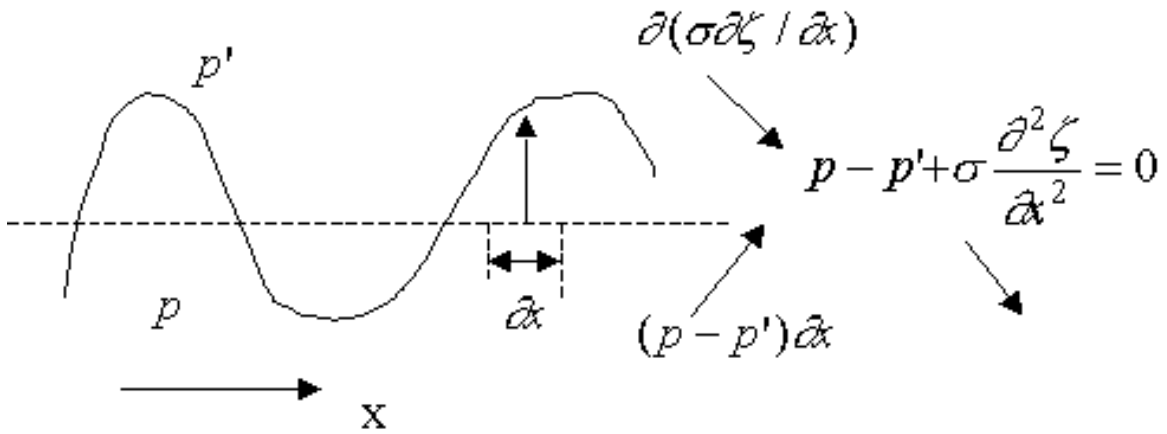


Figure 7.3-8: 2-D (Cartesian geometry) modeling for pressure perturbation at the wavy surface when surface tension is taken into account.

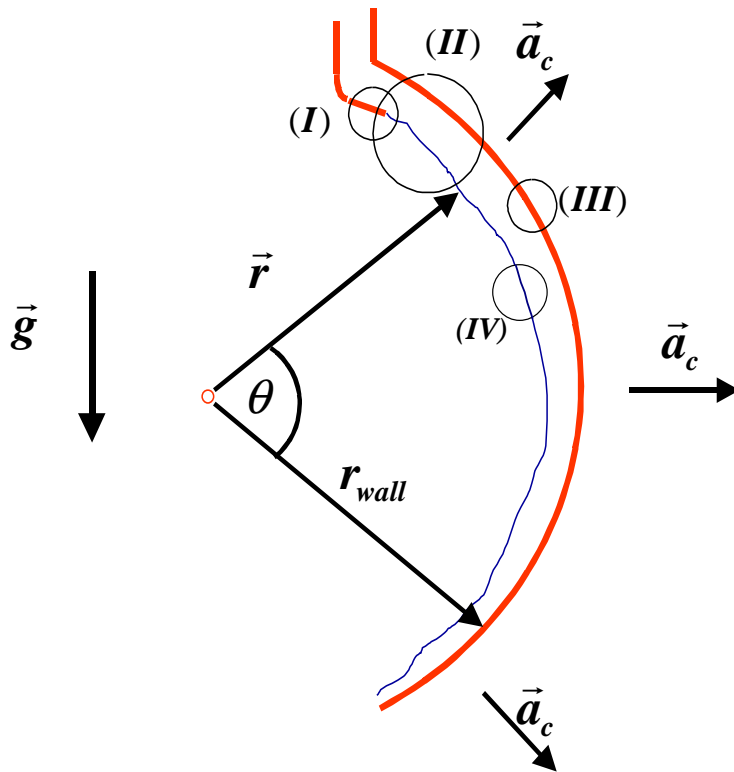


Figure 7.3-9: Eddy generating mechanisms of a high velocity liquid-layer flow over a concave surface.

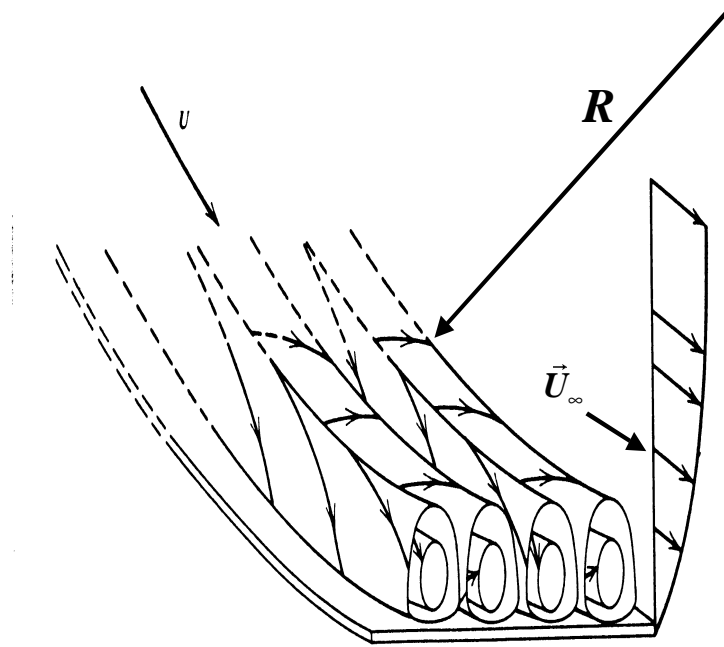
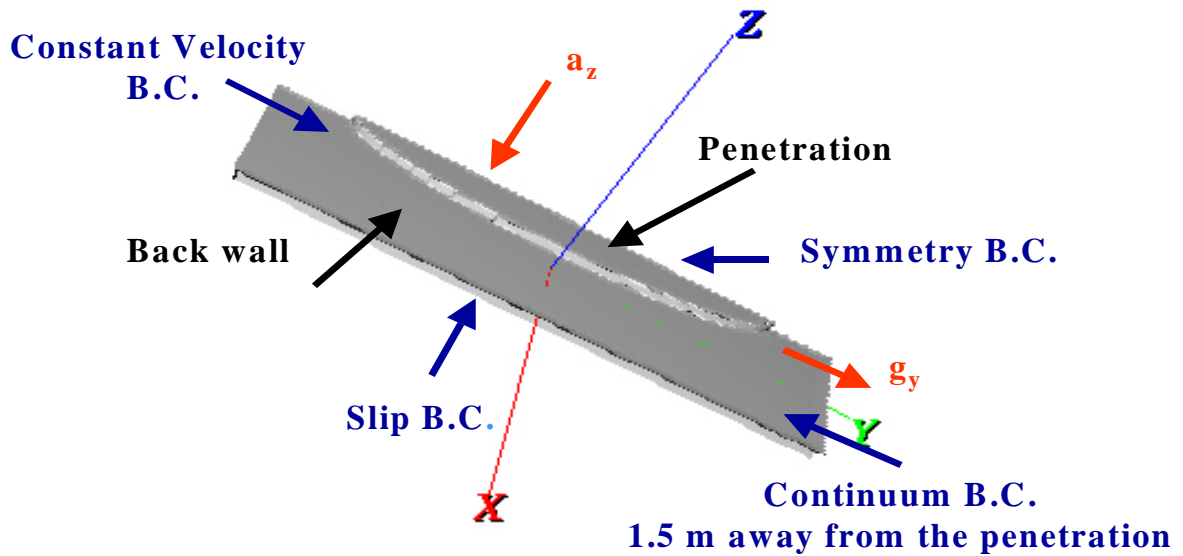
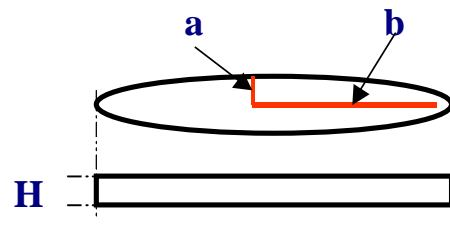


Figure 7.3-10: Gortler vortices formation in the boundary layer flow over a concave surface.



a)

V_{in} (m/s)	10.0		
a_z (m ² /s)	25.0		
g_y (m ² /s)	9.8		
Wall Roughness (m)	10^{-5}		
Fluid-Wall Contact Angle	0.0		
Penetration Dimensions (m)	a	b	H
	.1	.45	0.02



b)

Figure 7.3-11: a) Location of penetration with respect to direction of gravitational acceleration and boundary conditions used for accommodation of penetrations in the base case. b) Liquid wall operational parameters and shape/dimensions of penetration used in the base case.

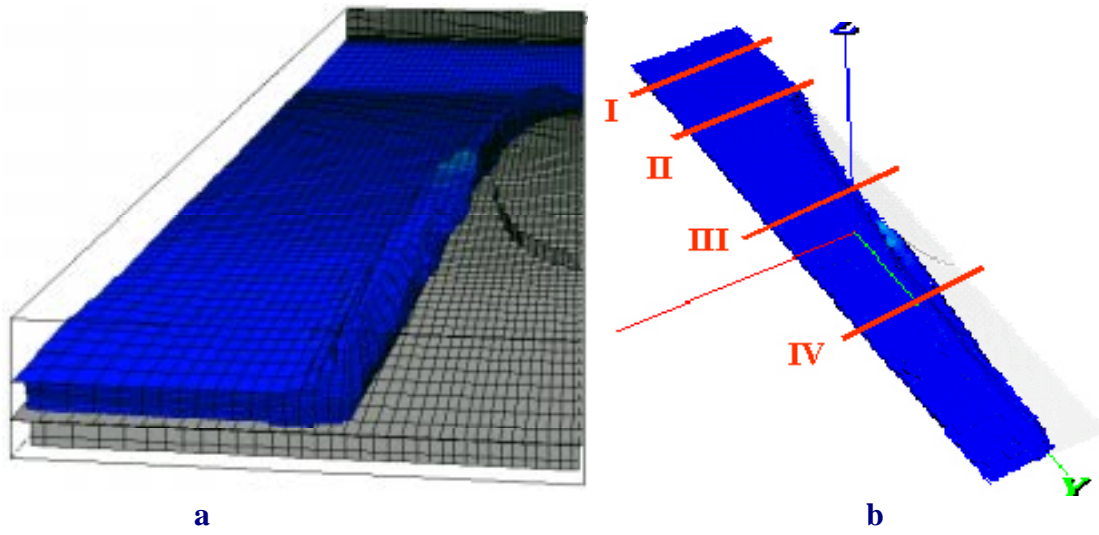


Figure 7.3-12: Perspective view of flow around an elliptical penetration with no backwall contouring.

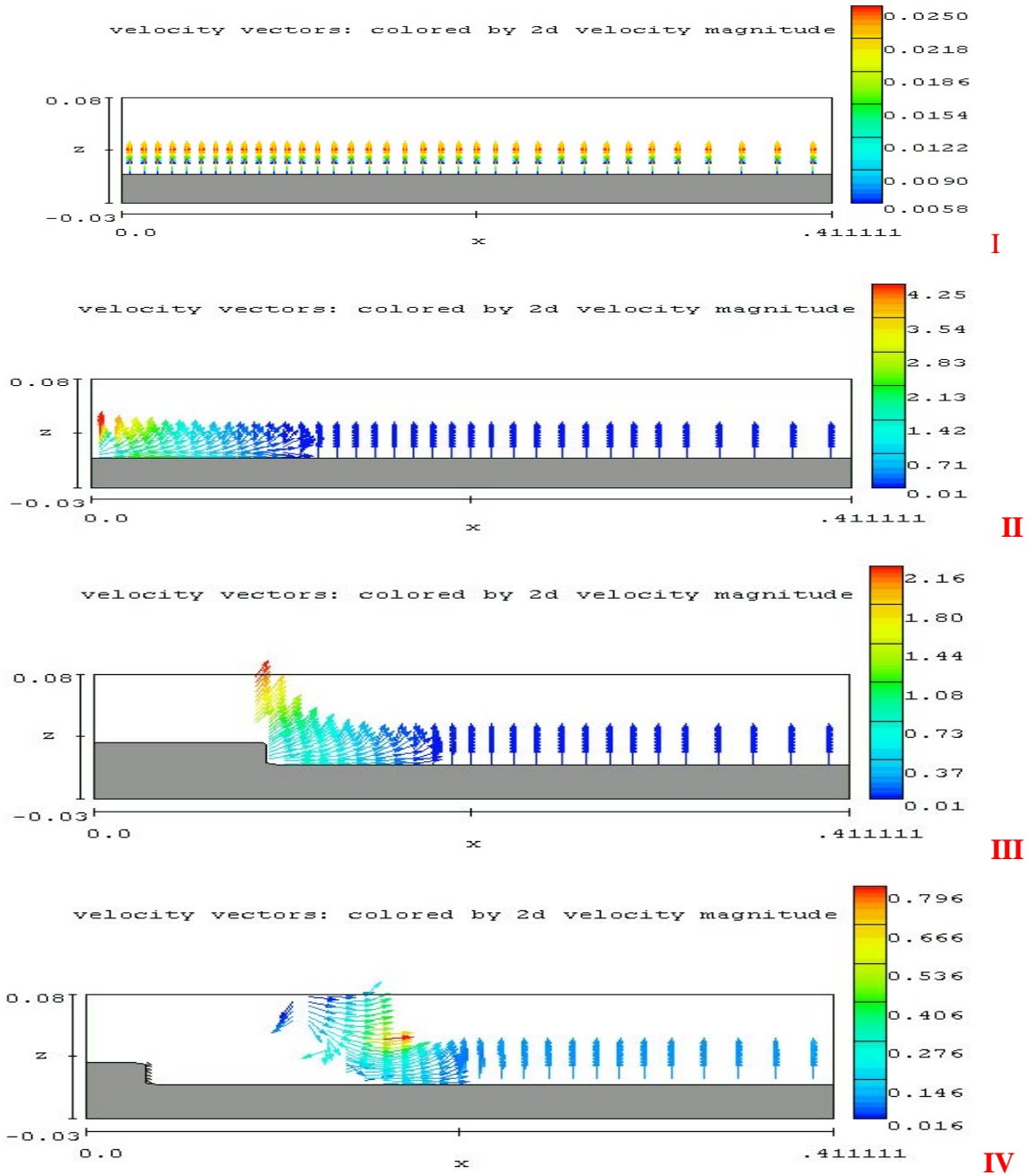


Figure 7.3-13: 2-D Velocity vectors at planes perpendicular to the flow direction as indicated in Figure 7.3.15.

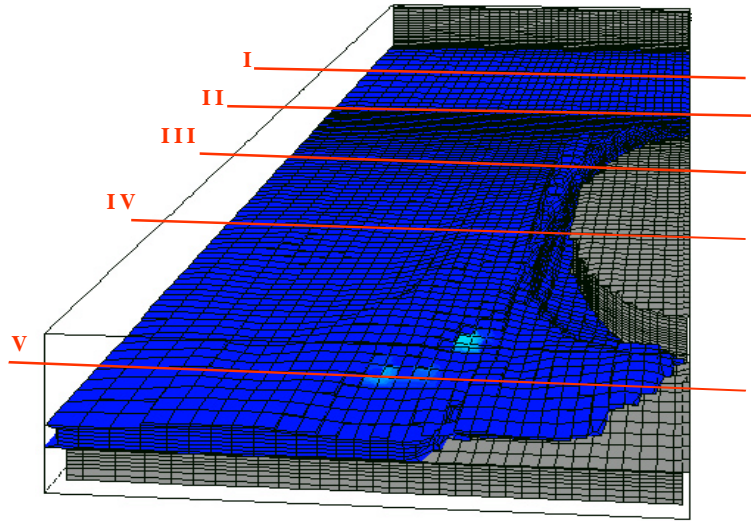
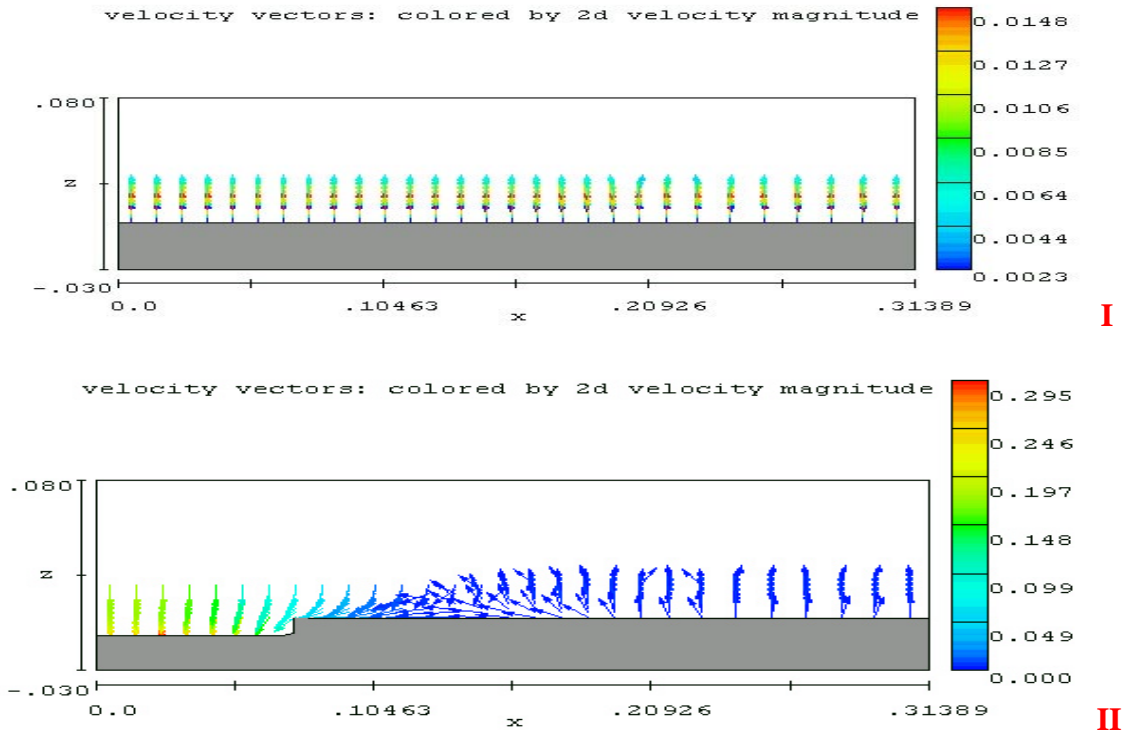


Figure 7.3-14: Perspective view of flow in two-groove systems.



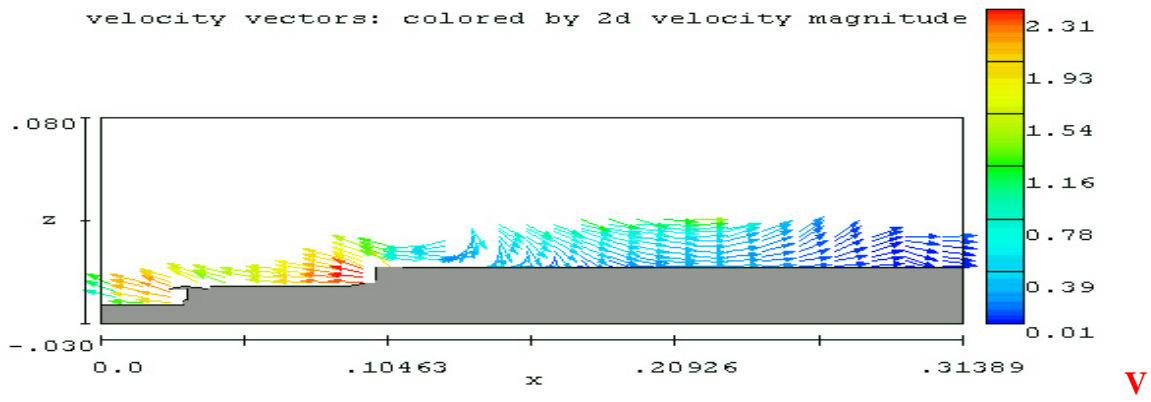
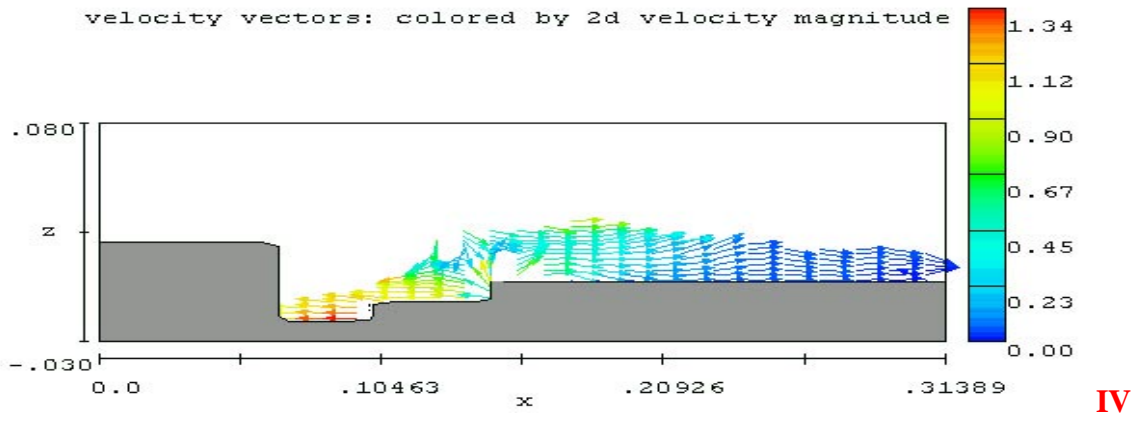
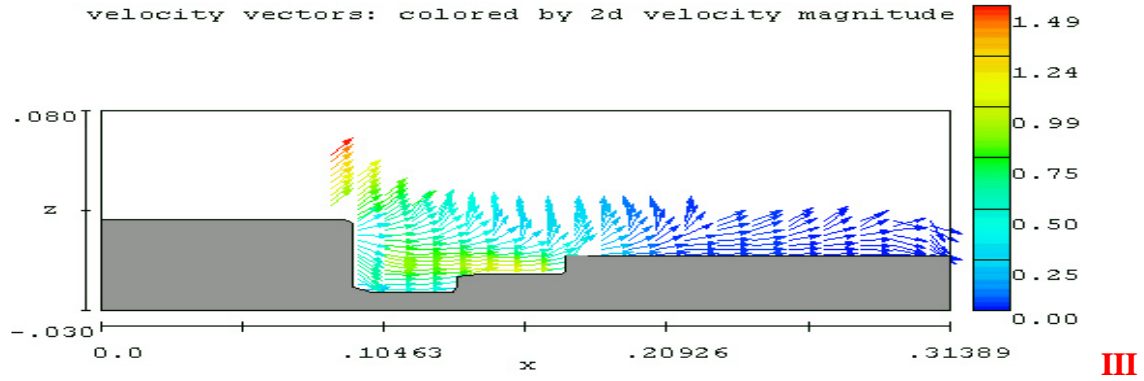


Figure 7.3-15: 2-D Velocity vectors at planes perpendicular to the flow direction as indicated in Figure 7.3.17.

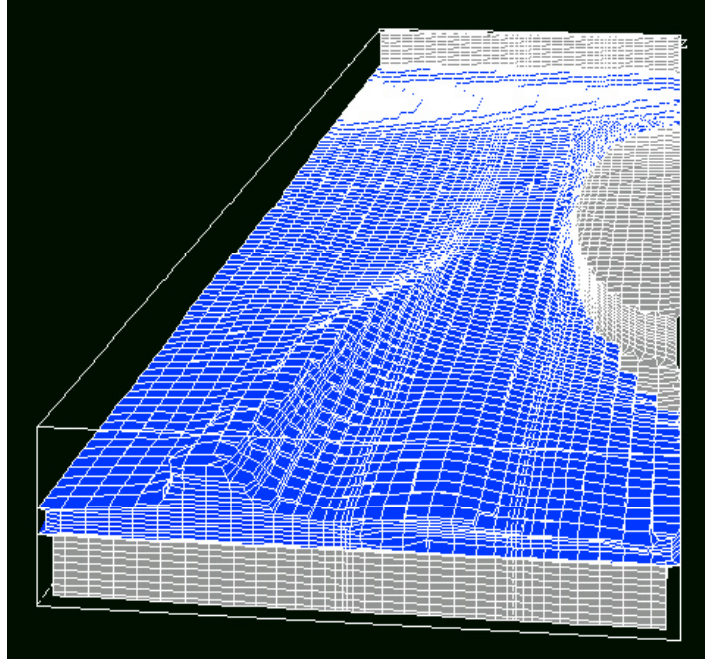
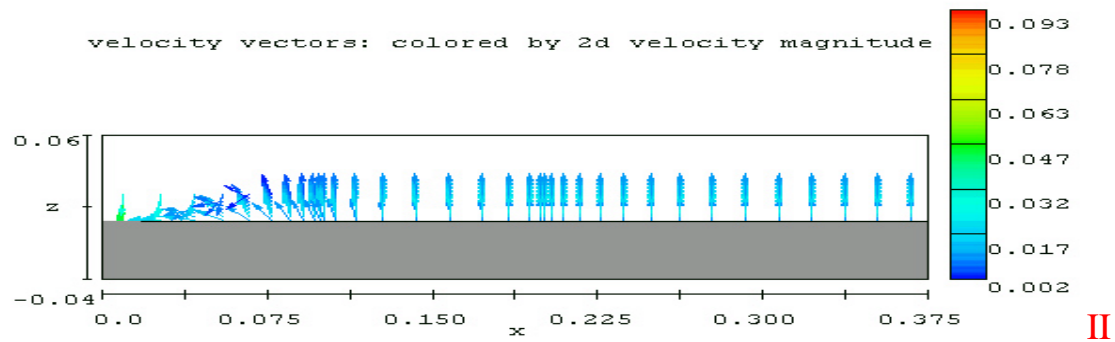
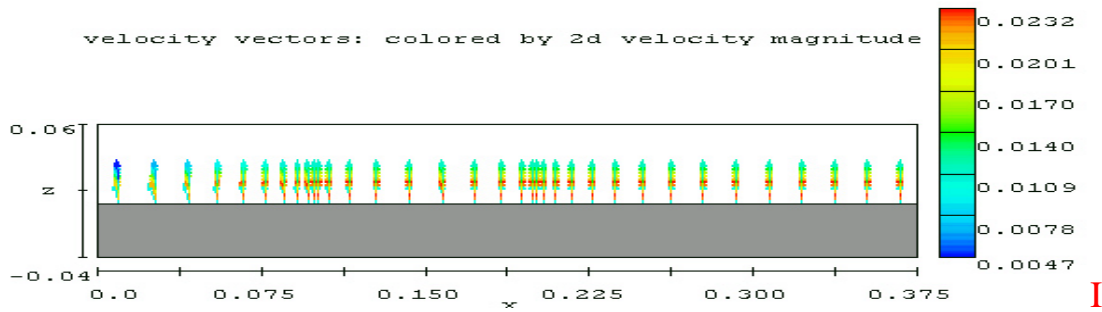


Figure 7.3-16: Perspective view of flow around penetration with the gradually tailored backwall system.



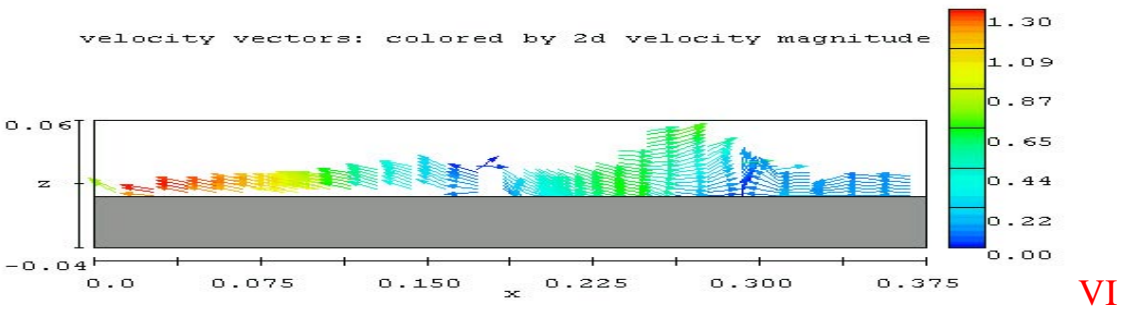
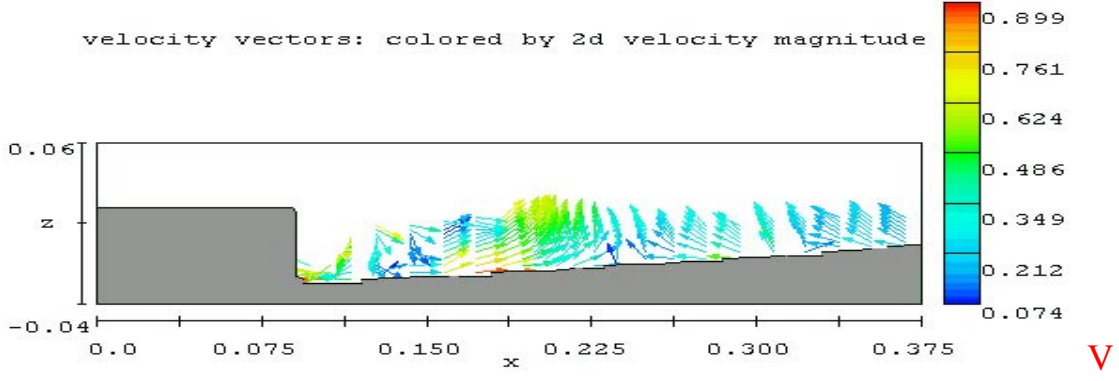
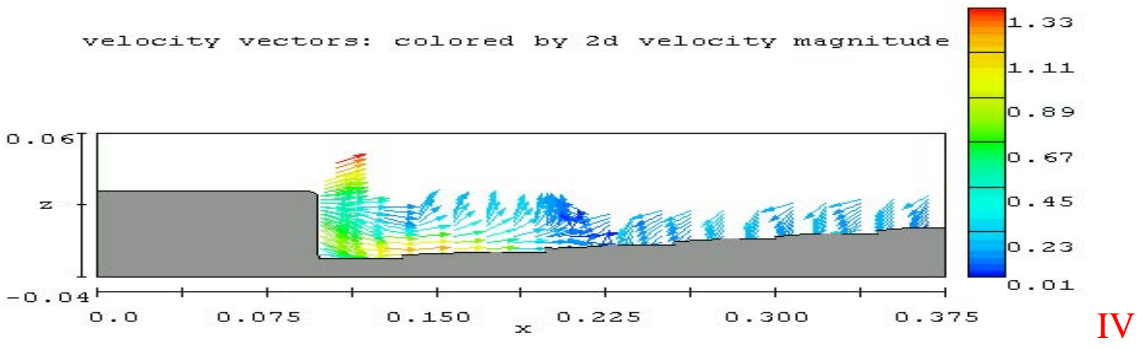
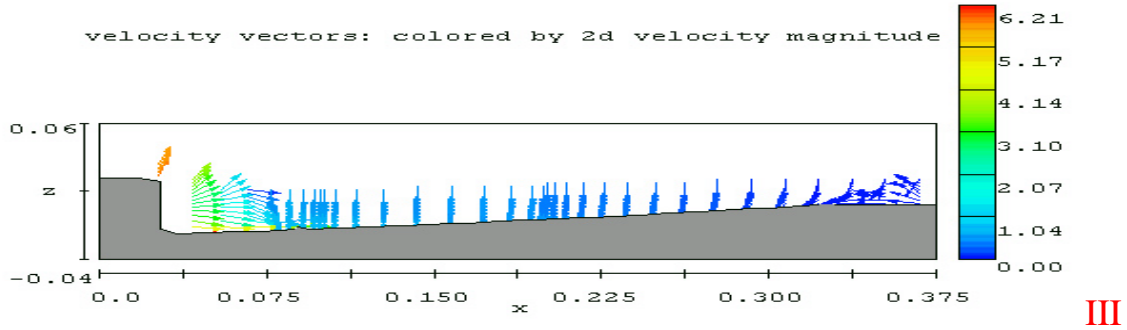
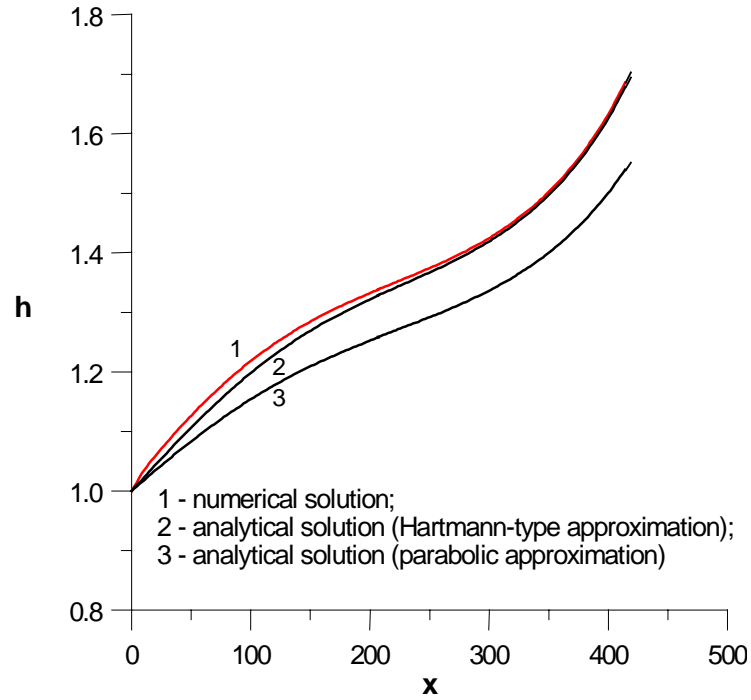


Figure 7.3-17: 2-D Velocity vectors at planes perpendicular to the flow direction and located shown as in Figure 7.3.19.



**Figure 7.3-18: Thickness of the layer vs. distance from the inlet CLiFF parameters:
 $Re=2.35 \cdot 10^5$; $Fr=500$; $Ha=4.53 \cdot 10^5$; $\chi=0.005$; $\beta=0.04$.
side walls are isolated (Lithium)**

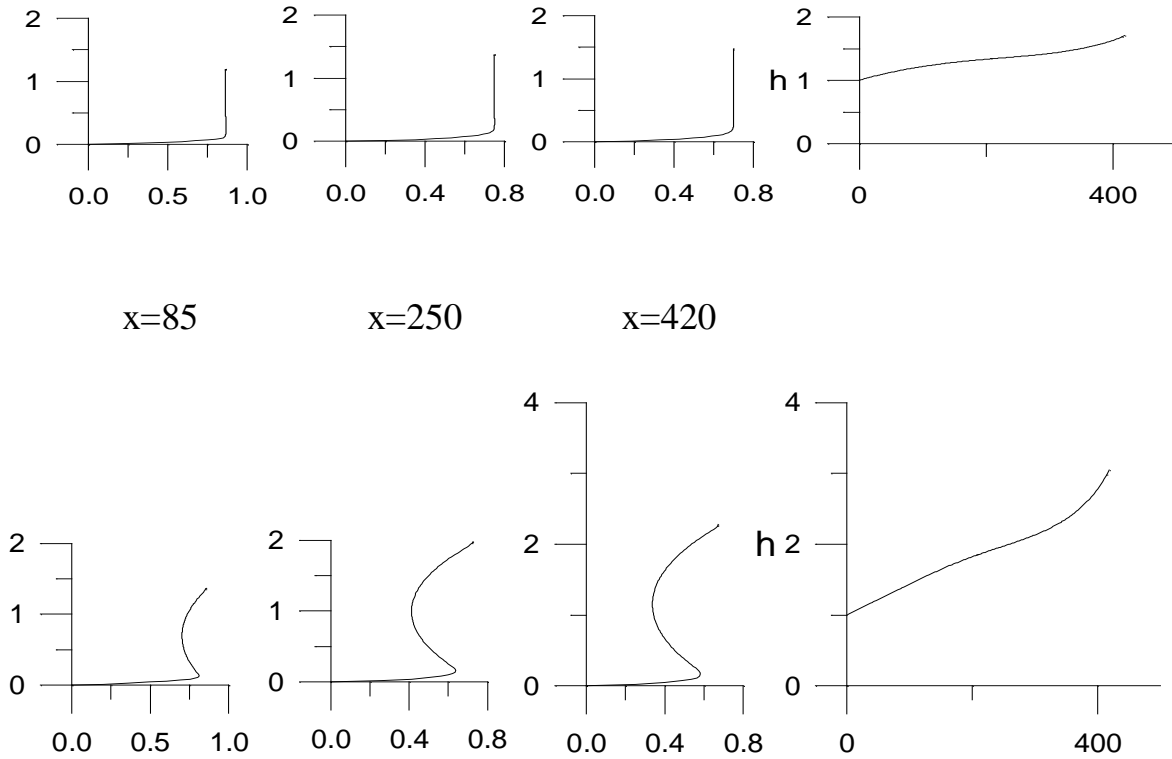


Figure 7.3-19: Velocity profiles in different cross-sections and film thickness evolution: $Re=2.35 \cdot 10^5$; $Fr=500$; $Ha=4.53 \cdot 10^5$; $\chi=0.005$; $\beta=0.04$. Lithium. Upper: Isolated sidewalls. Lower: conducting sidewalls ($c=1.0 \cdot 10^{-6}$)

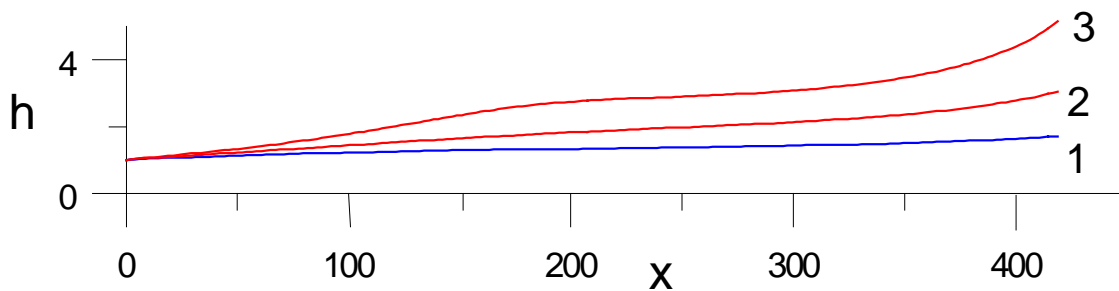


Figure 7.3-20: Influence of the wall conductance ratio on the layer thickness increase ($2b=1$ m). 1- $c_w=0$; 2- $c_w=1.0 \cdot 10^{-6}$; 3- $c_w=2.0 \cdot 10^{-6}$

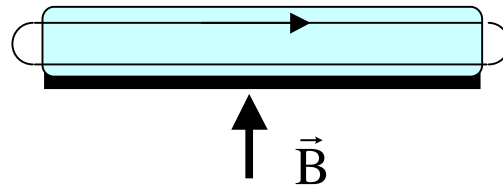


Figure 7.3-21: Cross-sectional area in the model with the radial field component.

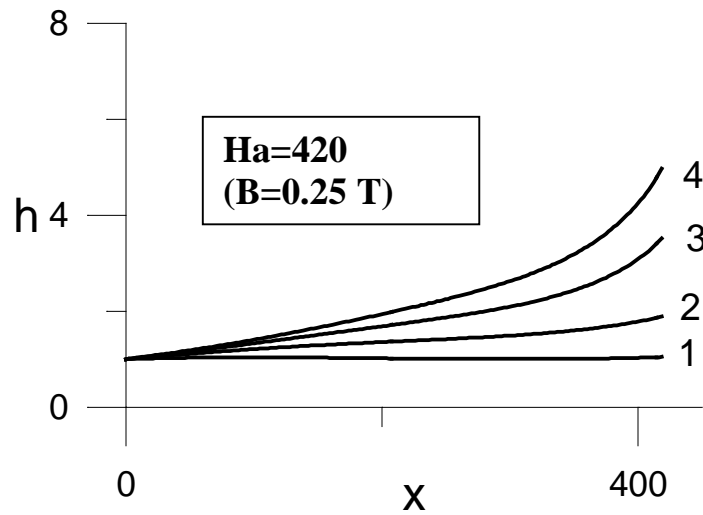


Figure 7.3-22: Influence of the wall conductance ratio on the thickness of the layer:
1- $c_w=0$; 2- $c_w=0.002$; 3- $c_w=0.003$; 4- $c_w=0.0035$

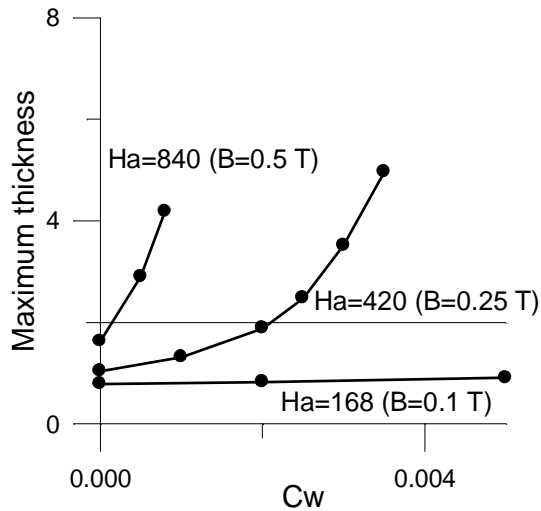


Figure 7.3-23: Influence of the radial magnetic field and the wall conductance ratio on the maximum thickness of the layer

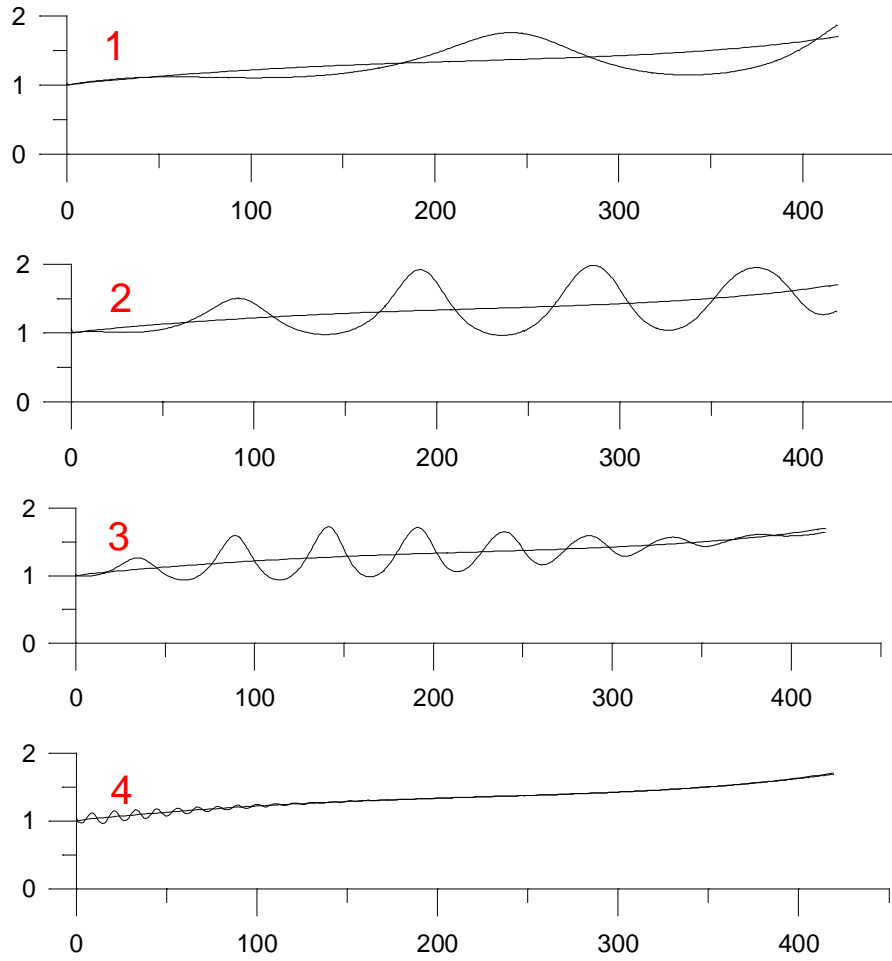


Figure 7.3-24: Surface waves propagation. Initial disturbances are specified as perturbations of the mean velocity without perturbations of the flow rate. 1- $\varepsilon = 5\%$; $\omega = 0.02$ ($\lambda \approx 4.5$ m), 2- $\varepsilon = 5\%$; $\omega = 0.05$ ($\lambda \approx 2.0$ m), 3- $\varepsilon = 5\%$; $\omega = 0.10$ ($\lambda \approx 1.0$ m), 4- $\varepsilon = 5\%$; $\omega = 0.50$ ($\lambda \approx 0.2$ m).

7.4 Nuclear Analysis and Activation

In this Section we calculate the tritium production and heating rate profiles with the combination of Breeder/Structure Li/V, Flibe/Ferritic Steel, and Sn-Li/Ferritic Steel in the calculational model shown in Figure 7.4-1. Also assessed is the impact of Li-6 enrichment on tritium breeding ratio (TBR) and power multiplication factor (PM). To predict the lifetime of the various components, the key damage parameters have been calculated in the solid wall following the thin liquid layer, in the vacuum vessel, and in the casing of the toroidal coil (TF) of the super conducting magnet (SCM) with and without the presence of the liquid layer. The parameters considered are the DPA/FPY, and the helium production rate (appm/FPY). Since the TBR was found to be marginal in the case of Flibe and Li-Sn breeder, the improvement in TBR upon the inclusion of a beryllium multiplier was also studied. The impact of the utilization of various structural materials (TZM, Nb-1Zr, V-4Cr-4Ti) in the presence of a multiplier zone was also assessed. These topics are covered in Section 7.4.2 through Section 7.4.5. The results from the activation analysis are given in Section 7.4.6.

7.4.1 Numerical Model

The 1-D numerical model used in the analysis is shown in Figure 7.4-1. The model includes the geometrical details of the inboard (I/B) and outboard (O/B) sides to account for the geometrical effect on the key neutronics parameters mentioned above. Liquid breeder of 2 cm-thickness is flowing poloidally from the top and covers a solid wall layer of 0.5 cm-thickness. The blanket and shield follow this solid wall. The dimensions shown and material composition volume fractions are those corresponding to the ARIES-RS design. In this design, the blanket thickness (including the solid wall following the liquid layer) is 60 cm-thick on the O/B side and is 40 cm-thick on the I/B side. It consists of 90% liquid breeder and 10% structure. High-temperature (H.T.) shield follows the blanket and consists of 95% structure and 5% liquid (in the ARIES design, the volume fraction is 15% vanadium alloy, 80% Ferritic steel and 5% liquid breeder). Its thickness is 30.5 cm on the O/B side and 28 cm on the I/B side. After a 2 cm-thick gap, the low-temperature shield follows with a thickness of 30.5 cm (O/B) and 28 cm (I/B). It consists of 95% structure and 5% liquid breeder (in ARIES design, the structure of the L.T. shield is Ferritic steel). In the present analysis, the material and configuration of the vacuum vessel (V.V.) and the TF coil are fixed in all the cases considered. The V.V. walls are made of Ferritic steel (2 cm-thick) with an interior zone of 80% 316SSLN and 20% water. The thickness of this interior zone is 26 cm (O/B) and 16 cm (I/B). The TF coil case is made of SS316LN and epoxy is used as the insulator (see Figure 7.4-1 for details). The analysis reported in section 7.4.1 to 7.4.5 is based on transport calculations performed with the 1-D transport code ANISN [1] using a 46n-21g multigroup cross-section library based on FENDL-1 [2] data and generated with the TRANSX-2 interface code [3].

7.4.2 Tritium Breeding

The local tritium breeding ratio (TBR) was calculated as a function of Li-6 enrichment for the combination of breeder/structure material Li/((V-4Cr-4Ti), Flibe/Ferritic Steel (FS), and Li-Sn/FS. In the Li and Flibe cases, it maximizes around 25%Li-6. In the Li-Sn case, the TBR is very low at natural Li-6 enrichment (~0.38) but it keeps rising rapidly with Li-6 enrichment. At 90%Li-6 enrichment, the TBR reaches a value of 1.26 which is larger than TBR with Flibe (1.1) or with Li (1.18) at this enrichment. This is shown in Figure 7.4-2. From this Figure, the maximum local TBR is as follows: Li/V: 1.46 (25%Li-6), Flibe/FS: 1.16 (25%Li-6), and Li-Sn/FS: 1.26 (90%Li-6). Thus, with no neutron multiplier, the TBR in Li-Sn can be larger than the achievable TBR with Flibe. It will be shown in later section that the situation with a multiplier is different.

The profiles of tritium production rate (TPR) are shown Figure 7.4-3(a) and Figure 7.4-3(b) for the I/B and O/B, respectively. The profiles are shown for the cases where the TBR is maximum with Li-6 enrichment. (i.e. 25%Li-6, 25%Li-6, and 90%Li-6 for the Li, Flibe, and Li-Sn breeder, respectively). The values are in unit of triton atoms generated per incident neutron per cm³. As shown, the TPR at locations near the front surface (facing the plasma side) are the largest in the Flibe case. The TPR profiles with this breeder show steepness larger than the profiles with other breeders due to the large neutron attenuation characteristics of Flibe relative to Li and Li-Sn. This is consistent with the attenuation characteristics of the several breeders discussed in Section 5.3.

7.4.3 Heating Rate Profiles and Power Multiplication

The volumetric heating rate profiles in the I/B and O/B resulting from neutrons slowing down in the system are shown in Figure 7.4-4 for an average wall load of 10 MW/m². The values shown are expressed in terms of w/cm³. The maximum heating rates at various locations are given numerically in Table 7.4-1 for the same neutron wall load. From Figure 7.4-4 and Table 7.4-1, the maximum power deposition rate in the 2 cm liquid layer is the largest in the Li-Sn case (~97 w/cc) followed by Flibe (~70 w/cc) and Li (~52 w/cc). The maximum heating rate in the solid wall (0.5 cm-thick) following the liquid layer is the largest in the Flibe case (~72 w/cc) followed by the Li-Sn (~61 w/cc) and Li (~50 w/cc). In the blanket, the maximum heating rate is the largest in the Li-Sn case (~70 w/cc, features similar to the liquid layer) followed by Flibe (~57 w/cc) and Li (~45 w/cc). Generally, the heating rates in the layer/FW/Blanket are larger in the outboard side than in the inboard. However, the heating rates in the H.T shield, the L.T. shield, the V.V. walls, and the interior zone of the V.V. are larger in the inboard side than in the outboard. Note that the heating rates at deep locations (i.e. in the V.V) with the Flibe breeder are an order of magnitude lower than with other breeders. The largest heating rates across the shield and V.V. are in the case of Li breeder since the attenuation power of this breeder is the least compared to the other breeders (i.e. neutrons and gamma rays resulting from their interactions can penetrate to deep locations than with other breeders).

The total power deposited in each component of the system per unit height in the poloidal direction is given in Table 7.4-2 for an average neutron wall load of 10 MW/m². The same features found for the maximum heating rates still hold for the integrated power deposited in the various component; larger power deposited in the liquid layer and blanket with the Li-Sn breeder, larger power deposited in the solid wall that follows the layer with the Flibe breeder, and the power deposited in the remote components (i.e. H.T. and L.T shields, V.V walls, etc) are the largest with the Li breeder, for the reasons described above.

According to Table 7.4-2, the power multiplication factor (PM) in the entire system is the largest with the Li-Sn breeder (1.39) as compared to the other breeders (Li: PM ~1.14, Flibe: PM ~1.02). The variation of the PM with Li-6 enrichment is shown in Figure 7.4-5. The features of the PM curves and the TBR curves when Li-6 increases are reversed, i.e. the PM minimizes with Li-6 enrichment at the values where TBR maximizes. The variation of the PM is less sensitive to Li-6 enrichment in the Li and Flibe cases than in the Li-Sn case where it drops from ~1.48 (natural Li-6) to ~1.28 (90%Li-6).

The large power multiplication in the case of Li-Sn breeder is due to the large gamma heating that is the consequence of the large Sn(n,gamma) reactions (see also discussion in Section 11.6). This is advantageous from the viewpoint of improving the thermal efficiency of the system. The power multiplication with Flibe is only ~1.02 at 25% Li-6 enrichment. Coupled with the marginal local TBR value of 1.16 at this enrichment (where TBR is the maximum), it makes the Flibe to have the most unfavorable neutronics characteristics as far as tritium and power multiplication are concerned. As will be seen in section 7.4.5, the TBR can be drastically improved upon utilizing beryllium as a multiplier.

7.4.4 Damage Parameters

The damage parameters in the solid wall following the liquid layer, in the walls of the V.V. and in the TF coil casing are calculated and expressed in terms of DPA/FPY and helium production rate in appm/FPY. The values are shown in Table 7.4-3 for the three breeders in the presence of the 2 cm-thick layer. The corresponding values in the case of a bare solid walls (no flowing liquid layer) are shown in Table 7.4-4. Several observations can be made: (1) The damage parameters in the solid walls of the O/B are larger than those found in the I/B, (2) the damage parameters in the V.V. walls and in the TF coil casing of the I/B are larger than the O/B ones, (3) damage parameters in the Li breeder case are larger in the V.V. walls and the TF coil casing characteristics of Li compared to Flibe and Li-Sn, and (4) because the superior attenuation characteristics of Flibe relative to the other breeders, the damage parameters in the V.V. walls and the TF coil casing are about an order of magnitude less compared to the values found with the other breeders.

The inclusion of the 2-cm layer reduces the damage parameters in the first solid wall by 11-30%, depending on the response type under consideration. The percent reduction (including heating rate in w/cc) is shown in Table 7.4-5. This is consistent with the

estimated 10-fold thickness (the thickness required to reduce a response by an order of magnitude) discussed in Section 5.3 for several breeders.

The largest DPA rate in the bare solid wall is in the case of Li-Sn breeder on the O/B side (~152 DPA/FPY) followed by Flibe (~141 DPA/FPY) and Li (~137 DPA/FPY). The corresponding values in the presence of the liquid layer are: ~122 DPA/FPY, ~110 DPA/FPY, and 123 DPA/FPY, respectively. For a lifetime limit of ~200 DPA, the solid wall with the liquid layer can last for ~ 1.6 years with the Li and Flibe breeders and slightly longer (~1.8 year) with the Flibe breeder. On the other hand, the accumulated DPA in the V.V walls over 30 years are 3 (considering the largest DPA rate with the Li breeder on the I/B side). This makes the V.V. a lifetime component (less than 200 DPA). Furthermore, the accumulated helium production over 30 years is ~ 0.9 appm, which is less than the limit of 1 appm for reweldability.

7.4.5 Enhancing Tritium Breeding

7.4.5.1 Effect of neutron multiplier on tritium breeding ratio

From Section 7.4-2, it was shown that the maximum local TBR is: Li/V: 1.46 (25%Li-6), Flibe/FS: 1.16 (25%Li-6), and Li-Sn/FS: 1.26 (90%Li-6). Thus, with no neutron multiplier, the TBR in Li-Sn can be larger than the TBR with Flibe. The marginal TBR with Flibe can be improved upon including a beryllium multiplier in the blanket region.

The blanket region in the O/B (60 cm-thick) and in the I/B (40 cm-thick) was assumed to include a front multiplier zone consisting of 60% Be, 30% breeder, and 10% structure. The thickness of this zone was varied. The rest of the blanket zone (back blanket zone) is assumed to remain with the same composition (90% breeder, 10% structure). Figure 7.4-6 shows the variation of TBR with the front multiplier thickness where natural Li-6 enrichment is assumed for the Flibe and Li-Sn. As shown, the TBR increased from 1.14 to 1.63 in Flibe (~43% increase) while the TBR in Li-Sn increased from 0.38 to 0.92 (~142% increase). This demonstrates the effectiveness of beryllium in improving TBR. Also, with a multiplier zone, the TBR with Flibe is always larger than the TBR with Li-Sn breeder. The TBR with Flibe (natural Li-6) in the presence of Be is larger than in the case of Li (TBR ~1.46) with 25% Li-6.

To investigate the impact of Li-6 enrichment on TBR in the presence of a multiplier, the front Be zone was fixed at 10 cm-thickness and Li-6 was varied. Figure 7.4-7 shows the local TBR in this case (Ferritic steel structure). For Flibe, the TBR maximizes at 25% Li-6. It increased from 1.47 (natural Li-6) to 1.50 (only ~2% increase). For Li-Sn, the TBR keeps rising with Li-6 enrichment. It increased from 0.57 (natural li-6) to 1.31 (90%Li-6), i.e. ~134% increase. Also, contrary to the no-multiplier case, the local TBR with Li-Sn breeder is always lower than the local TBR with the Flibe breeder.

To estimate the upper bound of the local TBR (i.e. maximum achievable value), the optimal Li-6 enrichment obtained from Figure 7.4-7 (25%Li-6 in Flibe, 90%Li-6 in Li-

Sn) was used and the beryllium multiplier zone was increased in thickness. The results are shown in Figure 7.4-8. In Flibe, the TBR increased from 1.16 to 1.68 (~45% increase) while the TBR in Li-Sn increased from 1.26 to 1.39 (~10%) upon increasing the Be zone from 0 cm (no-multiplier zone) to fully occupying the blanket zone (60 cm O/B, 40 cm I/B). One notices that the Flibe is superior to Li-Sn when a beryllium multiplier is used. Thus the maximum local TBR is 1.68 and 1.39 for the Flibe and the Li-Sn breeder under the conditions: 25%Li-6 enrichment (Flibe) and 90%Li-6 enrichment (Li-Sn), 0.5 cm solid wall with 2 cm-thick breeder layer, Ferritic steel structure 10% in the blanket, 60%Be, and 30% breeder in the front multiplier zone with a thickness of ~60/40 cm on the OB/IB side. It was shown that increasing the blanket thickness to 90/70 cm has insignificant increase (less than 1%) on the local TBR cited above.

The impact of the percentage of the structure in the blanket on the TBR was also studied. The references cases are:

Liquid layer:	2 cm Breeder
Solid wall:	0.5 cm Ferritic Steel
Beryllium Zone:	10 cm (Flibe), 20 cm (Sn-Li) (60%Be, 30%breeder, 10%FS)
Back Blanket Zone:	50/30 cm OB/IB (Flibe Case: 90%Flibe, 10%FS) 40/20 cm OB/IB (Li-Sn Case: 90%Li-Sn, 10%FS)

7.4.5.2 Effect of the type of structure on tritium breeding ratio

The reference cases studied above utilized either V-4Cr-4Ti alloy with Li or Ferritic steel with the Flibe and Li-Sn breeders. The impact of considering other structural materials on TBR was investigated by replacing the structural material with either W, V-4Cr-4Ti, TZM, Nb-1Zr, and FS alloy, on one-to-one basis, in the reference Flibe and Li-Sn breeder system.

The reference case for Flibe (TBR=1.504) is:

Liquid layer:	2 cm Flibe
Solid wall:	0.5 cm Structure
Beryllium Zone:	10 cm (Flibe) (60%Be, 30%Flibe, 10%Structure)
Back Blanket Zone:	50/30 cm OB/IB (90%Flibe, 10%Structure)

Table 7.4-6 shows the achievable TBR in the case where a beryllium multiplier zone (10 cm-thick) is included and in the case where this zone is replaced entirely with the non-multiplier back blanket zone. While there is an improvement in the TBR (of 9-29% increase) upon the inclusion of the beryllium zone when the structure used is V-4Cr-4Ti, TZM, Nb-1Zr, or FS, there is an adverse effect on the local TBR when tungsten is used in the presence of beryllium. This latter combination leads to ~ 12% reduction in the local TBR. The neutron multiplication with W through the (n,2n) reactions, whose threshold energy is high (6.6 MeV), tends to compete with the Be(n,2n) reactions, whose threshold energy is relatively low (~ 2 MeV). Successive neutron multiplication takes place in Be

which further moderates neutron to low energies where the Li-6 (n,α) cross section is high. The presence of the W reduces this effect which in turn reduces the local TBR. The strong moderation of neutron energy in Flibe tends to improve the TBR.

As for the Li-Sn breeder, the reference case is:

Liquid layer:	2 cm Sn-Li
Solid wall:	0.5 cm Structure
Beryllium Zone:	20 cm (Sn-Li) (60% Be, 30% Sn-Li, 10% Structure)
Back Blanket Zone:	40/20 cm OB/IB (Sn-Li) (90% Sn-Li, 10% Structure)

Table 7.4-7 is similar to Table 7.4-6 and it gives the achievable TBR with and without the beryllium multiplier zone (20 cm-thick). As shown, there is only an improvement in the TBR (of ~8% increase) upon the inclusion of the beryllium zone when the structure used V-4Cr-4Ti or FS. The presence of beryllium in this case has an adverse effect on the local TBR when tungsten, TZM, or Nb-1Zr alloys are used as the structural materials. The decrease in the local TBR upon the inclusion of the beryllium zone is ~10% in the TZM and Nb-1Zr case, but as large as ~30% in the case of tungsten. Note that neutron multiplication through ($n,2n$) reactions takes also place in Mo, and Nb at high threshold energies, but to lesser extent than multiplication in W. Since Li-Sn is not as a good moderator to neutrons as Flibe, the impact of the competition between neutron multiplication in beryllium and in W, Mo, or Nb are more pronounced. Since much less ($n,2n$) reactions take place in V and Ferritic steel alloys, the utilization of beryllium with these structural materials improves the local TBR by ~8%.

The adverse effect of the presence of a beryllium multiplier zone when tungsten is used as the structural material is further investigated in Li-Sn breeder reference case (see above) by gradually increasing the volume fraction of Be in the beryllium multiplier zone up to 60%. The variation of local TBR with this increase is shown in Figure 7.4-10. As shown, the TBR drops from a value of 1.244 (0% Be) to 0.872 (60% Be). When the Be fraction is low, the TBR decreases by ~3-4% for every 10% increase in Be fraction. This decrease is larger (~6-10%) at larger Be fraction.

7.4.6 Activation Analysis

Activation analysis was performed for the CLiFF concept. Calculations are performed assuming neutron wall loadings of 7 and 10 MW/m² at the inboard and outboard first walls, respectively. The analysis used the ORNL low activation ferritic steel (LAFS) 9Cr-2WVTa as a structure material and Flibe as breeding material. No other material combinations have yet been analyzed. The elemental composition of the ferritic steel 9Cr-2WVTa alloy is shown in Table 7.4-8. The radial build used in the analysis is based on the ARIES-RS design and uses a 2-cm thick liquid first wall (see Fig. 7.4-1). Based on dpa limits for steel, the inboard and outboard blankets were assumed to be replaced every 3 FPY. On the other hand, the shield and vacuum vessel were assumed to stay in place for 30 FPY. Neutron transport calculations were performed using the discrete ordinates neutron transport code DANTSYS [4]. The neutron flux obtained from

the neutron transport calculations was used in the activation calculations. The activation analysis was performed using the activation code DKR-PULSAR2.0 [5]. The code combined the neutron flux with the FENDL/A-2.0 [6] data library to calculate the activity and decay heat as a function of time following shutdown. Calculated specific activities were used to calculate the waste disposal ratings (WDR) of the different components at the end of their life-time. Results of the decay heat analysis were used to evaluate the temperature variation exhibited by the structure during a loss of coolant accident (LOCA).

7.4.6.1 Activity and decay heat

Figure 7.4-11 and Figure 7.4-12 show the specific activity and decay heat values induced in the different components of CLiFF as a function of time following shutdown, respectively. As shown in the two figures, the ORNL LAFS produces acceptable level of radioactivity after shutdown. The blanket and shield dominate the overall activity and decay heat induced in the structure. Table 7.4-9 shows a list of nuclides that dominate the induced radioactivity at different times following shutdown. As shown in the table, ^{55}Fe ($T_{1/2} = 2.7$ yr), ^{185}W ($T_{1/2} = 75.1$ day), and ^{187}W ($T_{1/2} = 23.9$ hr) are the main contributors to the induced radioactivity during the first few weeks following shutdown. ^{55}Fe ($T_{1/2} = 2.7$ yr) and ^{54}Mn dominate the induced activity in the intermediate-term following shutdown. The long-term radioactivity (between one and ten years) is mostly generated by the ^{63}Ni ($T_{1/2} = 100$ yr) and ^{60}Co ($T_{1/2} = 5.27$ yr) isotopes. Nuclides with much longer half-lives have no impact on the decay heat generated from the LOCA point of view. However, as shown in the next section, these nuclides dominate the waste disposal ratings.

7.4.6.2 Waste disposal ratings

The radwaste of the different components of CLiFF were evaluated according to both the NRC 10CFR61 [7] and Fetter [8] waste disposal concentration limits (WDL). The 10CFR61 regulations assume that the waste disposal site will be under administrative control for 100 years. The dose at the site to an inadvertent intruder after the 100 years is limited to less than 500 mrem/year. The waste disposal rating (WDR) is defined as the sum of the ratio of the concentration of a particular isotope to the maximum allowed concentration of that isotope taken over all isotopes and for a particular class. If the calculated $\text{WDR} \leq 1$ when Class A limits are used, the radwaste should qualify for Class A segregated waste. The major hazard of this class of waste is to individuals who are responsible for handling it. Such waste is not considered to be a hazard following the loss of institutional control of the disposal site. If the WDR is > 1 when Class A WDL are used but ≤ 1 when Class C limits are used, the waste is termed Class C intruder waste. It must be packaged and buried such that it will not pose a hazard to an inadvertent intruder after the 100 years institutional period is over. Class C waste is assumed to be stable for 500 years. Using Class C limits, a $\text{WDR} > 1$ implies that the radwaste does not qualify for shallow land burial.

Fetter developed a modified version of the NRC's intruder model to calculate waste disposal limits for a wider range of long-lived radionuclides which are of interest for fusion researchers than the few that currently exist in the current 10CFR61 regulations. Fetter's model included more accurate transfer coefficients and dose conversion factors. However, while the NRC model limits the whole body dose to 500 mrem or the dose to any single organ (one of seven body organs) to 1.5 rem, Fetter limits are based on the maximum dose to the whole body only.

Specific activities calculated by the DKR-PULSAR2.0 code were used to calculate the waste disposal ratings (WDR). The waste disposal ratings for the Fetter and 10CFR61 limits are shown in Tables 7.4-10 and 7.4-11, respectively. Results in the tables are given for compacted wastes. Compacted waste corresponds to crushing the solid waste before disposal (to eliminate voids in the structure) and thus disallowing artificial dilution of activity. The Class C WDR's were calculated after a one-year cooling period. The dominant nuclides are given between brackets. As shown in Table 7.4-10, according to Fetter limits, all components (except for the shield) would qualify for disposal as Class C waste. The inboard and outboard shields are within 30% and 10% of the acceptable limits for disposal as Class C LLW, respectively. The two isotopes, ^{192m}Ir ($T_{1/2} = 240$ yr), and ^{94}Nb ($T_{1/2} = 20,000$ yr) are the dominant source of WDR for all components. ^{192m}Ir and ^{94}Nb are produced by nuclear interactions with the iridium, niobium and molybdenum impurities present in the ORNL LAFS alloy. Finally, as shown in Table 7.4-11, according to the 10CFR61 limits, all components (including the shield) would qualify for disposal as Class C waste. The waste disposal ratings of all components are dominated by contribution from the ^{94}Nb isotope.

References for Section 7.4

1. W. W. Engle, ANISN: A one dimensional discrete ordinates transport code with anisotropic scattering, Report K-1693, Union Carbide Corporation, 1967
2. A.B. Pashchenko, "Completion of FENDL-1 and Start of FENDL-2," INDC(NDS)-352, IAEA Nuclear Data Section, International Atomic Energy Agency, March 1996.
3. R.E. MacFarlane, "TRANSX-2: A Code for Interfacing MATXS Cross-Section Libraries to Nuclear Transport Codes," LA-12312-MS, UC-705 and UC-700 Issued: July 1992, Los Alamos National laboratory, (1992)
4. R. O'Dell et al., "User's Manual for ONEDANT: A Code Package for One-Dimensional, Diffusion-Accelerated, Neutral Particle Transport," Los Alamos National Laboratory report, LA-9184-M (1982).
5. J. Sisolak, Q. Wang, H. Khater and D. Henderson, "DKR-PULSAR2.0: A Radioactivity Calculation Code that Includes Pulsed/Intermittent Operation," to be published.
6. A. Pashchenko et al., "FENDL/A-2.0: Neutron Activation Cross-Section Data Library for Fusion Applications," Report INDC (NDS)-173, IAEA Nuclear Data Section, March 1997.
7. Nuclear Regulatory Commission, 10CFR part 61, "Licensing Requirements for Land Disposal of Radioactive Waste," Federal Register, FR 47, 57446 (1982).

8. S. Fetter, E. Cheng and F. Mann, "Long Term Radioactive Waste from Fusion Reactors," Fusion Engineering and Design, 13, 239-246 (1990).

**Table 7.4-1: Maximum Heating Rate (w/cc) in Various Components
(CLiFF Concept- 10 MW/m²)**

Component	Li/V (25%Li6)	Flibe/FS (25%Li6)	Sn-Li/FS (90%Li6)
Liquid Layer I/B	44.834	59.881	83.219
Liquid Layer O/B	52.204	70.628	97.344
Solid Wall I/B	39.613	56.196	48.519
Solid Wall O/B	50.054	71.550	61.416
blanket I/B	36.235	46.676	62.337
blanket O/B	45.448	57.424	69.707
HT shield I/B	11.270	2.7330	3.2243
HT shield O/B	6.7865	0.70014	1.1116
LT shield I/B	1.3389	0.24382	1.0042
LT shield O/B	0.60495	0.041149	0.29418
VV walls I/B	0.28866	0.044834	0.25488
VV walls O/B	0.098266	0.0055581	0.052204
VV I/B	0.33779	0.046062	0.27637
VV O/B	0.11055	0.0058038	0.057731

**Table 7.4-2: Total Heat Deposited (w/1 cm) in Various Components per Unit Height
(CLiFF Concept- 10 MW/m²)**

Component	Li/V (25%Li6)	Flibe/F.S (25%Li6)	Sn-Li/F.S. (90%Li6)
Liquid Layer I/B	2.2566e+05	3.1639e+05	4.1214e+05
Liquid Layer O/B	4.6013e+05	6.3111e+05	8.1904e+05
Solid Wall I/B	51305	77903	62909
Solid Wall O/B	1.0876e+05	1.6626e+05	1.3362e+05
blanket I/B	1.7823e+6	1.7314e+6	2.1805e+6
blanket O/B	4.5911e+6	3.9939e+6	5.0380e+6
HT shield I/B	2.8160e+05	66825	1.2372e+05
HT shield O/B	3.4893e+05	33343	94721
LT shield I/B	35785	6929.5	30485
LT shield O/B	38534	6929.5	20831
VV walls I/B	1229.18	198.49	1062.02
VV walls O/B	978.713	59.69	519.34
VV I/B	6686.0	961.89	5559.4
VV O/B	6382.7	332.36	3158.3
total	7.9393e+06	7.0326e+06	8.9262e+06
Power Multiplication	1.14	1.02	1.39

**Table 7.4-3: Damage Parameters in the CLiFF Concept
with 2 cm Liquid Layer (10 MW/m²)**

Component	Li/V (25%Li-6)		Flibe/FS (25%Li-6)		Sn-Li/FS (90%Li-6)	
	DPA/FPY	He ppm/FPY	DPA/FPY	He ppm/FPY	DPA/FPY	He ppm/FPY
SW I/B	96.115	335.14	82.583	923.84	96.709	821.71
SW O/B	122.69	454.20	109.75	1301.0	122.24	1150.8
V.V. I/B	0.11138	0.025427	0.012007	0.0029806	0.080410	0.0033055
V.V. O/B	0.034772	0.0057210	0.0013528	0.00024155	0.014887	0.00030230
TF Coil I/B	0.0019342	0.0017890	0.00020374	0.00020696	0.00090732	0.00023853
TF Coil O/B	7.0087e-05	6.4193e-05	2.7383e-06	2.6835e-06	1.4506e-05	3.5604e-06

SW = Solid Wall

Table 7.4-4: Damage Parameters in the CLiFF Concept with Bare Wall (10 MW/m²)

Component	Li/V (25%Li-6)		Flibe/FS (25%Li-6)		Sn-Li/FS (90%Li-6)	
	DPA/FPY	He ppm/FPY	DPA/FPY	He ppm/FPY	DPA/FPY	He ppm/FPY
Solid Wall I/B	111.95	420.39	113.55	1399.9	124.96	1279.8
SW O/B	137.95	542.39	141.26	1808.1	151.58	1652.7
V.V. I/B	0.11844	0.027404	0.011464	0.0030230	0.088559	0.0038988
V.V. O/B	0.037162	0.0061448	0.0015919	0.00028676	0.016788	0.00035880
TF Coil I/B	0.0025566	0.0019118	0.00023851	0.00024555	0.00097252	0.00028062
TF Coil O/B	9.3092e-05	6.9104e-05	3.2272e-06	3.1746e-06	1.6462e-05	4.2269e-06

Table 7.4-5: Percent Reduction in FW parameters

	Li/V (25%Li-6)	Flibe/FS (25%Li-6)	Li-Sn/FS (90% Li-6)
DPA/FPY	~11%	~23%	~19%
Helium and Hydrogen Production (appm/FPY)	~15%	~28%	~30%
Heating rate (w/cc)	~12%	~18%	~25%

**Table 7.4-6: The Local Achievable TBR with and without a Beryllium Multiplier
Zone with Various Structural I Materials- Flibe Breeder**

Structure Type	With Be-Zone	Without Be-Zone	Change in TBR
W	0.887	0.954	-12%
V-4Cr-4Ti	1.535	1.189	29%
TZM	1.184	1.065	8.7%
Nb-1Zr	1.131	0.928	16%
Ferritic Steel	1.504	1.165	29%

**Table 7.4-7: The Local Achievable TBR with and without a Beryllium Multiplier
Zone with Various Structural I Materials- Li-Sn Breeder**

Structure Type	With Be-Zone	Without Be-Zone	Change in TBR
W	0.872	1.244	-30%
V-4Cr-4Ti	1.379	1.275	8.2%
TZM	1.122	1.254	-11%
Nb-1Zr	1.069	1.185	-10%
Ferritic Steel	1.356	1.259	8%

Table 7.4-8: Elemental Composition of the ORNL LAFS Alloy.

Nuclide	wt% or wppm
C	0.1%
Si	0.25%
V	0.025%
Cr	9%
Mn	0.5%
Fe	88.055%
Co	34 wppm
Ni	402 wppm
Nb	0.5 wppm
Mo	70 wppm
Pd	0.18 wppm
Ag	0.16 wppm
Cd	0.05 wppm
Eu	0.05 wppm
Dy	0.05 wppm
Ho	0.05 wppm
Er	0.05 wppm
Ta	0.07%
W	2%
Os	0.02 wppm
Ir	0.05 wppm
Bi	0.05 wppm

Table 7.4-9: List of Dominant Nuclides.

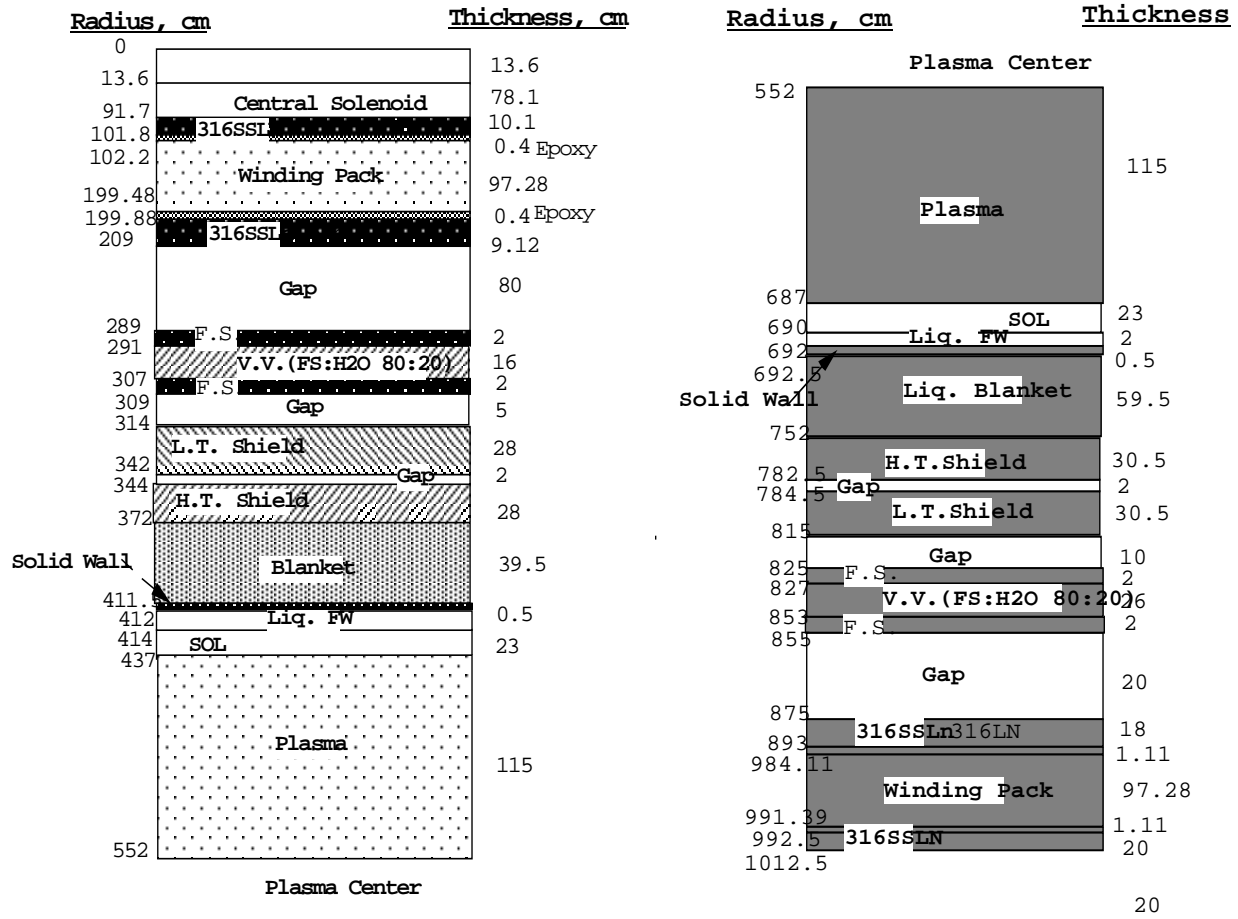
	Activity	Decay Heat
Short-term < 1 day	⁵⁵ Fe, ¹⁸⁵ W, ¹⁸⁷ W	⁵⁶ Mn, ¹⁸⁷ W
Intermediate-term < 1 month	⁵⁵ Fe, ⁵⁴ Mn, ⁵¹ Cr	⁵⁴ Mn, ¹⁸² Ta
Long-term > 1 year	⁵⁵ Fe, ⁶³ Ni	⁶⁰ Co, ⁵⁴ Mn

Table 7.4-10. Class C Waste Disposal Ratings Using Fetter Limits.

Zone	FPY	WDR	Dominant Nuclides
<i>Inboard Blanket</i>	3	0.687	^{192m} Ir, ⁹⁴ Nb
<i>Inboard Shield</i>	30	1.31	^{192m} Ir, ⁹⁴ Nb
<i>Inboard VV</i>	30	0.835	^{192m} Ir, ⁹⁴ Nb
Outboard Blanket	3	0.57	^{192m} Ir, ⁹⁴ Nb
<i>Outboard Shield</i>	30	1.09	^{192m} Ir, ⁹⁴ Nb
<i>Outboard VV</i>	30	0.267	^{192m} Ir, ⁹⁴ Nb

Table 7.4-11: Class C Waste Disposal Ratings Using 10CFR61 Limits.

Zone	FPY	WDR	Dominant Nuclides
<i>Inboard Blanket</i>	3	0.282	⁹⁴ Nb
<i>Inboard Shield</i>	30	0.567	⁹⁴ Nb
<i>Inboard VV</i>	30	0.129	⁹⁴ Nb
Outboard Blanket	3	0.231	⁹⁴ Nb
<i>Outboard Shield</i>	30	0.395	⁹⁴ Nb
<i>Outboard VV</i>	30	0.025	⁹⁴ Nb



a) b)

Figure 7.4-1: The Radial Build of the Cliff Concept Based on the ARIES-RS Reactor.
a) Inboard Side, b) Outboard Side.

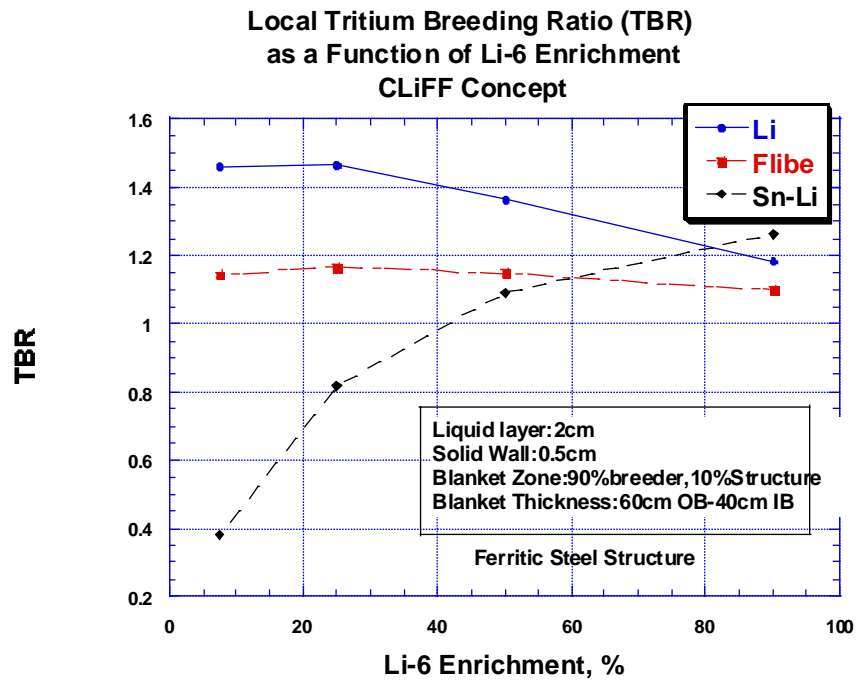


Figure 7.4-2: The Tritium Breeding Ratio (TBR) for Several Breeders as a Function of Li-6 Enrichment.

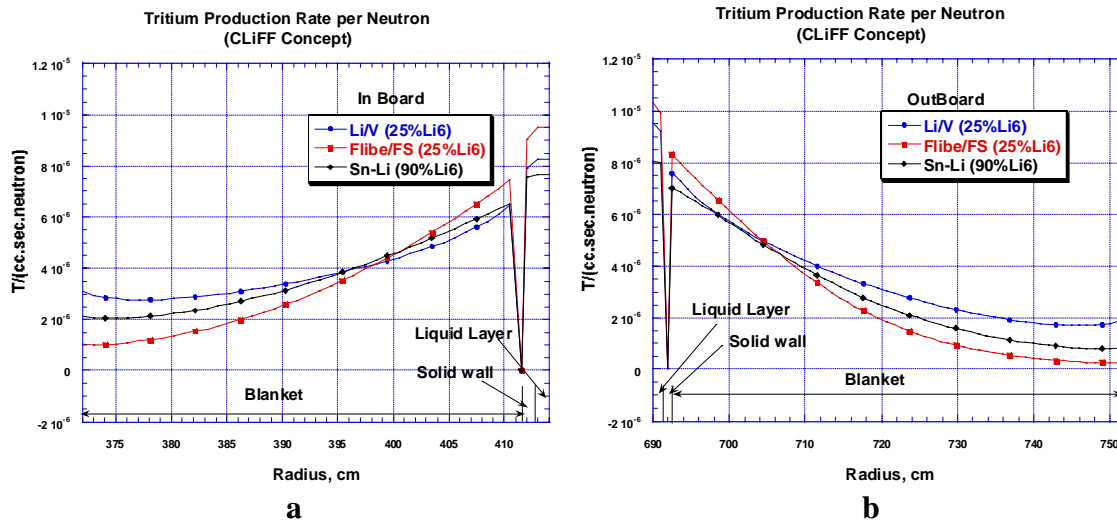


Figure 7.4-3: The Tritium Production Rate (TPR) Profiles for Several Breeders
a) Inboard, b) Outboard.

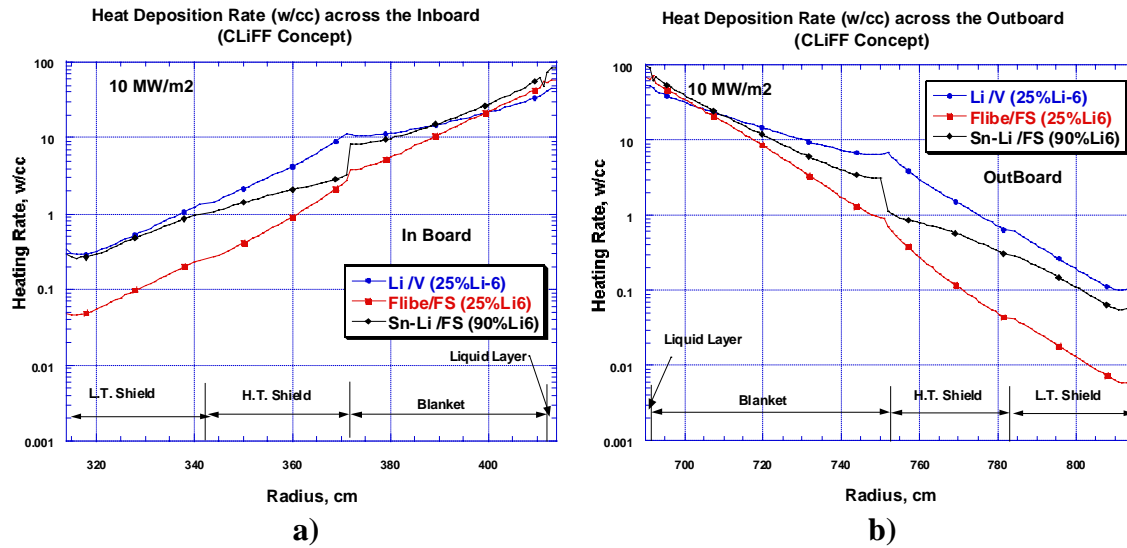


Figure 7.4-4: The Heating rate Profiles for Several Breeders in the CLiFF Concept
a) Across the Inboard, b) Across the Outboard.

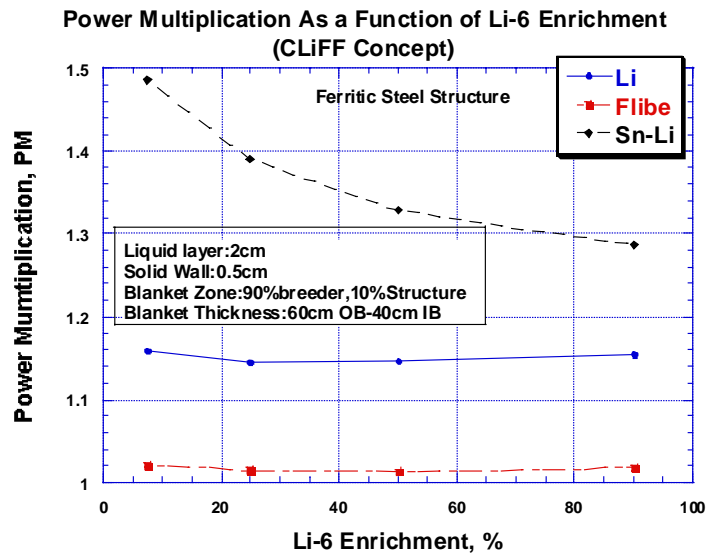


Figure 7.4-5: The Power Multiplication, PM, as a Function of Li-6 Enrichment for Various Breeders

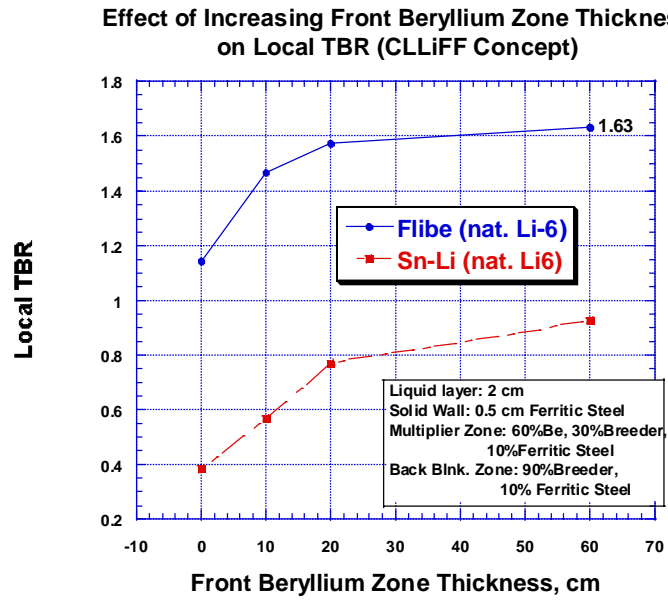


Figure 7.4-6: Effect of Increasing the Thickness of the Front Multiplier Zone on TBR.

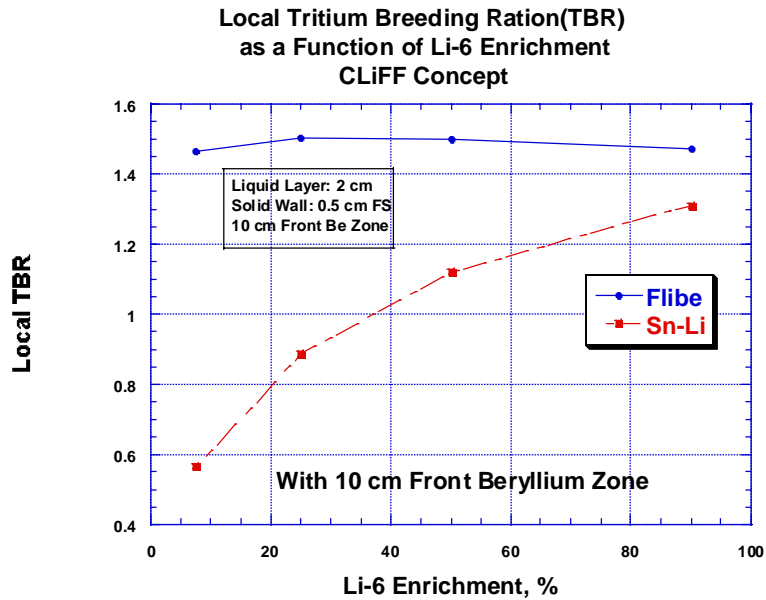


Figure 7.4-7: The Local TBR as a Function of Li-6 Enrichment with a 10 cm-Thick Multiplier Zone.

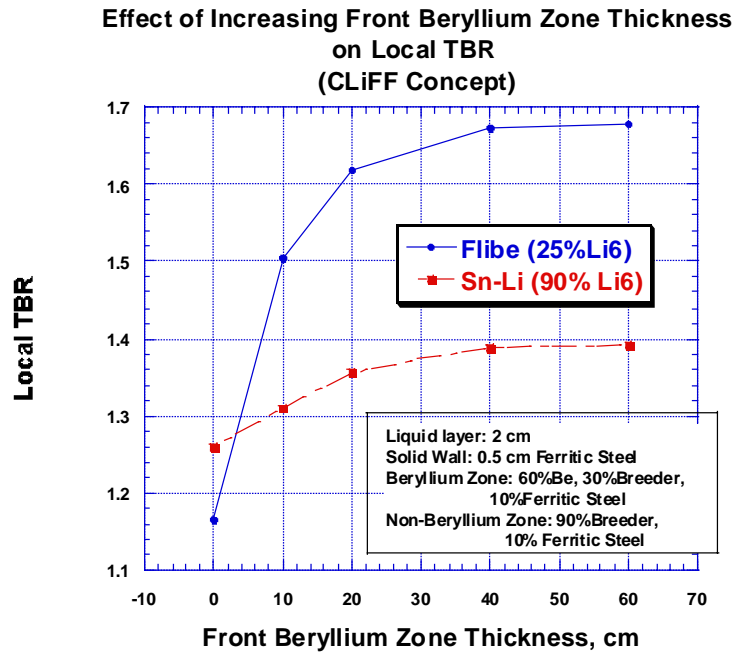


Figure 7.4-8: The variation of The Local TBR with the Front Multiplier Zone with Optimal Li-6 Enrichment

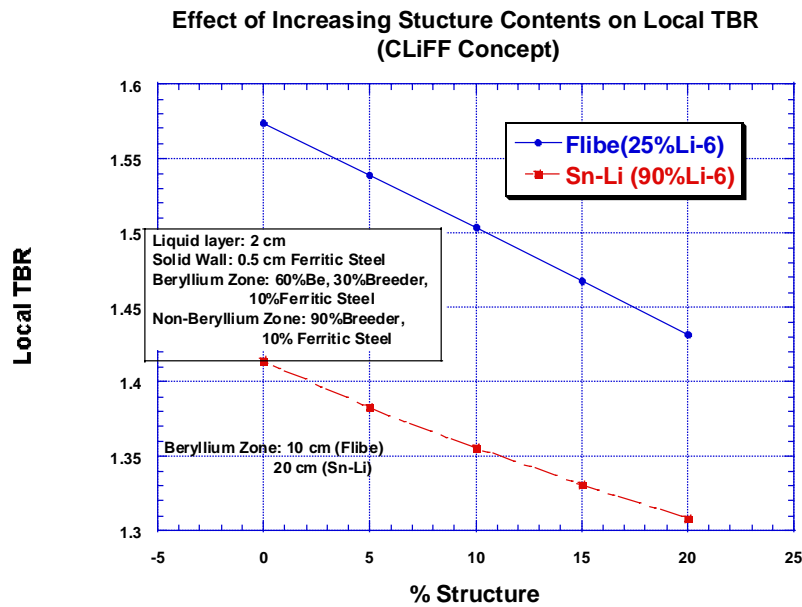


Figure 7.4.9: The Variation of the Local TBR with the Structure Content.

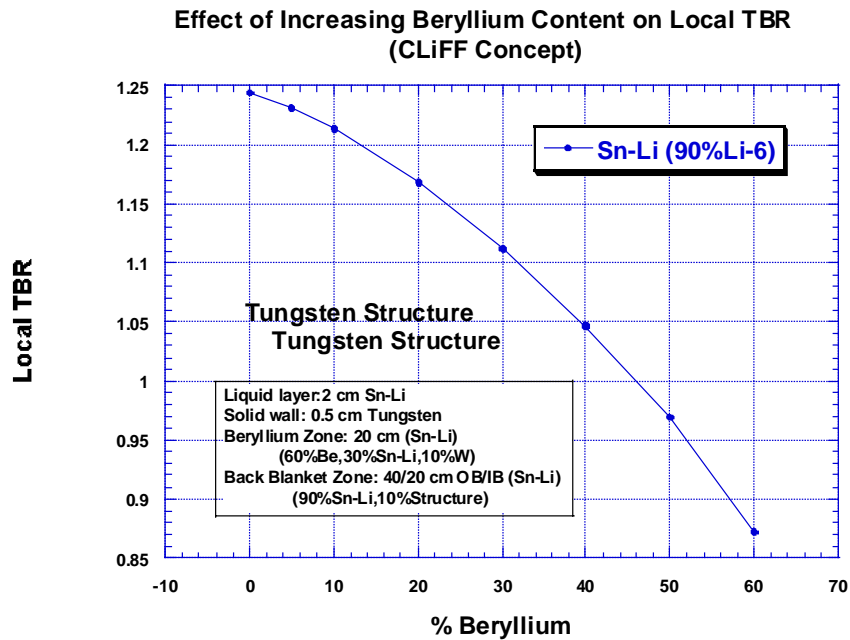


Figure 7.4-10: The Effect of Increasing the Beryllium Volume Fraction on Local TBR in the Presence of Tungsten Structure- Li-Sn Breeder.

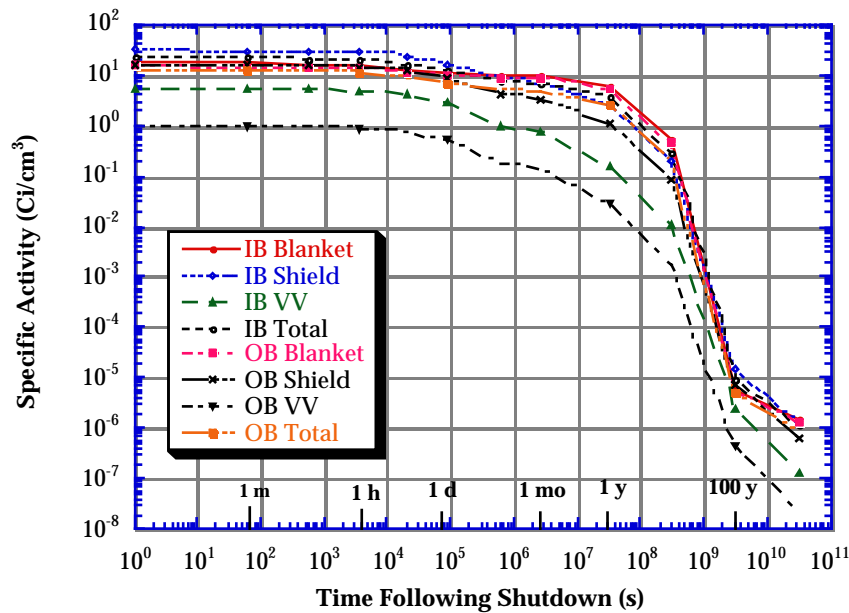


Figure 7.4-11: Activity induced in the different components of CLiFF as a function of time following shutdown.

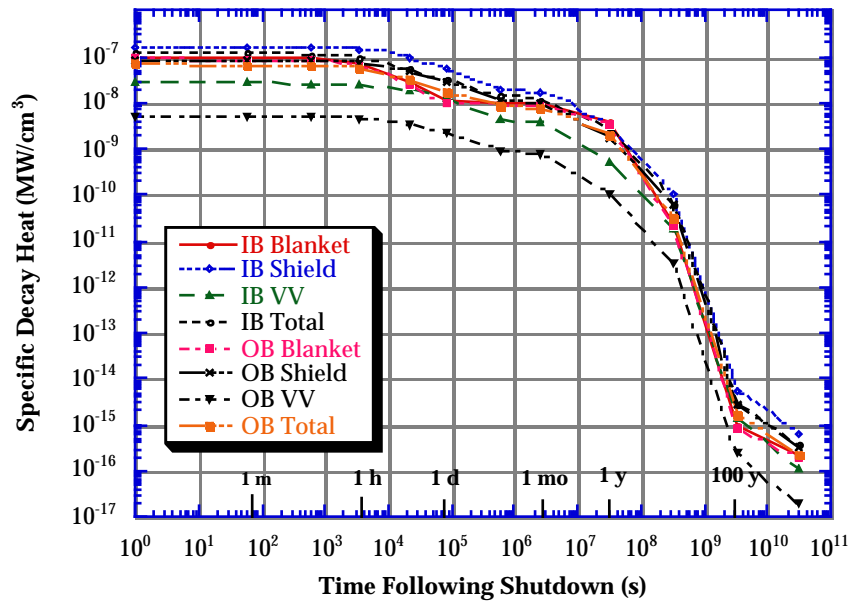


Figure 7.4-12: Decay heat induced in the different components of CLiFF as a function of time following shutdown.

7.5 Heat Transfer and Thermal-Hydraulics

Heat transfer to the flow liquid coolant is accomplished via two mechanisms, near surface photon and energetic particle absorption, and bulk heating by fusion neutrons. This first mechanism is of particular importance in determining the liquid surface temperature facing the plasma, which governs the evaporation rate. Particular focus is placed here on analyzing the phenomena responsible for free surface heat transfer and the effective thermal conductivity due to turbulence and surface deformation.

7.5.1 Free Surface Heat Transfer in Flibe

CLiFF FW flows were analyzed for Flibe using both the two-layer approach and the k - ϵ model. The two-layer approach is an analytical solution of the energy equation for a fully-developed heat transfer regime, while the k - ϵ modeling is based on the numerical solution of the flow equations along with the turbulence closure equations and the energy equation. Both the approaches need some empirical information on near-surface phenomena. At present this information is not complete, and to our knowledge, it is not present at all for MHD free surface flows. Nevertheless some estimations of unknown quantities were done using empirical correlations for turbulent parameters with and without a magnetic field. Detailed description of this can be found in Chapter 5. We believe that use of two independent approaches for estimating the surface temperature rise (the surface temperature minus the bulk temperature) give us more reliable data, and so have analyzed two cases, with and without the magnetic field. The two-layer calculational results for the case when the magnetic field is absent along with some additional parameters, are presented in Table 7.5-1. The same model was also used to estimate the surface temperature rise in the presence of the magnetic field. In this analysis, the velocity is approximately 10 m/s and the flow depth is 2 cm. The surface heat flux is 2 MW/m², and the thermal conductivity is 1.06 W/(m·K). The magnetic field is 10 T, so that the Hartmann number built through the hydraulic diameter is about 40. From the tables one can see that there is a small reduction of heat transfer by the magnetic field.

The phenomenon of the heat transfer degradation due to turbulent suppression by the magnetic field has also been illustrated experimentally by different authors only for closed channel flows. Here, we use a formula obtained by Blums [1], which generalizes his experimental data on heat transfer for rectangular duct MHD flows of a water solution of KOH. In accordance with this formula, the heat transfer coefficient is reduced by $(1 - 1.2Ha^2/Re)$ times. The results of the calculations for free surface flows are in a qualitative, and also in a quantitative agreement with the Blums formula. Namely, both the Blums formula and the two-layer model demonstrate negligible effect of the magnetic field on the turbulent heat transfer if the layer is thin. There are, however, two very important parameters for the two-layer model of the turbulent heat transfer. They are the effective thermal conductivity in the bulk and the thickness of the near-surface layer. Unfortunately, these parameters are not defined clearly up until now for free surface flows, and hence there is a large uncertainty in this simple model. In the analysis, very rough values of these parameters were used.

The k- ϵ model of turbulence is a more accurate approach, but it takes much more effort to implement. In this study, to quantify more accurately the effect of turbulence on the surface temperature we used the low-Reynolds number k- ϵ model of turbulence. In comparison to the ordinary k- ϵ model, the present one was extended to the MHD case by means of additional terms in closure equations. This procedure was discussed in detail in Chapter 5, and will not be repeated here. The equations described above are augmented by the energy equation as follows:

$$\frac{\partial T}{\partial t} + U \frac{\partial T}{\partial x} + V \frac{\partial T}{\partial y} = \frac{1}{Pe} \frac{\partial}{\partial y} \left[\left(1 + \frac{\nu_t}{\sigma_T} \text{Pr} \right) \frac{\partial T}{\partial y} \right] + q_v \quad (7.5-1)$$

The thermal boundary conditions for equation (7.5-1) specify a constant heat flux at the free surface and a thermally isolated back-wall. The symbol σ_t stands for the turbulent Prandtl number. In our calculations we assume $\sigma_t = 1$.

The surface temperature rise (the surface temperature minus the initial temperature) is shown in Figure 7.5-1 for several possible turbulent boundary conditions at the free surface. Curve 4 in this figure was calculated using a zero surface turbulence boundary condition. As it was mentioned, this variant of boundary conditions is an attempt to simulate the mechanism of suppression of the turbulent transport in the near-surface region. This phenomenon is usually caused by the turbulence redistribution in the surface vicinity due to both the geometrical restrictions and the gravitational force. By doing this, some analogy with the two-layer scheme is realized in the model. In accordance with this curve, the temperature maximum is about 160 K. It corresponds to the value calculated with the two-layer model in the previous section. The curve 2 was calculated using Naot's boundary condition [2]. It shows an improvement in surface heat transfer compared with curve 4, since in the variant with the Naot's boundary condition a finite turbulence intensity is still allowed in the near-surface layer.

The curve 3 was calculated for zero surface turbulence boundary conditions, but volumetric (Bremsstrahlung) heating was included into the model. This curve goes between the other two. In order to illustrate the effect of turbulence on the surface temperature, the results of calculations for a laminar flow are also presented (Figure 7.5-2). It can be seen that the difference is significant.

As a final result, we would like to give a range of the maximum temperature rise, which comes from our calculations. In accordance with the k- ϵ computations, this range is 30-160 K (depending on which boundary conditions are used). Taking into account the effect of penetration (Bremsstrahlung heating), it is 30-70 K.

The effect of the magnetic field on the turbulent heat transfer is illustrated in Figure 7.5-3. The Hartmann number was varied from zero to 3000. The Hartmann number, which corresponds to CLiFF parameters for Flibe is 560. The effect of heat transfer degradation due to the magnetic field increase at this Ha is negligible. All curves in Figure 7.5-3 were computed with Naot's boundary conditions for surface heating that

correspond to the lower level in our estimations of the temperature rise. The curves 1 ($Ha=0$) and 2 ($Ha=560$) are very close. It confirms again that the influence of the magnetic field on heat transfer for the Flibe thin liquid wall flows is negligible. At the same time, the curves 3 and 4 show a much larger temperature rise that is a consequence of the turbulence reduction.

7.5.2 Free Surface Heat Transfer in Liquid Metals

The temperature profile of the liquid metal FW can be calculated assuming that conduction is the dominant heat transfer mechanism. We calculate the temperature field, then, using a three-dimensional finite difference heat transfer code for a combined surface heat load of 2 MW/m^2 and neutron wall load of 10 MW/m^2 . The code takes the velocity profile as an input parameter and solves the energy equation. The volumetric heating due to both neutron and finite penetration of x-rays are accounted in the source term, q''' . In cases where x-ray penetration is insignificant, the surface heat flux is accounted for as a boundary condition. To adequately simulate the sharp heat deposition gradient, finer meshes are required in the first 1 cm of the liquid wall close to the plasma side.

The surface and bulk temperature distributions as fluids proceed downstream are shown in Figure 7.5-4 for lithium slug jets; while temperature profiles into the jets at about two meters downstream are shown in Figure 7.5-5. As shown, accounting for x-ray penetration significantly reduces the jet surface temperature, particularly in the case where the Bremsstrahlung radiation spectrum is very hard (for the case shown a classical Bremsstrahlung radiation spectrum corresponding to an average T_e of 10 KeV is assumed [3]). Nevertheless, most of the Bremsstrahlung radiation is deposited within the 1st cm of the jet. The peak surface temperatures as shown for 1 cm thick lithium and Flibe jets under the hard Bremsstrahlung radiation heating for the coolant velocity of 20 m/s and 10 m/s are 327 and 375°C respectively. The later value corresponds to a surface temperature rise $< 150^\circ\text{C}$, which is used in design calculations for the base case thermalhydraulics. The case for Sn-Li, calculations indicate that since there will be no appreciable penetration of X-ray photons, the surface temperature rise will be $\sim 300^\circ\text{C}$.

7.5.3 Bulk Coolant Thermal-Hydraulics

The temperature and pressure of the bulk coolants as they proceed through the CLiFF liquid wall reactor have been calculated using simple correlations in an excel spread sheet program. Relevant output for the working liquids Li, Sn-Li and Flibe are summarized in Tables 7.5-2 through 7.5-4, and in Figures 7.5-6 through 7.5-8 (which illustrates the system very nicely). No serious attempt has been made to optimize the flowrates and film thicknesses for different working liquids in order to achieve optimum thermal-hydraulic performance, and these results serve only as a indicator of what to expect.

In keeping with the results of the surface heat transfer calculations, the surface temperature rise for a 2 cm thick, 10 m/s Flibe and Sn-Li flow are taken as 25°C and 300°C respectively. The Flibe value assumes a very effective thermal transport via surface turbulence and wave formation. For lithium, a faster velocity was required to keep the surface temperature down to an acceptable level. For a 2 cm thick, 15 m/s lithium CLiFF flow, the surface temperature rise is taken as 100°C. This value assumes hard X-rays carry a major portion of the surface heat.

Other assumptions implicit in these calculations are an ARIES-RS size reactor scaled to 4500 MW fusion power, 75% of the alpha energy going to the FW as radiation, and a multiplication factor of 1.15. For Flibe and Sn-Li, 15% of the neutron heat is assumed absorbed in the FW layer, for lithium 7% is assumed (see neutronics in Chapter 5). The inlet temperature of lithium is assumed to be 325°C, in order to be practically utilized for power conversion using a steam cycle (more on this in the next subsection). The inlet temperature of both Sn-Li and Flibe are made as high as possible whilst still keeping the surface temperature under an assumed maximum. For these calculations, the maximum surface temperatures allowed for lithium, Flibe, and Sn-Li are 460, 560, and 750°C respectively.

The thermal hydraulic results vary considerably for the different working liquids. For Flibe, an outlet temperature of 600°C is achieved with a reactor mass flowrate of 21 metric tons/second. The pumping power, assuming complete loss of the velocity and gravity head and a friction pressure drop equal to the velocity head, is on the order of 3.5 MW. The viability of such a Flibe system is critically linked to the surface heat transfer assumptions and the precise value of the allowable surface temperature, as little temperature window exists between the melting point of Flibe (460°C) and the maximum allowable surface temperature (here, 560°C).

For lithium, the volumetric flowrate is higher since the velocity was increased in order to reduce the surface temperature rise. In addition, the choice was made to only recycle 43% of the CLiFF flow to the blanket, so that the blanket outlet temperature would be high, ~600°C. These choices result in a two-stream outlet to the power conversion system. The stream outlet temperatures are 357/600°C at mass flowrates of 4.8/3.6 ton/s respectively. This two-outlet-stream option may not be the most optimum way to utilize the fusion power, since two different type of power conversion systems will be needed. As an alternative, if 100% of the CLiFF is recirculated to the blanket, the single outlet stream will be at 461°C and a flowrate of 8.5 ton/s.

For Sn-Li, due to the higher allowable surface temperature of this alloy, a single stream implementation is possible where an inlet temperature of 400°C results in an outlet temperature of 640°C at a mass flowrate of 80 ton/s. This high mass flowrate results from the high density of the Sn alloy. But a higher inlet and outlet temperature is possible with this alloy, leading to greater thermal efficiency.

Probably the greatest issue with the liquid metal systems is related to the MHD drag. As discussed in the hydrodynamics sections, no conducting penetrations are allowable for

these systems, without excessive thickening and slowing-down of the liquid free surface flow. This will result in high surface temperatures in the affected regions. Drag on the flow when crossing toroidal field gradients will also affect the flow in a similar fashion. The magnitude of this effect has not yet been quantified, but appears to be significant. Overcoming field gradients may require active pumping or going to thinner flows, since the drag will appear regardless of the presence of insulator coatings or toroidal axisymmetry.

In addition to the free surface flow itself, there is also a serious concern about the liquid supply lines as they enter the magnetic field between two adjacent toroidal field coils. As is evident from the spread-sheet calculations, the pressure drop, and resulting pumping power requirements are estimated to be extremely high for both Lithium and Sn-Li at the flowrates needed for CLiFF. Using the established correlation,

$$\Delta p = k\sigma u B^2 D \quad (7.5-2)$$

with $k = 0.04$ [4] for entrance lengths equal to the pipe diameter for insulated pipes, the pressure drop associated with the field entrance region can be many MPa. The associated pumping power for the lithium system skyrockets to 14% of the fusion power! The Sn-Li system also has a very high pumping power requirement. It may be possible to design around this problem to some degree by elongating supply channels along the toroidal field and using multiple small channels to carry the need LM supply, but this problem needs to be carefully evaluated at the high flowrates required for CLiFF.

Stresses and temperatures in the structures have not been analyzed yet in detail.

7.5.4 Power Cycle and Balance of Plant

A summary of the critical parameters for power conversion system are given in Table 7.5-5. This information is used to define the power conversion system and the thermal converting efficiency. For coolant exit temperature below 650°C, the most efficient power conversion system is by Rankine cycle. The cut off temperature to start to consider more advanced cycle is about 650°C. Therefore, the only system for which a more advanced cycle can be considered is the Sn-Li system. Even for this system, a more efficient Rankine cycle can be designed.

To design a Rankine cycle, both the coolant maximum temperature and the minimum temperature have to be considered. The maximum coolant temperature determines the steam temperature and pressure, which determines the power converting efficiency. The minimum temperature governs the pinch-point problem, which will determine if a design of the steam generator is possible. The low temperatures of the three systems are all above 325°C. Therefore, the pinch-point problem is not an issue. An EPRI study evaluated such power conversion systems for advanced pulverized-coal power plant [5].

The systems being evaluated are summarized in Table 7.5-6 and the power conversion results are reported at the bottom of Table 7.5-5. These results show that the Sn-Li system has the highest electrical power output due to the higher outlet temperature. The Li system has the worst efficiency, and it is uncertain whether the two outlet-steam approach is the best design from a power producing viewpoint. Finding a way to accommodate lower flowrates for Li where all CLiFF flow can be recirculated to the blanket will be of great benefit.

References for Section 7.5

1. Blums E., Mikhailov Yu.A., Ozols R. Heat and Mass Transfer in MHD Flows. Series in Theoretical and applied Mechanics, Vol.3 (1987).
2. Naot D., Rodi W. Calculation of Secondary Currents in Channel Flow, Proc. ASCE, 108, No.HY8, 948 (1982).
3. M. Youssef, N. Morley and A. El-Azab, X-Ray surface and volumetric heat deposition and tritium breeding issues in liquid-protected FW in high power density devices, Fusion_Technology, 34, No. 3, 697-705 (1998)
4. Lielausis O. Liquid Metal Magnetohydrodynamics, Atomic Energy Review, 13, 527 (1975).
5. G. M. Yasenchak, et al., Engineering Assessment of an Advanced Pulverized-Coal Power Plant, EPRI CS-5255, August 1982

Table 7.5-1: Surface temperature rise estimations for thin liquid wall concepts with Flibe using the two-layer analytic model

Concept	$\alpha, W/(m^2 \times K)$	$\lambda_t, W/(m \times K)$	$\Delta T, K$	$(\Delta T)_\delta, K$	$(\Delta T)_b, K$
No Field	14100	94	144	4	140
11 T Field	13570	90.5	149.5	4	145.5

Table 7.5-2: Thermal hydraulic calculations for Flibe

ARIES PARAMETERS (given)			FLOW (calculated)		
fusion power	4500	MW	FW flowrate/sector, outboard	0.37	m3/s
energy multiplication factor	1.15		FW flowate/sector, inboard	0.30	m3/s
total reactor thermal power	5040	MW	FW flowrate/sector	0.66	m3/s
major radius	5.52	m	FW flowrate/reactor	10.6	m3/s
minor radius (midplane)	1.38	m	FW mass flowrate/sector, outboard	731	kg/s
X-point major radius	4.70	m	FW mass flowrate/sector, inboard	585	kg/s
number of field coils (sectors)	16		FW mass flowrate/sector	1315	kg/s
sector angle	22.50	deg	FW mass flowrate/reactor	21	ton/s
inboard sector width, midplane	1.63	m	FW supply pipe diameter, sector	41	cm
outboard sector width, midplane	2.71	m			
magnetic field strength, outboard	7.00	T	POWER BALANCE (calculated)		
magnetic field strength, inboard	11.00	T	CLiFF temperature rise	30.4	C
module width, top	1.85	m	Blanket temperature rise	70.2	C
fusion power per sector	281.25	MW	total temperature rise	101	C
			CLiFF outlet temperature	530	C
CLIFF PARAMETERS (given)			Blanket outlet temperature	601	C
inlet temperature	500	C	Average N wall load	7.10	MW/m2
liquid layer initial depth, outboard	2.00	cm	Average FW surface heat load	1.9	MW/m2
liquid layer initial depth, inboard	2.00	cm	Average Divertor heat load	7.6	MW/m2
liquid layer initial velocity, outboard	10.00	m/s	FW surface temperature rise	25	C
liquid layer initial velocity, inboard	8.00	m/s	Divertor surface temperature rise	25	C
radius of curvature, outboard	3.40	m	Peak FW surface temperature	555	C
radius of curvature, inboard	5.00	m			
maximum inverted angle, outboard	80	deg	REACTOR OUTLET (calculated)		
maximum inverted angle, inboard	45	deg	Stream 1 (from FW) temp	530	C
FW flow length, outboard	8.31	m	Stream 1 mass flowrate	0.00	ton/s
FW flow length, inboard	5.50	m	Stream 1 total power	0.00	MW
inlet pipe velocity limit	5.00	m/s	Stream 2 (from B) temp	601	C
nuclear heat absorbed in FW flow	15%	%	Stream 2 mass flowrate	21	ton/s
FW flow recirculated to blanket	100%	%	Stream 2 total power	5040	MW
			total output thermal power	5040	MW
GEOMETRY (calculated)					
FW width expansion, outboard	47%		PUMPING POWER (calculated)		
FW width decrease, inboard	12%		velocity head loss, FW inboard	63	kPa
centrifugal/gravity force, outboard	3.04		velocity head loss, FW outboard	99	kPa
centrifugal/gravity force, inboard	1.85		FW gravity head loss, both	146	kPa
FW area, outboard	302.7	m2	piping head loss (k=1)	99	kPa
FW area, inboard	143	m2	FW pumping power estimate	3.5	MW
Divertor area	29.5	m2	Fraction of Fusion Power	0.08%	%
Total area	475	m2			
LIQUID PROPERTIES (given)					
density	1980	kg/m3	heat capacity	2380	J/kg.K
kinematic viscosity	7.6E-6	m2/s			
electrical conductivity	155	1/ohm.m			

Table 7.5-3: Thermal hydraulic calculations for Lithium

ARIES PARAMETERS (given)			FLOW (calculated)		
fusion power	4500	MW	FW flowrate/sector, outboard	0.52	m3/s
energy multiplication factor	1.15		FW flowrate/sector, inboard	0.52	m3/s
total reactor thermal power	5040	MW	FW flowrate/sector	1.03	m3/s
major radius	5.52	m	FW flowrate/reactor	16.5	m3/s
minor radius (midplane)	1.38	m	FW mass flowrate/sector, outboard	264	kg/s
X-point major radius	4.70	m	FW mass flowrate/sector, inboard	264	kg/s
number of field coils (sectors)	16		FW mass flowrate/sector	528	kg/s
sector angle	22.50	deg	FW mass flowrate/reactor	8.5	ton/s
inboard sector width, midplane	1.63	m	FW supply pipe diameter, sector	51.3	cm
outboard sector width, midplane	2.71	m			
magnetic field strength, outboard	7.00	T	POWER BALANCE (calculated)		
magnetic field strength, inboard	11.00	T	CLiFF temperature rise	32.3	C
module width, top	1.85	m	Blanket temperature rise	243	C
fusion power per sector	281.25	MW	total temperature rise	275	C
			CLiFF outlet temperature	357	C
CLiFF PARAMETERS (given)			Blanket outlet temperature	600	C
inlet temperature	325	C	Average N wall load	7.10	MW/m2
liquid layer initial depth, outboard	2.00	cm	Average FW surface heat load	1.89	MW/m2
liquid layer initial depth, inboard	2.00	cm	Average Divertor heat load	7.62	MW/m2
liquid layer initial velocity, outboard	14.00	m/s	FW surface temperature rise	100	C
liquid layer initial velocity, inboard	14.00	m/s	Divertor surface temperature rise	100	C
radius of curvature, outboard	3.40	m	Peak FW surface temperature	457	C
radius of curvature, inboard	5.00	m			
maximum inverted angle, outboard	80	deg	REACTOR OUTLET (calculated)		
maximum inverted angle, inboard	45	deg	Stream 1 (from FW) temp	357	C
FW flow length, outboard	8.31	m	Stream 1 mass flowrate	4.8	ton/s
FW flow length, inboard	5.50	m	Stream 1 total power	678	MW
inlet pipe velocity limit	5.00	m/s	Stream 2 (from B) temp	600	C
nuclear heat absorbed in FW flow	7%	%	Stream 2 mass flowrate	3.63	ton/s
FW flow recirculated to blanket	43%	%	Stream 2 total power	4362	MW
			total output thermal power	5040	MW
GEOMETRY (calculated)					
FW width expansion, outboard	47%		PUMPING POWER (calculated)		
FW width decrease, inboard	12%		velocity head loss, FW inboard	50	kPa
centrifugal/gravity force, outboard	5.97		velocity head loss, FW outboard	50	kPa
centrifugal/gravity force, inboard	5.65		FW gravity head loss, both	37	kPa
FW area, outboard	302.	m2	Entrance to field	39517	kPa
FW area, inboard	143	m2	FW pumping power estimate	655	MW
Divertor area	29.5	m2	Fraction of Fusion Power	14%	%
Total area	475	m2			
LIQUID PROPERTIES (given)					
density	511	kg/m3	heat capacity	4361	J/kg.K
kinematic viscosity	1.12E-6	m2/s			
electrical conductivity	3.9E+6	1/ohm.m			

Table 7.5-4: Thermal hydraulic calculations for Sn-Li

ARIES PARAMETERS (given)			FLOW (calculated)		
fusion power	4500	MW	FW flowrate/sector, outboard	0.37	m3/s
energy multiplication factor	1.15		FW flowrate/sector, inboard	0.37	m3/s
total reactor thermal power	5040	MW	FW flowrate/sector	0.74	m3/s
major radius	5.52	m	FW flowrate/reactor	11.81	m3/s
minor radius (midplane)	1.38	m	FW mass flowrate/sector, outboard	2496	kg/s
X-point major radius	4.70	m	FW mass flowrate/sector, inboard	2496	kg/s
number of field coils (sectors)	16		FW mass flowrate/sector	4991	kg/s
sector angle	22.50	deg	FW mass flowrate/reactor	79.9	ton/s
inboard sector width, midplane	1.63	m	FW supply pipe diameter, sector	43.4	cm
outboard sector width, midplane	2.71	m			
magnetic field strength, outboard	7.00	T	POWER BALANCE (calculated)		
magnetic field strength, inboard	11.00	T	CLiFF temperature rise	72	C
module width, top	1.85	m	Blanket temperature rise	167.3	C
fusion power per sector	281.25	MW	total temperature rise	239.7	C
			CLiFF outlet temperature	472	C
			Blanket outlet temperature	639	C
CLiFF PARAMETERS (given)			Average N wall load	7.10	MW/m2
inlet temperature	400	C	Average FW surface heat load	1.89	MW/m2
liquid layer initial depth, outboard	2.00	cm	Average Divertor heat load	7.62	MW/m2
liquid layer initial depth, inboard	2.00	cm	FW surface temperature rise	300	C
liquid layer initial velocity, outboard	10.00	m/s	Divertor surface temperature rise	300	C
liquid layer initial velocity, inboard	10.00	m/s	Peak FW surface temperature	772	C
radius of curvature, outboard	3.40	m			
radius of curvature, inboard	5.00	m	REACTOR OUTLET (calculated)		
maximum inverted angle, outboard	80	deg	Stream 1 (from FW) temp	472	C
maximum inverted angle, inboard	45	deg	Stream 1 mass flowrate	0.00	ton/s
FW flow length, outboard	8.31	m	Stream 1 total power	0.00	MW
FW flow length, inboard	5.50	m	Stream 2 (from B) temp	639.7	C
inlet pipe velocity limit	5.00	m/s	Stream 2 mass flowrate	79.9	ton/s
nuclear heat absorbed in FW flow	15%	%	Stream 2 total power	5040	MW
FW flow recirculated to blanket	100%	%	total output thermal power	5040	MW
GEOMETRY (calculated)			PUMPING POWER (calculated)		
FW width expansion, outboard	47%		velocity head loss, FW inboard	338	kPa
FW width decrease, inboard	12%		velocity head loss, FW outboard	338	kPa
centrifugal/gravity force, outboard	3.04		FW gravity head loss, both	497	kPa
centrifugal/gravity force, inboard	2.88		Entrance to field	15737	kPa
FW area, outboard	302.76	m2	FW pumping power estimate	196	MW
FW area, inboard	143.07	m2	Fraction of Fusion Power	4.35%	%
Divertor area	29.53	m2			
Total area	475.36	m2			
LIQUID PROPERTIES (given)					
density	6761	kg/m3	heat capacity	263	J/kg.K
kinematic viscosity	2.7E-7	m2/s			
electrical conductivity	1.9E+6	1/ohm.m			

Table 7.5-5: Power Conversion Cycle Summary

	Flibe	Lithium		Sn-Li
Heat Capacity, J/kg.K	2380	4361		263
Number of Streams	1	2		1
Mass Flowrate, ton/s	21	4.8	3.6	80
High Temperature, C	601	357	600	640
Low Temperature, C	500	325	325	400
Thermal Power, MW	5040	678	4362	5040
Steam Pressure, MPa	31	8.5	31.8	31
Steam Temp, C	538	320	538	566
Rehat. Temp, C	552/566	---	552/566	579/593
Thermal Efficiency, %	44.6	32	44.6	46.9
Electrical Power, MW	2249	2162		2364

Table 7.5-6: Steam conditions Evaluated

<u>Availability</u>	<u>Steam Conditions</u>
Current	23.6MPa/538C/552C/566C
	31.0MPa/538C/552C/566C
Advanced	31.0MPa/566C/579C/593C
	23.6MPa/593C/607C/621C
	31.0MPa/593C/621C/649C
Futuristic	44.8MPa/649C/691C/732C

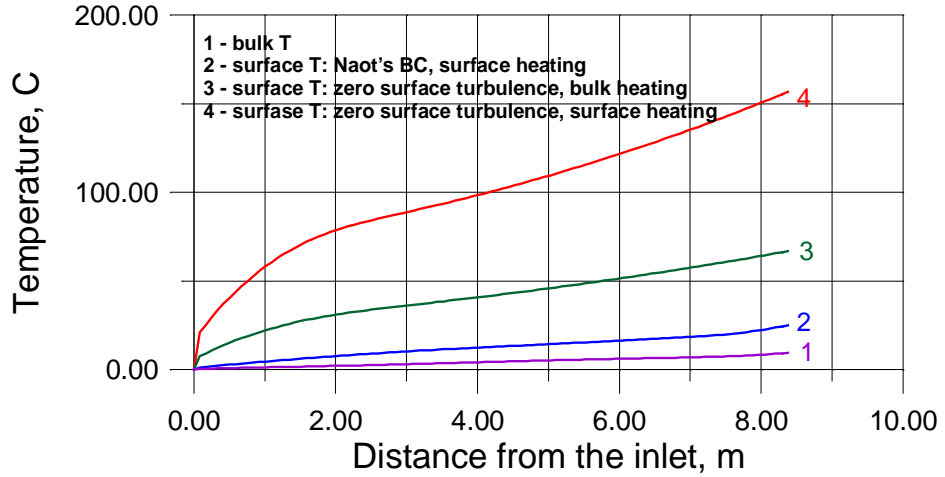


Figure 7.5-1: Temperature rise vs. distance from the inlet cross-section in the turbulent regime.

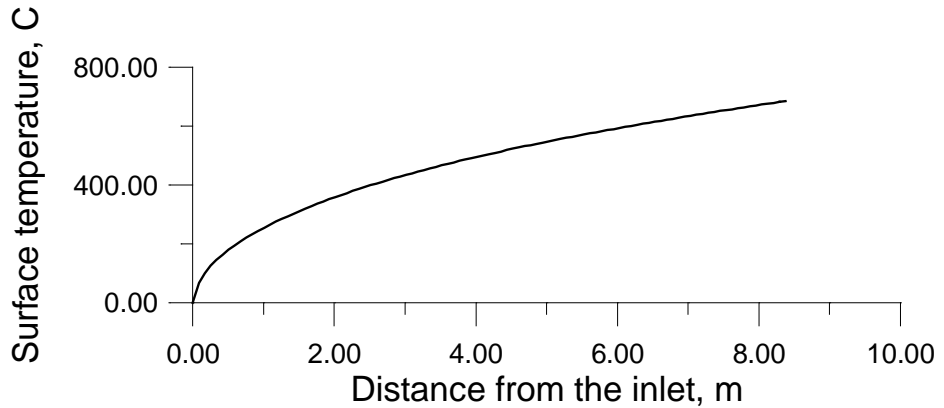


Figure 7.5-2: Temperature rise vs. distance from the inlet cross-section in a laminar regime.

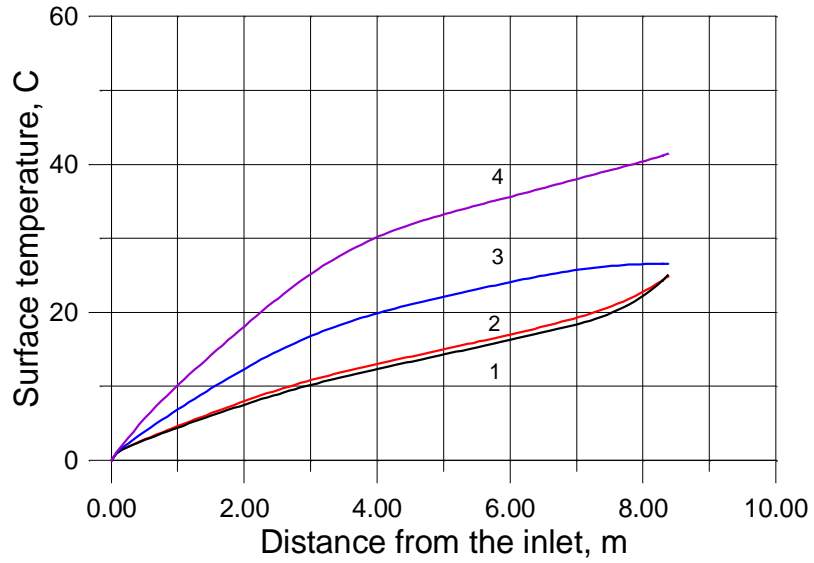


Figure 7.5-3 The effect of heat transfer degradation due to magnetic field. 1- $Ha=0$; 2- $Ha=560$; 3- $Ha=2000$; 4- $Ha=3000$

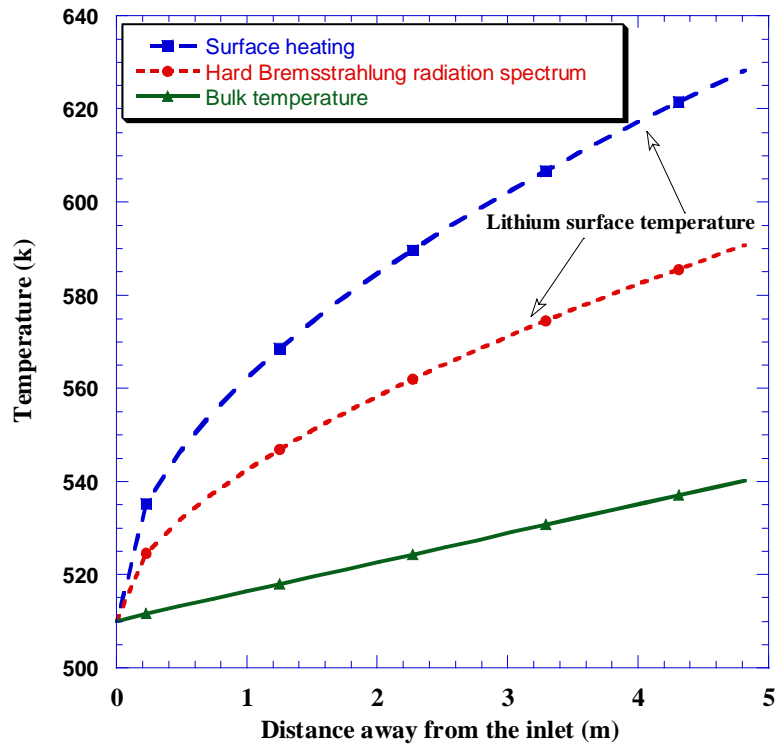


Figure 7.5-4: Lithium surface and bulk temperature assuming 20 m/s and various cases of photon spectrum.

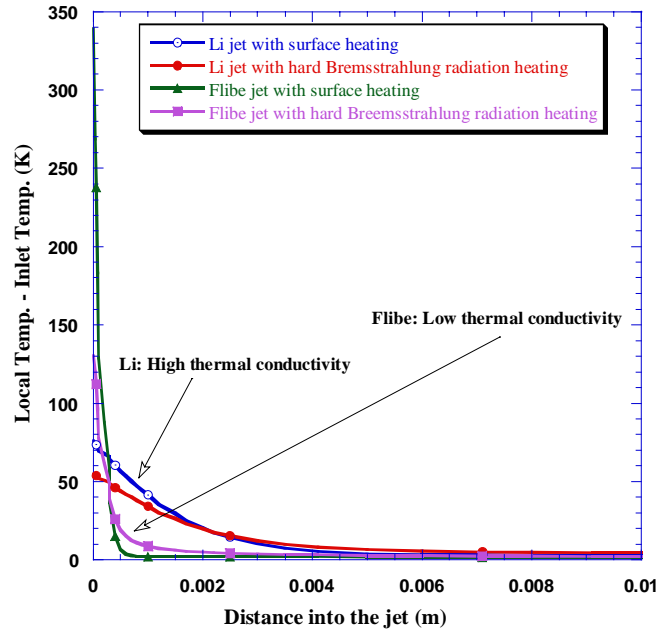


Figure 7.5-5: Temperature increases inside the jets at about 2 m downstream under different heating conditions. (jet velocity =20 m/s, 1 cm thick jet)

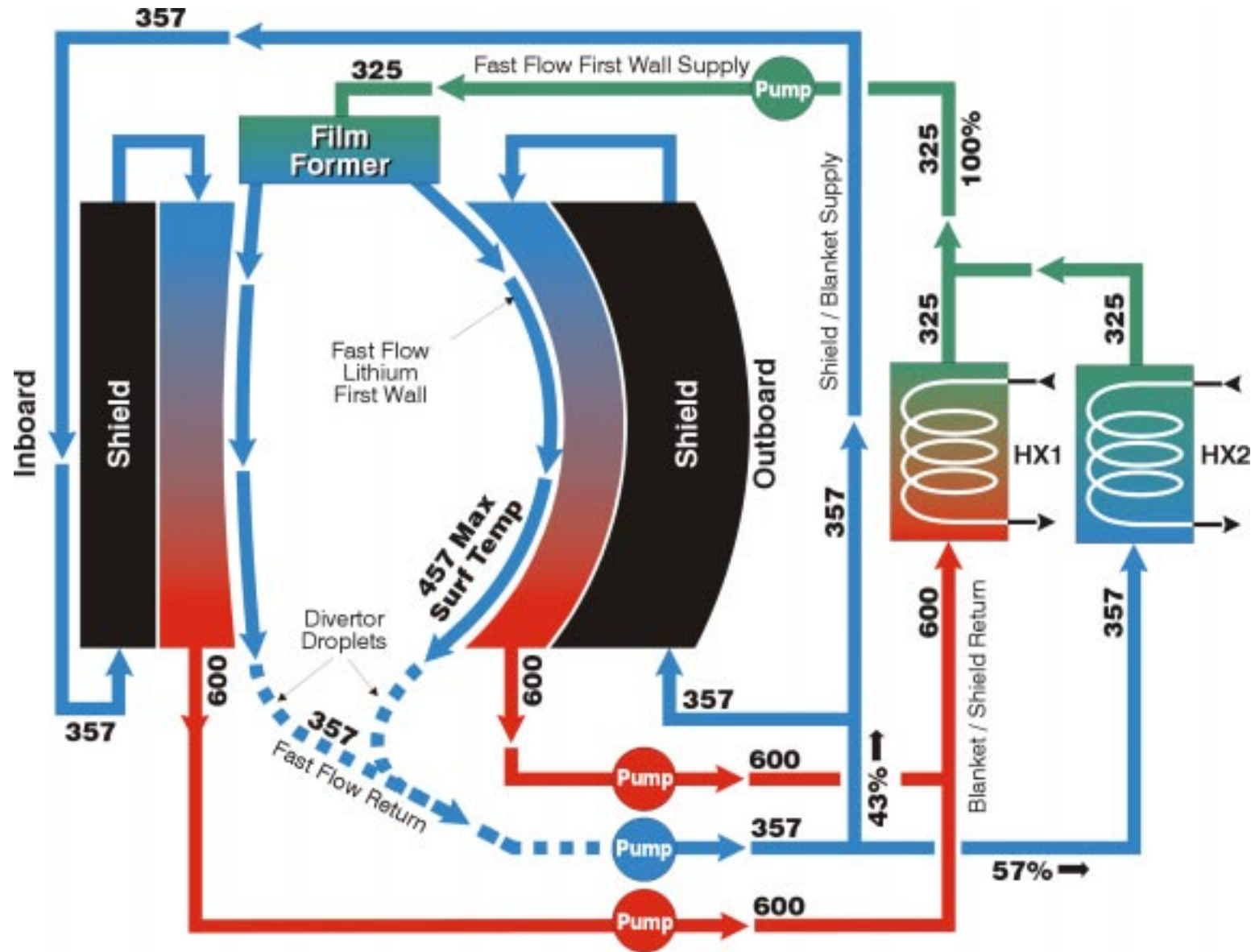


Figure 7.5-6: CLiFF – Flow / Temperature Schematic-Lithium option.

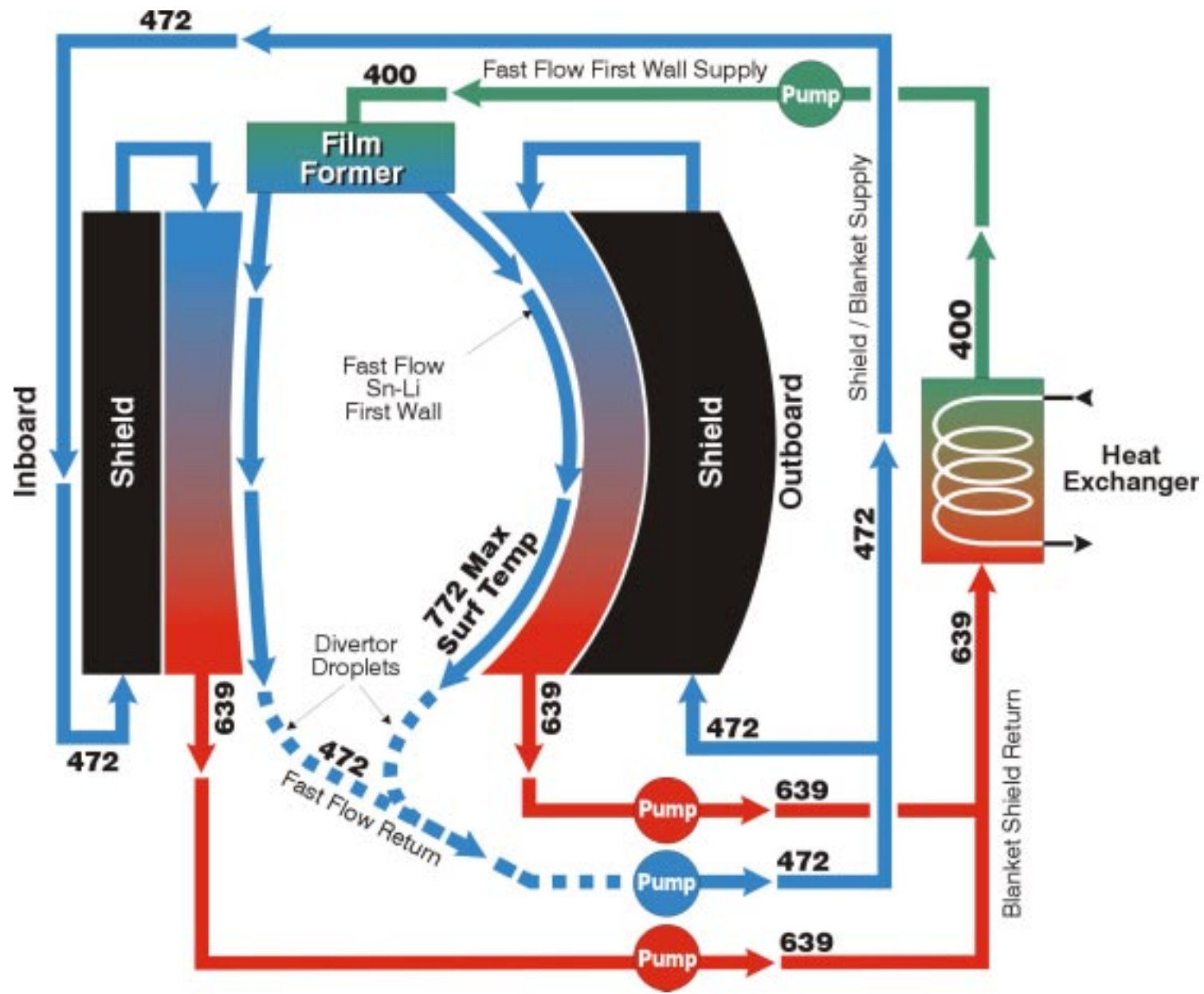


Figure 7.5-7: CLiFF – Flow / Temperature Schematic-Sn-Li option.

7.6 Mechanical Design and Maintenance Approach

7.6.1 Mechanical Design Features and Configuration Layout

The mechanical design of the CLiFF concept must satisfy the basic APEX design goals listed in Table 7.6-1. These goals include minimum limits on wall loading, shielding, tritium breeding, and availability as well as provisions for heating and diagnostic penetrations, vacuum pumping, and plasma exhaust (divertor). The CLiFF liquid first wall concept is not limited to a particular fusion reactor configuration, and may be adapted to both magnetic and inertial confinement designs. For the purpose of the mechanical design and maintenance study, however, the ARIES-RS reactor design was chosen as the basic configuration. This choice provides a relatively difficult design challenge and allows direct comparison between the “conventional” first wall/blanket design used for the ARIES-RS study and the CLiFF high power density, liquid first wall.

In order to meet the intent of the APEX study and adapt the CLiFF concept, several changes were required to the baseline ARIES-RS design. First the power density was approximately doubled to obtain the correct surface heat flux and neutron wall load specified by the APEX design goals. A list of the ARIES-RS parameters and APEX modifications are listed in Table 7.6-2. Second, in order to accommodate the liquid wall, the ARIES-RS configuration was changed from double null to single null with the divertor at the bottom of the reactor. The shape of the first wall was also modified to reduce the horizontal component of flow at the upper part of the machine. Figure 7.6-1 shows a comparison of the ARIES-RS and the modified configuration for the CLiFF concept geometry.

The CLiFF concept replaces the conventional first wall of a fusion reactor with a thin, fast flowing convective layer of a low vapor pressure liquid. The liquids under consideration include lithium, Flibe or Sn-Li. The mechanical design must incorporate a convective layer forming device, a convective layer collecting system, a concept for starting the system, a concept for providing heating and diagnostic penetrations, a vacuum pumping concept and a divertor concept. Figures 7.6-2 and 7.1-1 illustrate the CLiFF concept, showing the various systems.

7.6.1.1 Convective layer forming device

The convective layer forming device is located at the top of the blanket array. Its primary function is to evenly distribute a layer of fast flowing liquid on the plasma-facing surfaces of the blanket. It must split the stream into inboard and outboard paths, distributed uniformly in the toroidal direction. The stream must have sufficient velocity in the poloidal direction (~20 m/s) to avoid excessive temperature rise or thinning as it travels from the top to the bottom of the reactor. In addition, the device must not interfere with shielding function at the top of the machine.

A first concept for the convective layer forming device is shown in Figure 7.6-3. The device consists of a set of cassettes that can be removed and replaced independently from the rest of the reactor internals. The cassettes are arranged such that they form a continuous array at the top of the reactor. Each cassette contains piping, shielding, and a set of nozzles that direct the flow to the inboard and outboard plasma facing surfaces.

The inboard flow is completely poloidal in direction, with no toroidal component that would tend to separate the flow from the inboard blanket surface. The outboard flow is both poloidal and toroidal, with both components of velocity tending to force the liquid against the outboard blanket surface. The ability to inject the outboard stream in the toroidal direction is important, since it provides a means of protecting each nozzle with the flow from adjacent nozzles. Each nozzle is canted at a 20 degree angle from the horizontal and a 45 degree angle to the radial plane. The inboard flow is injected below the outboard flow within a nozzle, but the outboard flow is injected at an angle under the neighboring nozzle. This overlapping system shields the entire nozzle array such that none of the nozzles are exposed directly to the plasma heat flux. The cassettes and nozzles are not well shielded from the neutron fluence, however, and the nozzles and internal piping are subject to erosion and degradation from the high velocity flow. It must be assumed that replacement of the film forming cassettes will occur frequently, perhaps as often as once every two years.

7.6.1.2 Convective layer collecting system, divertor, and vacuum pumping

The liquid that flows down the plasma facing surfaces of the blanket must be collected at the bottom of the reactor. The collection system consists of a trough that directs the flow through openings between the toroidal field coils and into a duct. The duct also serves as the vacuum pumping duct. Prior to collection, the liquid is broken into droplets that form the divertor surface. The droplets are formed with a comb-like set of radial baffles that are mounted to the lower portions of the plasma-facing surfaces.

Both the divertor droplet forming features and the liquid collection trough surface are separately cooled and contained in a cassette. There is one cassette per sector, and it can be independently removed from the primary blanket module for maintenance. A typical cassette is shown in Figure 7.6-4.

The pumping duct is protected with a removeable sleeve that also provides radiation shielding for the duct wall and magnets. The duct is shown as 1 m in dia., which is large enough to carry the fluid as free surface flow. At 5 m/s, the duct would only be 1/3 full. The duct cannot be full, as this would prevent flow (except for very long ducts).

7.6.1.3 Concept for providing heating and diagnostic penetrations

Openings must be provided in the liquid wall for plasma heating and current drive systems and for diagnostics. The opening must be shaped to allow a smooth diversion of flow without splashing, or ejecting liquid into the plasma. An elongated shape, as shown

in Figure 7.1-1 , may be similar to what will work. Regardless of the shape, there must be a structure to deflect the liquid, and this structure will almost certainly be directly exposed to the plasma. For this reason, and because the heating and diagnostic systems themselves may need frequent maintenance, it is necessary to provide another cassette for each penetration. This is shown schematically in Figure 7.6-2.

7.6.1.4 Piping arrangement

The piping arrangement for the CLiFF concept consists of several separate sets of pipes. The first set is for the liquid first wall itself. The supply pipes are integrated with the film forming cassettes, and consist of separate pipes for each inboard nozzle and each outboard nozzle. The exit piping is integral with the pump duct, which carries the total flow into a reservoir from which it is pumped through a heat exchanger and back into the film forming system. There are separate piping systems for each divertor/collection trough cassette and for each heating/diagnostic penetration cassette.

The pressures and temperatures for the piping systems depends on the particular liquid employed for the first wall and blanket system. The schematics for three different liquids, lithium, Flibe, and Sn-Li are shown in the previous section in Figures 7.5-6 through 7.5-8 respectively.

7.6.2 Thermal and Pressure Stresses

No in-depth analysis has yet been performed in the area of thermal stress and pressure stresses in supply lines, blanket and nozzles. Nuclear heat in the nozzles and in the blanket structures necessitate a temperature gradient through all structural members to the coolant. The stress magnitude and implication on component failure must still be analyzed in detail, however, the elimination of the first wall heat flux makes the problem considerably more tractable than in solid wall designs. Analysis of components that still have a large heat flux, like antennae arrays and other mid-plane ports, must be looked at very carefully and jointly designed and analyzed with the cooperation of the Plasma Interface Group of the APEX team.

7.6.3 High Temperature Materials for Support Structures

Material choices will likely be the same as discussed for thick liquid wall concepts in Chapter 5.

7.6.4 Maintenance

High Maintenance Components: Maintaining the CLiFF configuration is based on designing removable cassettes for the components considered to be most likely to fail

during operation (liquid supply systems, film formers, heating elements, diagnostics devices, and divertors). To increase the availability factor of the machine, it is imperative that these high maintenance components can be rapidly replaced without having to disassemble the entire device. This approach also provides easy incorporation of new design elements and modifications for these components by simply removing the old cassettes and replacing them with the ready-to-install new cassettes (see Figure 7.6-5)

Low Maintenance Components: Repairing damage to the first wall / blanket / shield components and incorporating new modifications to these components will require “total sector removal”. These elements are extremely heavy and not designed to be remotely maintained or remotely transported.

Lifetime Components:

The vacuum vessel and coil sets are considered to be lifetime components and therefore need to be protected with adequate shielding. If repairs are required, the shielding minimizes the neutron damage to the vessel material and makes it possible to cut, remove, replace, and re-weld sections of the vessel. This procedure follows the sector removal process.

The main reason for “total sector removal” is that there is simply no access through the back of the blanket, nor from the top of the liquid supply system to be able to insert a remote device, and certainly not enough clearance to extract the large, bulky components. Basically, in order to get to the inboard first wall / blanket region, the outboard region must be removed first. In so doing, it would be easier and faster to remove a sector module intact. This would provide the needed access to all of the components in a hot cell in order to make necessary repairs and scheduled maintenance.

Even if there was adequate access to allow for remote maintenance and remote handling of damaged components, the probability is high that components will “stick” to each other and make removal a difficult task if any of the liquid leaks and then “freezes”. This situation is minimized with “total sector removal” because a component can literally be destroyed in order to extract it. In so doing, it is likely that the adjacent or attachment components could be damaged trying to free a single component.

It is therefore deemed prudent to do all major repairs of non-cassette components outside of the machine in a hot cell room, while at the same time, a replacement sector can be in the process of being installed concurrently.

There are numerous mechanical design issues associated with the CLiFF concept, including:

- How to design the piping and nozzles for reliable operation at high fluid velocity
- How to start and stop the system safely
- How to keep the stream attached to the inboard wall (must prevent toroidal rotation of inboard stream)

- How to provide sufficient penetrations for heating and diagnostics
- How to account for image current effects from moving plasma
- How to protect liquid from exposed surfaces (ie excessive vapor pressure if liquid hits hot spots)

Table 7.6-1: General Design Requirements

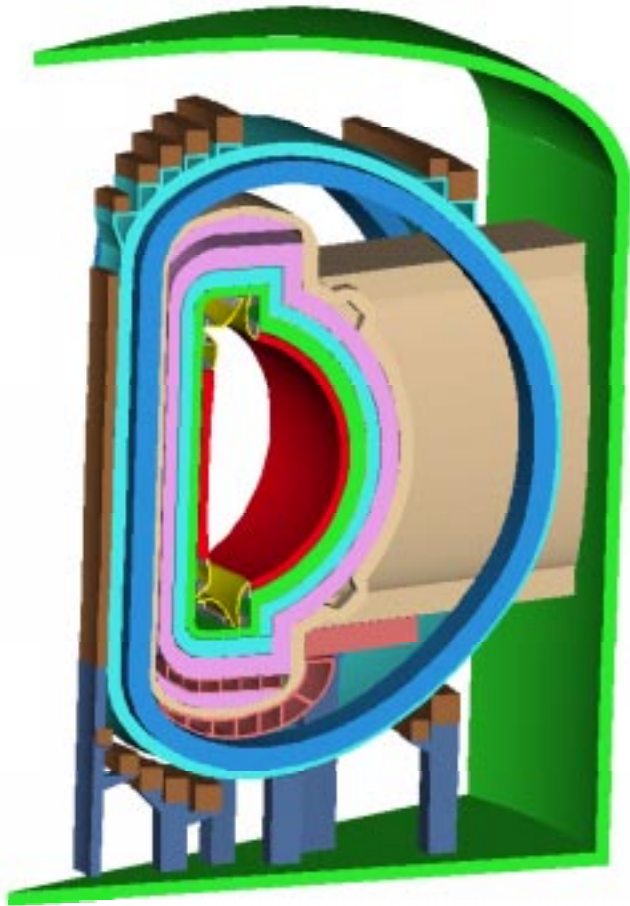
Function	Requirement	Value/Goal
Power Extraction	Neutron Wall Load Surface Heat Flux	7 MW/m ² avg* 10 MW/m ² peak* 2 MW/m ² *
Tritium Breeding	Self Sufficient	TBR > 1
Shielding	Radiation exposure of coils (insulation) Nuclear heating of coils (sc cable) Re-weldable confinement boundary	< 1x10 ⁹ Rad < 1kW/m ³ < 1 appm He
Vacuum	Compatible with plasma - Base partial pressure, non-fuel - Base pressure, fuel (H,D,T)	< 1x10 ⁻⁹ Torr < 1x10 ⁻⁷ Torr
Plasma Exhaust	Divertor required	to remove helium
Penetrations	Plasma Heating Power Density - NBI - ICH Diagnostics	~4 MW/m ² ~6 MW/ m ² viewing through labyrinth/mirrors
Operating Parameters	Pulse Length Number of pulses Disruptions	Steady State < 3,000 TBD
Availability	Maximize total availability	A _{plant} > .75 A _{blanket/FW} > .98
Safety	Confinement Boundaries	At least 2

* Values are minimum goals for steady state operation

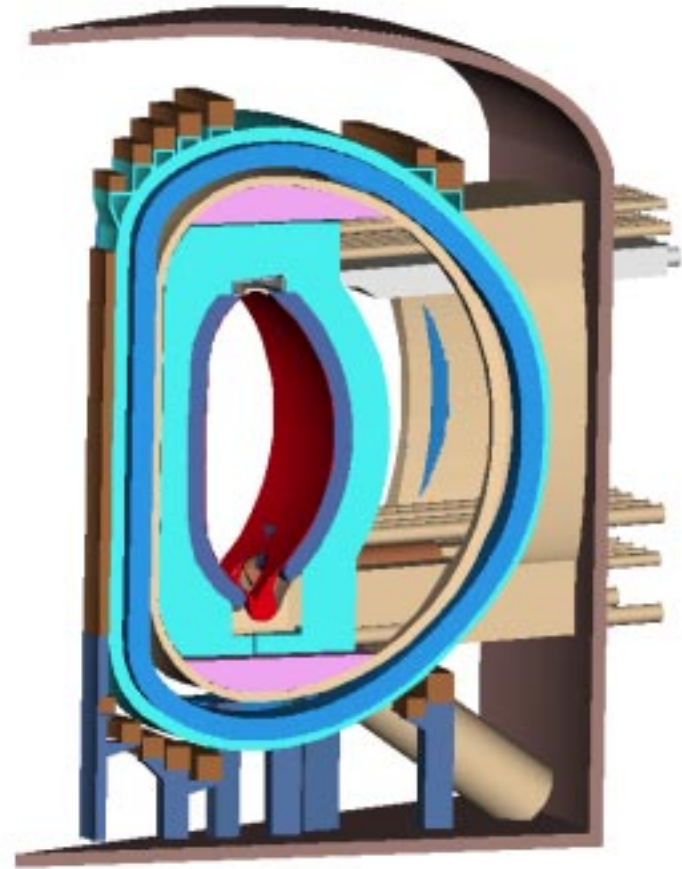
Table 7.6-2: ARIES RS Parameters & APEX modifications

	<u>ARIES*</u>	<u>APEX</u>
Major Radius	5.52	same
Minor Radius	1.38	same
Plasma Aspect Ratio	4	same
Number of Sectors	16	same
Fusion power (MW)	2171	~ 4000
Neutron Power (MW)	1736	~ 3400
Alpha power (MW)	433	~ 600
Fusion power density (MW/m ³)	6.38	~ 12
Average neutron load (MW/m ²)	4.03	7
Peak neutron load (MW/m ²)	5.67	10
Ave. FW surface heat flux (radiative), MW/m ²	0.4	1.5
Peak FW surface heat flux, MW/m ²	0.47	2

* Ref <http://aries.ucsd.edu/PUBLIC/ariesrs.html>



ARIES-RS Reactor Concept



Modifications for CLiFF First Wall

Figure 7.6-1: Comparison of ARIES-RS configuration and CLiFF modifications.

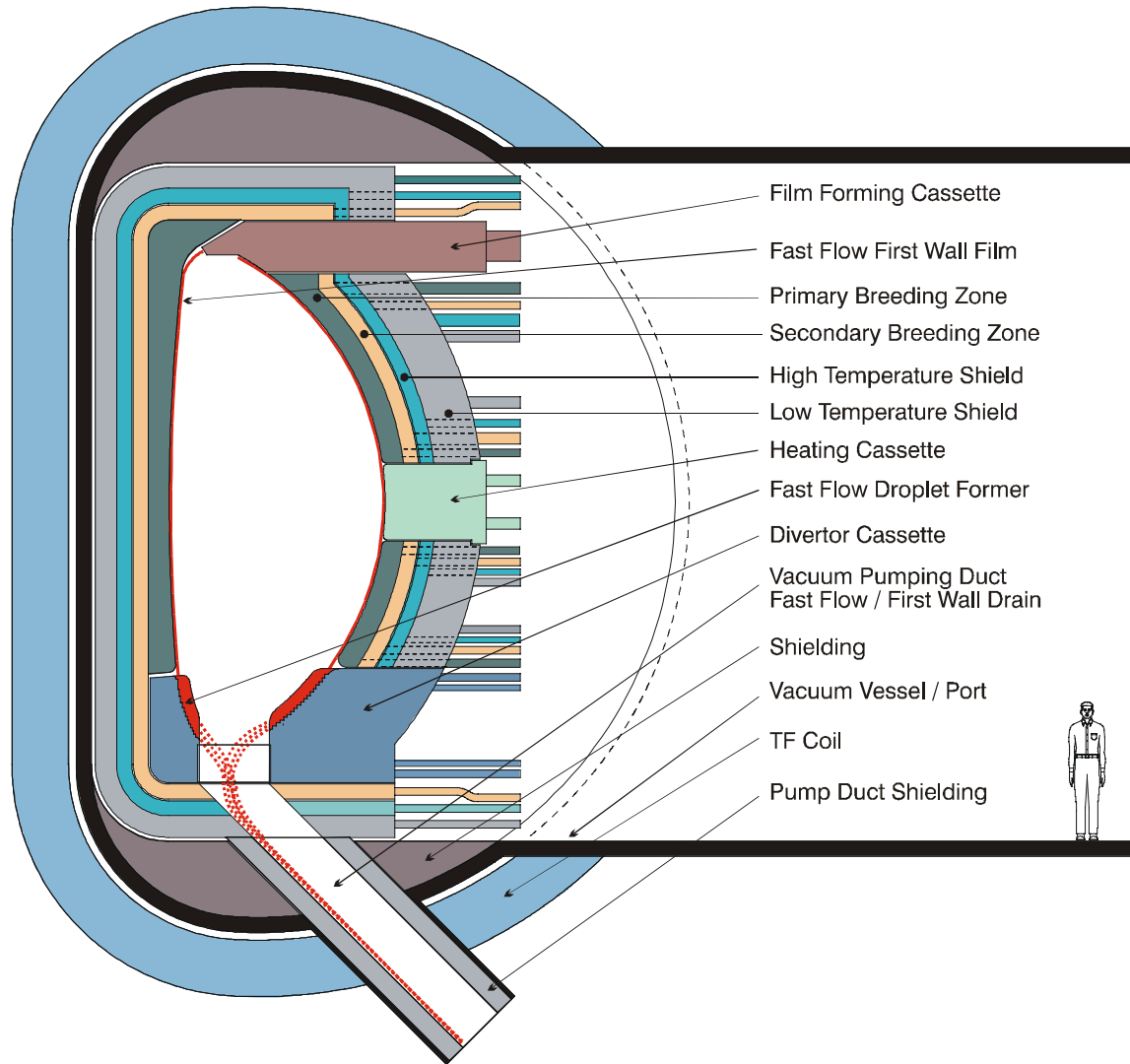
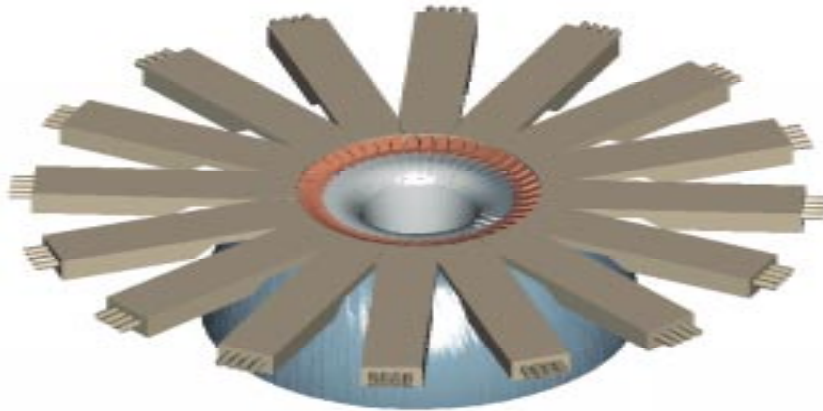
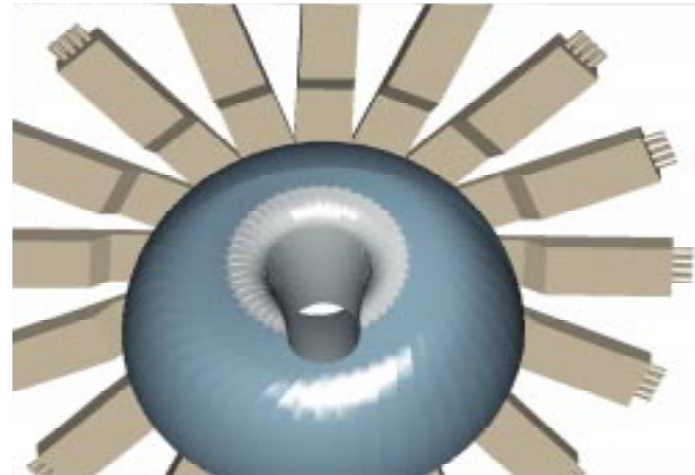


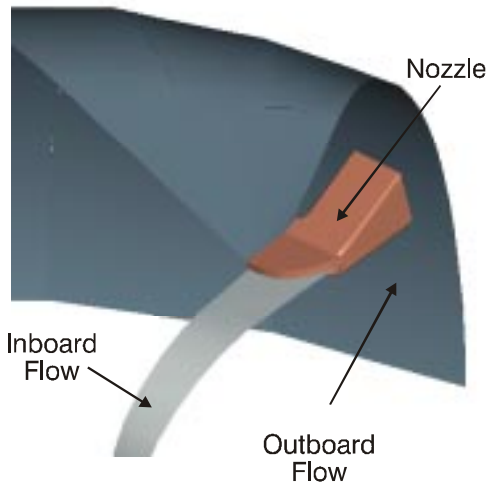
Figure 7.6-2: Elevation view of CLiFF concept.



Top view of convective layer forming device array



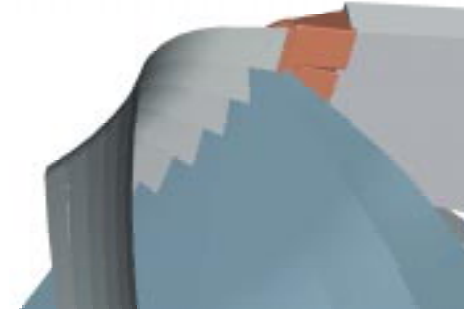
View looking up from inside the machine



View of convective layer forming device - single nozzle



View from centerline of machine showing inclination of nozzles



View from plasma looking up, nozzles are completely shielded

Figure 7.6-3: Convective Layer film forming device.

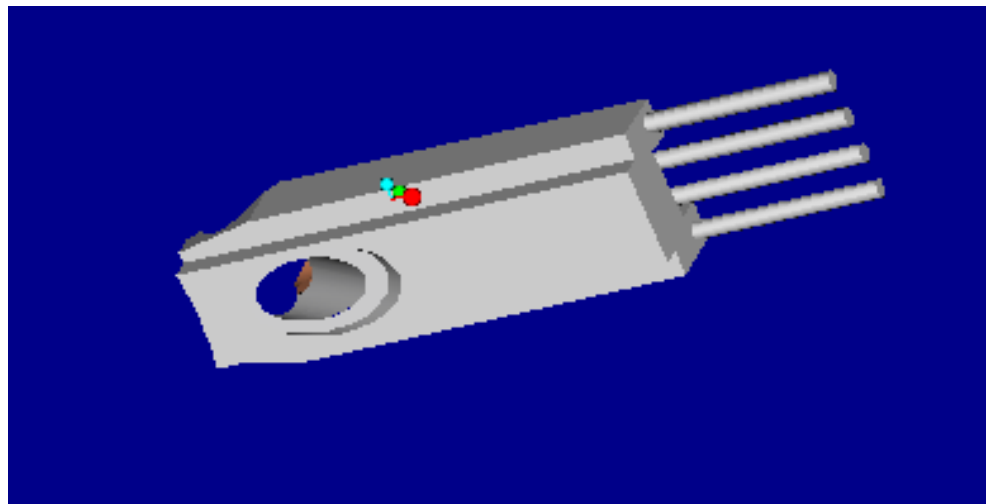
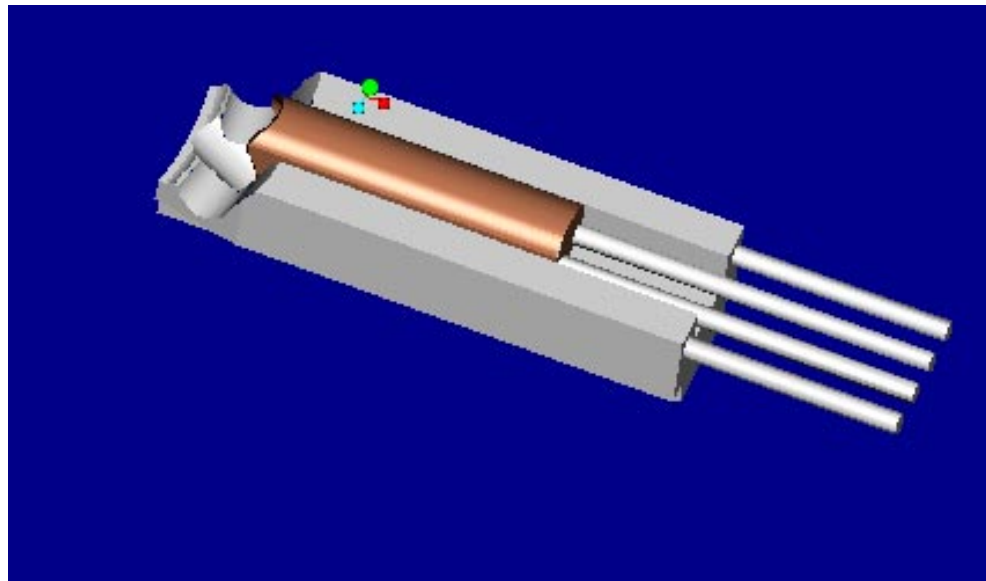


Figure 7.6-4: Film collection trough and divertor cassette showing piping, passage to vacuum pumping duct and divertor comb features.

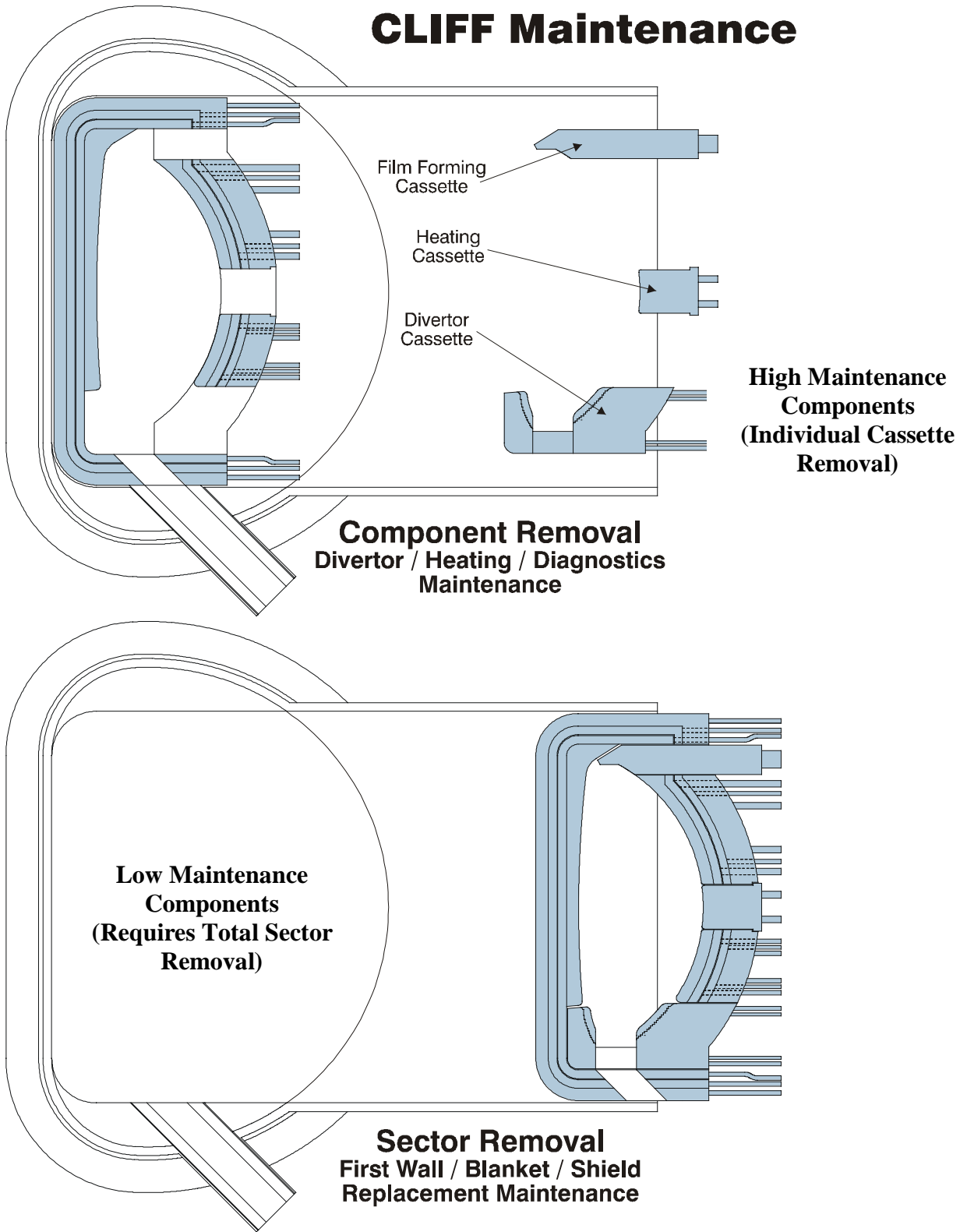


Figure 7.6-5: Maintenance approach for CLiFF concept.

7.7 Safety and Failure Analysis

Because this design is in a preliminary stage, the purpose of this safety evaluation was to look for “show-stoppers,” situations where it is doubtful that safety requirements can be met. Chapter 4 (Evaluation Criteria) gives general safety guidelines, and although these are not hard limits, they provide guidance for designs in early stages.

7.7.1 LOCA Calculations

A series of Loss of Coolant Accident (LOCA) calculations were done for a CLiFF design with lithium / vanadium based on the ARIES-RS radial build and material choice. This calculation was done to estimate long-term temperatures and provide guidance to designers to help them make the design better from a safety point of view (e.g., provide good heat transfer paths that will limit long-term LOCA temperatures). Calculations using the CHEMCON code [1] showed that a LOCA, with no safety-grade cooling systems (therefore no active cooling), resulted in temperatures in excess of 800°C, lasting for almost 10 days (see Figure 7.7-1). As indicated in Chapter 4 (Evaluation Criteria), a general guideline is that long-term temperatures should be below 800°C to minimize the contribution to the activation product source term from oxidation-driven mobilization. While vanadium is significantly less of a radiological hazardous than a material such as tungsten, for example (see Chapter 14), this is probably an unacceptable temperature and time after shutdown. The same figure shows the temperature distribution assuming vacuum vessel cooling during the LOCA. With this active cooling, the peak temperature is lower, however, the temperature is in excess of 800°C for 3.5 days.

Because vanadium is a low decay heat material, it is surprising that temperatures are this high. Further examination of the results indicates that the shield assumed for the activation and decay heat calculations is contributing significantly to the decay heat. The shield is based on the ARIES-RS design, and uses Tenelon, a high-manganese steel, as the major structural material. It is possible that using a lower decay heat material such as a low activation ferritic steel would result in acceptable long-term temperatures, and provide similar shielding. This solution would be better than having to rely on a safety grade cooling system (one that would continue to operate during a LOCA).

After the shield is optimized, and new decay heat calculations are completed, the next step in this type of analysis is to calculate the amount of material mobilized during a postulated accident, and the corresponding off-site dose. This gives an indication of the confinement necessary to ensure doses that meet safety limits. These calculations will be documented in the next report.

7.7.2 Other Safety Issues and Reliability Issues

Because liquid lithium may be used in this design to provide cooling and tritium breeding, the design suggestions outlined in Chapter 14 should be followed. As more design detail becomes available, further safety analyses will be done to ensure that safety requirements are met. Similarly, a reliability assessment cannot be done until more

design detail is available, however general information on reliability issues can be found in Chapter 14.

References 7.7

1. M. J. Gaeta and B. J. Merrill, CHEMCON User's Manual Version 3.1, INEL-95/0147, September 1995.

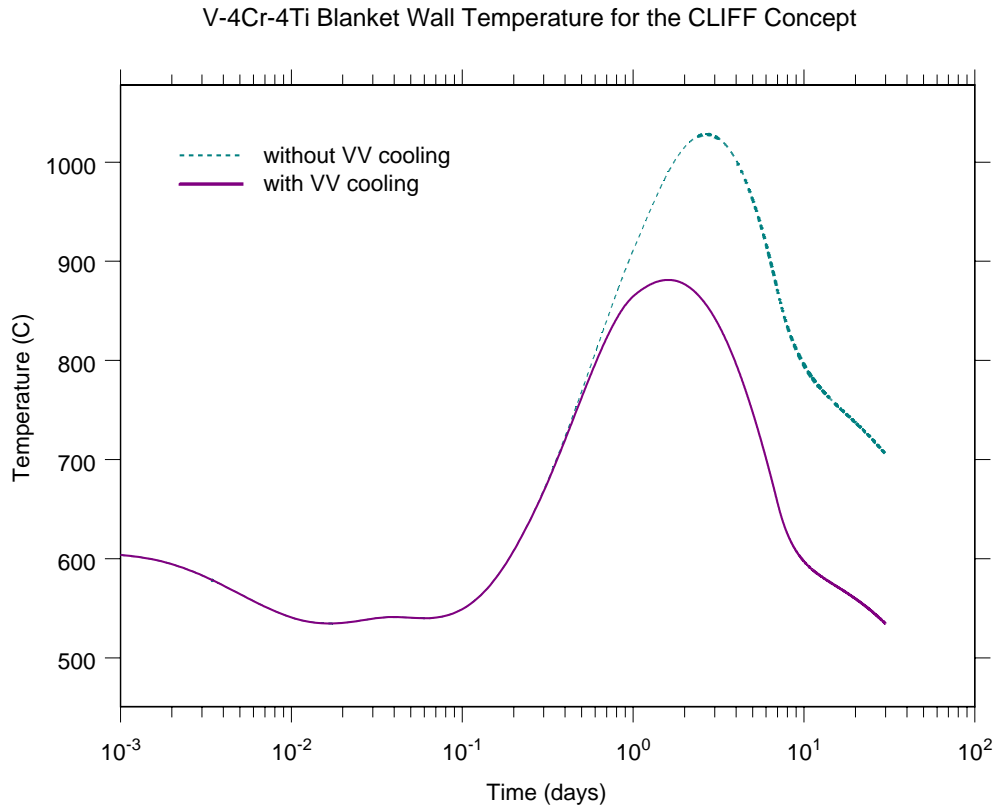


Figure 7.7-1: FW temperature assuming no active cooling during LOCA

7.8 Evaluation of Liquid Options

Similar issues exist for CLiFF as in the thick liquid wall and blanket option. This information is reported in Section 5.8 in Chapter 5 and is not repeated here.

7.9 Performance Summary for Evaluation

The majority of this information is included in the tables and figures of Sections 7.5 and 7.6 of this chapter. The CLiFF design is not yet at a stage where complete (and more importantly accurate) design information of this type has been finalized. We hope to continue work on the design to further flesh out these design parameters. A summary of the information specified in Chapter 4, Evaluation Criteria is given below.

Table 7.9-1: Evaluation Criteria information for CLiFF variants
(* indicates value was not determined)

	Flibe	Lithium	Tin-Lithium
Geometry	ARIES-RS	ARIES-RS	AIRIES-RS
Sketches	7.1-1 7.6-2	7.1-1, 7.6-2	7.1-1, 7.6-2
Radial Build	7.4-1	7.4-1	7.4-1
Nozzles	7.6-3, 7.6-5	7.6-3, 7.6-5	7.6-3, 7.6-5
Divertor Cassettes	7.6-4, 7.6-5	7.6-4, 7.6-5	7.6-4, 7.6-5
Flow Paths/Temps	7.5-8	7.5-6	7.5-7
Piping Location	7.6-1	7.6-1	7.6-1
Loads			
Total Surface Heat, MW	1125	1125	1125
Total Heat Load, MW ^d	5040	5040	5040
Ave. FW SHL, MW/m ²	1.9	1.9	1.9
Ave. Div. SHL, MW/m ²	7.6	7.6	7.6
Ave. NWL, MW/m ²	7.1	7.1	7.1
Peaking Factor	1.4	1.4	1.4
Coolant Parameters			
FW Inlet Temp, C	500	325	400
FW Outlet Temp, C	530	357	472
FW Noz. Pres, MPa ^e	0.1	0.05 + MHD	0.3 + MHD
BZ Inlet Temp, C	530	357	472
BZ Outlet Temp, C	601	600	640
BZ Flow Pres, MPa	*	*	*

^d Assumes a 1.15 multiplication factor for all liquids, true M will vary

^e Assumes velocity head only, MHD contributions were not estimated

Mass Flowrate, Kg/s	21000	8500	79900
FW velocity, m/s	10	14	10
BZ velocity, m/s	0.5	0.3	0.5
FW Piping Size, m ^f	0.4	0.5	0.4
BZ Piping Size, m	*	*	*
FW Pump Power, MW ^g	3.5	650	196
Structural Material	ODS Ferritic	V-4Cr-4Ti	* ^h
Max. Structure Temp, C	*	*	*
Max. Stress, MPa	*	*	*
Nuclear Analysis			
Li Enrichment, *	25	25	90
Local TBR	1.16	1.46	1.26
Max. Nuclear Heat in Structure, W/cc	56	20	49
Max. Nuclear Heat in Breeder, W/cc	71	52	97
Energy Multiplication	1.02	1.14	1.39
Damage, DPA/FPY	110	123	122
He Prod, appm/FPY	1301	454	1150
Activation, Ci/cc	10	*	10
Decay Heat, W/cc	0.1	*	0.1
Radwaste Classification	Class C	Class C	Class C
Power Cycle	Rakine	Rakine	Rakine
Ave. Thermal Efficiency	44.6	42.8	46.9

7.10 Key Issues and R&D

There are several dominant issues that go directly to the feasibility of this concept, and many more issues that weigh heavily on the ultimate attractiveness. The amount of allowable evaporation must be determined for all liquid candidates. This is both a feasibility issue and an attractiveness issue. We recognize that a fully consistent answer to this question will require a considerable amount of research in modeling and analysis of plasmas with liquid wall boundaries, as well as experimental research in various confinement devices. In this section, then, we look to the most serious issues associated

^f Assumes 5 m/s maximum velocity in supply pipes

^g Assumes loss of velocity and hydrostatic head, fully developed MHD forces in electrically-insulated supply pipes and approximate estimation of variable B effect for entrance/exit to magnetic field between TF coils. For LM, the value may be reduced by elongated, multiple supply channel design (to be investigated)

^h Ferritic Steel used in the nuclear analysis, but is probably not suitable for this high temperature operation with Sn-Li

with the hydrodynamic feasibility for implementation in the ARIES-RS type reactor. In addition, we pay some attention to serious system issues associated with tritium retention and permeation and material compatibility. These issues are summarized in Table 7.10-1 along with a rating of their relative critical need.

7.10.1 Hydrodynamic and Heat Transfer Feasibility Issues

The issues in this category differ significantly for molten salts versus liquid metals. For Flibe, the main issue concerns the penetration of heat at the free surface and the availability of a robust operating temperature window. Other issues as to the formation and removal of the liquid flow in the plasma chamber, and the accommodation of penetrations are also serious, but in our opinion solvable via numerical modeling and scaled experiments with Flibe simulants (such as water). These issues are pointed out at the end of Section 7.6. The heat transfer issue is a more serious unknown, as current limits on surface temperature for Flibe are estimated by the plasma interface group at about 560°C. Also a serious issue for Flibe, is the behavior in the divertor region, where direct plasma contact occurs. The amount of material sputtered and redeposited needs to be determined before accurate plasma modeling of the region can take place.

The main issue facing liquid metals is of course that of MHD interaction. The CLiFF flow itself is very sensitive to changes in drag since the only driving force is gravity. Without toroidal axi-symmetry of the flow and field, reliable insulator coatings will be required on all surfaces in contact with the LM layer. The MHD forces from any surface-normal components of magnetic field can upset the force balance, especially when complete axi-symmetry is assumed in the toroidal direction. Additionally, gradients in toroidal or surface normal fields can exert a significant drag on the free surface flow. All these effects need to be analyzed in greater detail, with both modeling and small-scale experimental efforts to see if a suitable flow is indeed possible in the real fields of a tokamak or other plasma confinement device including the accommodation of required penetrations.

LMs however, offer the potential for active control that is not present with the molten salt. By biasing and applying electric currents, the LM can be pumped or pushed against the back-wall *in-situ* – offering the chance to “confine” the liquid wall just as we confine the plasma. Indeed we may find that such measures are required in order to utilize LMs at all.

Apart from the free surface flow itself, MHD issues exist in the supply and drain lines and blanket flows as well. Insulator coatings are needed for these structures. Additionally, due to the large LM flowrates required for CLiFF, large pressure drops are expected in the entrance regions between toroidal field coil legs. These pressure drops can theoretically be overcome by *in-situ* LM pumping, but lead to very large pumping powers for the CLiFF designs with LMs. This issue will require a careful design work and analysis of the supply/exit channel geometry so that the pumping power is reduced to an acceptable level.

7.10.2 Other system attractiveness issues

Impact of liquid wall implementation on other reactor systems is another category of issues for the CLiFF concept. In particular, it will be likely that heating and diagnostic ports must be redesigned to allow flow to pass around the penetration. Pumping systems with a considerable amount of vapor from liquid evaporation will need to be modified. Tritium recovery (especially with hydrogen getters like lithium) will be even more challenging, and material selection and compatibility to help optimize liquid wall performance must be addressed. Flibe chemistry, decomposition and corrosion issues must be addressed for all liquid wall and blanket options.

Ultimately a system study to weigh the relative effect of liquid walls on the entire reactor design and operation will be needed.

Table 7.10-1: Key Issues and R&D for CLiFF Concepts
(x's indicate relative critical need, - indicates this is not an issue for this material)

Issue and/or R&D Area	Flibe	Li	Sn-Li
Plasma Compatibility	xxx	xxx	xxx
MHD Surface Heat Transfer	xxx	x	x
MHD Drag in FW	-	xxx	xxx
MHD Drag in Supply/Exit	-	xxx	xxx
MHD Effects due to Plasma Shifts	-	xxx	xxx
Active MHD Control	-	xxx	xxx
Tritium Recovery	x	xxx	x
Tritium Permeation	xxx	x	xxx
Effect on Plasma Stability	xx	xx	xx
Accommodation of Penetrations	xx	xxx	xxx
Improved Design	xxx	xxx	xxx
Chemistry and Corrosion	xxx	x	xxx
Material Database	xxx	x	xxx